ΕΘΝΙΚΟ ΜΕΤΣΟΒΙΟ ΠΟΛΥΤΕΧΝΕΙΟ

ΣΧΟΛΗ ΠΟΛΙΤΙΚΩΝ ΜΗΧΑΝΙΚΩΝ

ΕΡΓΑΣΤΗΡΙΟ ΜΕΤΑΛΛΙΚΩΝ ΚΑΤΑΣΚΕΥΩΝ

ΜΕΤΑΠΤΥΧΙΑΚΗ ΕΡΓΑΣΙΑ

ΠΕΙΡΑΜΑΤΙΚΗ ΔΙΕΡΕΥΝΗΣΗ ΣΥΜΠΕΡΙΦΟΡΑΣ ΤΟΞΩΝ ΑΠΟ ΧΑΛΥΒΑ

ΦΟΙΤΗΤΗΣ

ΚΩΝΣΤΑΝΤΙΝΟΣ Π. ΑΔΑΜΑΚΟΣ

ΕΠΙΒΛΕΠΟΝΤΕΣ : Δρ. ΧΑΡΗΣ ΓΑΝΤΕΣ, ΑΝΑΠΛΗΡΩΤΗΣ ΚΑΘΗΓΗΤΗΣ ΕΜΠ
Dr. CYRIL DOUTHE, ΜΕΤΑΔΙΔΑΚΤΟΡΙΚΟΣ ΕΡΕΥΝΗΤΗΣ, LCPC

ΟΚΤΩΒΡΙΟΣ 2010

NATIONAL TECHNICAL UNIVERSITY OF ATHENS

SCHOOL OF CIVIL ENGINEERING

LABORATORY OF STEEL STRUCTURES

POST-GRADUATE THESIS

EXPERIMENTAL INVESTIGATION OF STRUCTURAL BEHAVIOR OF STEEL ARCHES

STUDENT

KONSTANTINOS P. ADAMAKOS

SUPERVISORS : Dr. CHARIS GANTES, ASSOCIATE PROFESSOR, NTUA
Dr. CYRIL DOUTHE, POST- DOVTORATE RESEARCHER, LCPC

OCTOBER 2010

NATIONAL TECHNICAL UNIVERSITY ATHENS
SCHOOL OF CIVIL ENGINEERING
LABORATORY OF METAL STRACTURES

POST-GRADUATE DIPLOMA THESIS

Experimental investigation of structural behavior of steel arches

KONSTANTINOS P. ADAMAKOS

SUPERVISORS: Dr. CHARIS GANTES, ASSOCIATE PROFESSOR NTUA

Dr. CYRIL DOUTHE, POST-DOCTORAL RESEARCHER

OCTOBER 2010

ABSTRACT

The present thesis has as main purpose to investigate the existence and significance of two special phenomena which occur in curved beams and especially in arches. These phenomena refer to the residual stresses created by the curving process and the out of plane stresses and strains created by the curvature of the curved beams.

The first chapter introduces the thesis and describes previous research in similar issues. Chapter 2 presents an analytical study, where the static behavior of the arch, the calculation of the out of plane stresses and strains and that of the residual stresses are presented.

Chapter 3 presents the process followed in order to choose what was necessary for the experiment. This includes the geometry of arches, the material, the supports and the general set-up of the experiment. In this section, all selected parameters are shown, followed by documentation.

Chapter 4 presents a first set of numerical analyses. All appropriate analyses take place; including linear, geometrical- nonlinear and completely nonlinear analyses, with and without imperfections. These analyses are used to estimate the behavior of the arches and the loads which will be applied in the experiment.

Results from the previous numerical analyses are taken into account to design each member of the whole experiment. Chapter 5 presents the appropriate checks, according to Eurocode 3, for all members of the experimental set-up. Among others, the arches, the connections (welded and bolted) and the supports are checked.

Chapter 6 is a brief description of the devices used in the laboratory for the experiment. These devices are strain gages, LVDT, measures, computers etc. The general characteristics and properties of each device are referred, including the range, the accuracy and the error of each one.

Chapter 7 is the most important one, presenting all the measured magnitudes; strains, loads, displacements, and deformations are presented, commented and compared to numerical and theoretical results. The numerical analyses refer to the shell element models, taking all results from ADINA software, while the theoretical analyses refer to beam models, the results of which are modified by appropriate relations in order to calculate the estimated magnitudes. The comparison of the equilibrium paths, of the longitudinal and of the transverse strains is presented.

Finally, chapter 8 presents the conclusions that can be drawn from the thesis and describe some helpful suggestions of engineering interest. These suggestions include more complicated checks than those of Eurocode 3 and some ideas for future research.

ΕΘΝΙΚΟ ΜΕΤΣΟΒΙΟ ΠΟΛΥΤΕΧΝΕΙΟ
ΣΧΟΛΗ ΠΟΛΙΤΙΚΩΝ ΜΗΧΑΝΙΚΩΝ
ΕΡΓΑΣΤΗΡΙΟ ΜΕΤΑΛΛΙΚΩΝ ΚΑΤΑΣΚΕΥΩΝ

ΜΕΤΑΠΤΥΧΙΑΚΗ ΕΡΓΑΣΙΑ

ΠΕΙΡΑΜΑΤΙΚΗ ΔΙΕΡΕΥΝΗΣΗ ΣΥΜΠΕΡΙΦΟΡΑΣ ΤΟΞΩΝ ΑΠΟ ΧΑΛΥΒΑ

ΚΩΝΣΤΑΝΤΙΝΟΣ Π. ΑΔΑΜΑΚΟΣ

ΕΠΙΒΛΕΠΟΝΤΕΣ: ΧΑΡΗΣ ΓΑΝΤΕΣ, ΑΝΑΠΛΗΡΩΤΗΣ ΚΑΘΗΓΗΤΗΣ

Dr. CYRIL DOUTHE,ΜΕΤΑΔΙΔΑΚΤΟΡΙΚΟΣ ΕΡΕΥΝΗΤΗΣ

ΟΚΤΩΒΡΗΣ 2010

ΠΕΡΙΛΗΨΗ

Η παρούσα μεταπτυχιακή εργασία έχει ως στόχο να διερευνήσει την ύπαρξη και την επίδραση κάποιων φαινομένων που παρουσιάζονται σε μεταλλικές καμπύλες δοκούς. Τα φαινόμενα αυτά είναι οι παραμένουσες τάσεις που δημιουργούνται από την διαδικασία καμπύλωσης των τόξων, καθώς επίσης και οι εκτός επιπέδου τάσεις και παραμορφώσεις που προκαλούνται από την καμπυλότητα των καμπύλων δοκών.

Στο πρώτο κεφάλαιο πραγματοποιείται μια εισαγωγή στην εργασία, περιγράφοντας τον στόχο της, αλλά και παρουσιάζοντας περιληπτικά τις προσπάθειες άλλων ερευνητών στο αντικείμενο αυτό.

Το δεύτερο κεφάλαιο με τη σειρά του, παρουσιάζει μια αναλυτική εργασία για τον υπολογισμό - εκτίμηση της συμπεριφοράς των τόξων, αλλά και τον υπολογισμό των παραμενουσών και των εκτός επιπέδου τάσεων και παραμορφώσεων.

Το τρίτο κεφάλαιο δίνει μια πλήρη περιγραφή των μεθόδων με τις οποίες επιλέχθηκαν όλες οι απαραίτητες παράμετροι για την πραγματοποίηση του πειράματος. Μεταξύ άλλων, οι παράμετροι αυτές αφορούν στην γεωμετρία των τόξων, το είδος των στηρίξεων κ.α. περιλαμβάνοντας και αιτιολόγηση για κάθε επιλογή.

Το τέταρτο κεφάλαιο παρουσιάζει τις πρώτες αριθμητικές αναλύσεις με τη βοήθεια του λογισμικού ADINA, όπου περιλαμβάνονται γραμμικές και μη γραμμικές αναλύσεις, τόσο γεωμετρίας όσο και υλικού. Επίσης παρουσιάζονται αναλύσεις με και χωρίς την επίδραση ατελειών.

Στο κεφάλαιο 5 χρησιμοποιούνται τα αποτελέσματα από τις προηγούμενες αναλύσεις για τον σχεδιασμό και τον έλεγχο κάθε μέλους που συμμετέχει στα πειράματα. Μεταξύ άλλων, τα τόξα, οι συνδέσεις, κοχλιωτές και συγκολλητές, καθώς επίσης και οι στηρίξεις είναι αυτά τα οποία ελέγχονται για καταστάσεις αστοχίας και λειτουργικότητας.

Το έκτο κεφάλαιο περιλαμβάνει μια σύντομη περιγραφή των μηχανημάτων και των μέσων, τα όποια χρησιμοποιήθηκαν για την πραγματοποίηση των πειραμάτων και τις οποιεσδήποτε μετρήσεις που έγιναν. Περιλαμβάνονται γενικά χαρακτηριστικά και ιδιότητες των μηχανημάτων καθώς και στοιχεία όπως η ακρίβεια, το εύρος και το σφάλμα κάθε συσκευής.

Το έβδομο κεφάλαιο παραθέτει όλα τα αποτελέσματα των πειραμάτων, όπως μετρούμενες τάσεις, μετατοπίσεις, παραμορφώσεις, φορτία κ.α. τόσο για τα τόξα όσο και για το υλικό τους. Τα παραπάνω αποτελέσματα συγκρίνονται με αναλυτικά και αριθμητικά αποτελέσματα από το λογισμικό ADINA και από σχέσεις που παρουσιάζονται στο δεύτερο κεφάλαιο.

Τέλος, το κεφάλαιο 8 κάνει μια γρήγορη αναφορά στα συμπεράσματα που μπορεί να εξάγει κανείς από τα αποτελέσματα και τις συγκρίσεις ολόκληρης της εργασίας, και παραθέτει κάποιες προτάσεις στα ενδιαφέροντα του πολιτικού μηχανικού. Οι προτάσεις αυτές περιέχουν κάποιους περαιτέρω ελέγχους που υποχρεούται να κάνει κανείς για να βρίσκεται υπέρ της ασφαλείας, όσο και προτάσεις για μελλοντική έρευνα.

Dedicated to…..

My parents Panagiotis and Mina

THANKS TO….

I feel the need to thank the persons who were the most important for me during the period of this thesis.

Firstly I would like to appreciate Pr. Charis Gantes, for his professional and scientific guidance and willing, so I could bring into an end an important and interesting issue. Secondly, my special thanks to Dr. Cyril Douthe, for his daily cooperation and his friendly and supporting behavior. Both of them gave me the opportunity to deal with such an important issue, including an interesting experimental work.

As a member of the experimental team, I should thank especially the company of steel members EMEK for its perfect job and its offer to our experiments, with the proper and the in time cooperation with our team.

Finally, my very special thanks to my family, my brother C.Dr. Adamakos Theodoros, my friend Georgia and also to Thomina, Andreas, Dimitris, Nikos, Anastasija etc. for the scientific and psychological support, which they offer to me daily during all the period of the present thesis.

Thanks to all I cannot remember now….

1. Introduction

1.1. Generalities

The present thesis has the purpose to distinguish the behavior of an arch in global and local level. The construction method known as curving process and the creation of radial components of stresses in a curved beam are the main issues of this thesis. The magnitude of residual stresses is comparable to the stresses during the arch loading. Thus, the resistance of the section is possible to be influenced by these stresses, due to a combined interaction of the section in all directions. This combination of stresses can reduce the resistance of the section and as a result the final strength of the arch. The previous notes are referred to the interaction between section and material. However, the fact that the radial component of stress is followed by respective strains creates the thought that the inertial characteristics of the section are continuously changed, which explains why the flange of a section is deformed and the moment of inertia is influenced due to the change of the section- geometry.

1.2. Curving process

Although arches are used many years in several structures and they are considered as the best solutions for particular situations, their construction remain complicated. The most common constructional process includes the connection of many straight beams in a non- linear direction, creating a curved member. Nowadays, small arches are constructed via the curving process. A straight beam passes through rollers, it's being bent creating the desirable radius because of the residual strains. Due to the bending, the section enters the plastic region and remains deformed. These residual strains are of high significance, because their magnitudes are comparable to the yielding strain.

1.3. Radial components of stress

The arches have the advantage to work axially, in most cases, but there is no absence of bending. Both of these two different situations create main stress and strains in the arch. However, the equilibrium indicates a radial component of stress and strain, out of the plane of the arch. This component of stress and strain is not significant enough to have created a special interesting in researchers. The magnitudes

of this strain, however, are really important in some special cases, depending on the geometric and the inertial characteristics of the structure.

1.4. Previous researches

These phenomena are known from the early years with lots of references to describe them. The first trial is presented by Timoshenko (1), at theory of elasticity in the chapter about curved beams. This chapter presents the existence and the significance of the out of plane orthogonal stresses, without giving a particular quantitatively example. Later other projects followed the previous one, Cook and Young (2) and Roark (3), describing more accurately the phenomenon, giving to it a good initial description flanged by relationships, taking into consideration the theory of elasticity assumptions. Today the British guide about curved beams represents these phenomena, but in a very general manner. SCI (4) at the Design of curved beams, refers to the influence of residual stresses and how they can be calculated and as well an approximated expression of the out of plane orthogonal stress for I beams and rectangular boxes is given.

1.5. Current research

The present thesis have the willing and the purpose to present a better approximation about these orthogonal stresses and an arithmetical expression of the residual stresses, while experimental results shows the measurements of the first one compared to the theoretical and investigate the influence of the second one in the whole behavior of the arch.

The continuous approximations by others, lead us to investigate more accurately and experimentally the described phenomena. Totally 12 specimens are tested in the laboratory. The arches are separated to high and shallow arches, having six from each team. During the experiments, two different loads are applied. Two same concentrated loads at the arch crown but in two different directions. In each kind of load three high and three shallow arches are tested. The experiments include the measurement of strains on specific points of each arch, in order to be compared to the theory of the present or of previous theses. The overall behavior of the arch is measured during the test, as well. The deformations of the arch, the displacements on specific points are measured directly, while the load and the stiffness of arches are calculated.

2. Analytic study

2.1. Analytic model of an arch with concentrated load at crown (unpublished report by Cyril Douthe)

2.1.1. The arch and its loading

The structure studied here is a hyperstatic arch with hinges at supports. The geometry of the arch is characterized by the opening angle α and its curving radius R (see figure 2.1). The other geometrical characteristics can be deduced from these two parameters:

- The total length of the arch: $L = 2 R \alpha$
- The span of the arch: $s = 2 R \sin \alpha$
- The high of the arch : $f = R (1 - \cos \alpha)$

An ordinary point on the arch is located through the angle θ which varies from $\theta = -\alpha$ to $\theta = \alpha$. The arch is loaded through a concentrated load P at crown ($\theta = 0$). As a convention P and H are noted positively in the directions shown in figure 2.1.

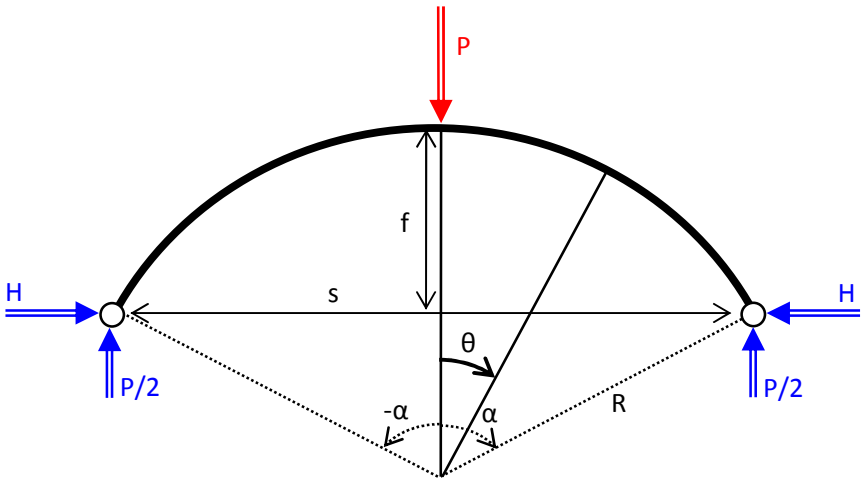

Figure 2.1: Studied arch with load at crown

This load induces compression and bending moment in the arch. It is supposed, however, that the contribution of the compression forces to the axial stress is negligible, so that the behavior of the section can be characterized through its moment-curvature curve. Moreover the loss of stiffness of the arch, once the first yield has happened, is

neglected so that the behavior is supposed to be bilinear or elastic perfectly plastic has shown in figure 2.2. The moment at first yield is evaluated from the elastic limit stress of the material f_y and the elastic section modulus W_{el}. In the same manner, the plastic moment of the section is evaluated from the elastic limit stress of the material f_y and the plastic section modulus W_{pl}. The corresponding curvatures are noted κ_{el} and κ_{pl} and they can be deduced from the young modulus E of the arch and its inertia I by $M_i = EI\ \kappa_i$.

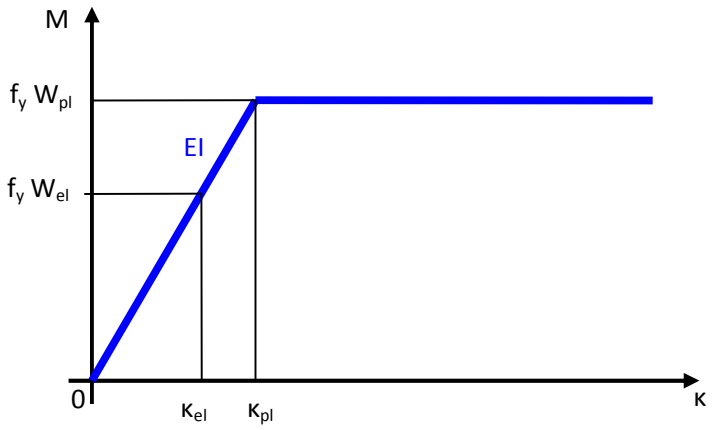

Figure 2.2: Simplified bi-linear moment-curvature

2.1.2. The elastic phase

In a first time, it is supposed that the load remains below a certain value such that the behavior of the arch is linear elastic ($\kappa < \kappa_{pl}$). Then, as the structure and its load are symmetrical, one concentrates on the right side of the arch ($0 < \theta < \alpha$) and the results for the other side will be deduced by symmetry. So, the internal forces in the arch can be found from the equations of equilibrium:

$$N = \frac{P}{2}\sin\theta - H\cos\theta \tag{1}$$

$$M = \frac{PR}{2}(\sin\alpha - \sin\theta) - HR(\cos\theta - \cos\alpha) \tag{2}$$

where H denotes the horizontal reaction at the hinge (which is here taken as hyperstatic unknown), N the normal force and M the bending moment.

To determine the hyperstatic unknown, Castigliano's theorem is used writing that the horizontal displacement at $\theta = \alpha$ is zero:

$$2\int_0^{\alpha} \frac{M}{EI}\frac{\partial M}{\partial H} R d\theta = 0 \tag{3}$$

Developing the integral, one finds:

$$H_\alpha = \frac{P}{2}\left[\frac{2\cos\alpha - 1 - \cos^2\alpha - 2\alpha\cos\alpha\sin\alpha + 2\sin^2\alpha}{\alpha + 2\alpha\cos^2\alpha - 3\cos\alpha\sin\alpha}\right] \quad (4)$$

In the following, the horizontal reaction H_α will be noted in a nondimensional form:

$$H_\alpha = h_\alpha \frac{P}{2} \quad (5)$$

And hence, introducing (5) into (1) and (2), the bending moment and normal forces in the arch are given by:

$$N = \frac{P}{2}\left(\sin\theta - h_\alpha\cos\theta\right) \quad (6)$$

$$M = \frac{PR}{2}\left[(\sin\alpha - \sin\theta) - h_\alpha(\cos\theta - \cos\alpha)\right] \quad (7)$$

Figure 2.3 shows the variation of the bending moments along the arch for different value of the opening angle α. In order to ease comparison, the results have been drawn in a relative manner with x = θ/α. It is remarkable that the proportions of the curve look the same: the bending moments change sign for the same value of relative angle, they are maximum and minimum for the same relative angle and the ratio maximum/minimum is also identical.

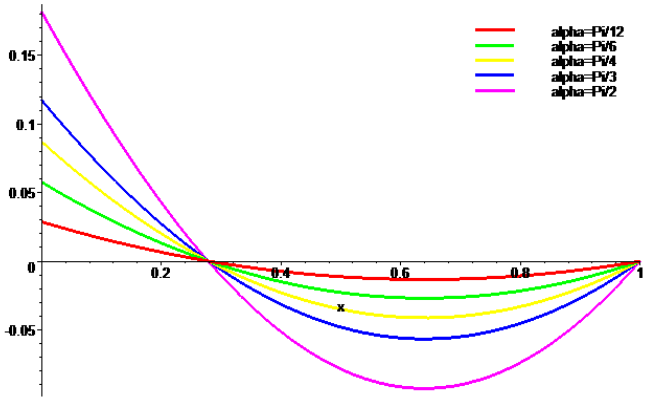

Figure 2.3: Bending moment in the right hand side of the arch

These three values can be deduced analytically from equation (2):

i) The value of the angle, for which the bending moment becomes zero, is a solution of this equation:

$$(\sin\alpha - \sin\theta_1) - h_\alpha(\cos\theta_1 - \cos\alpha) = 0 \quad (8)$$

$\theta_1 = \alpha$ is an obvious solution of (8) which expresses the fact that the bending moment is zero at the hinges. The other solution is found by trigonometric manipulations:

$$\theta_1 = 2\arctan\left(\frac{1}{h_\alpha}\right) - \alpha \tag{9}$$

ii) The maximal bending moment is reached at crown and its value is:

$$M_0 = \frac{PR}{2}\left[\sin\alpha - h_\alpha(1-\cos\alpha)\right] \tag{10}$$

iii) The bending moment passes through a minimum at the angle $\theta = \theta_1$ which is found writing that the derivative of the moment is null in this point:

$$\left(\frac{\partial M}{\partial \theta}\right)_{\theta=\theta_2} = 0 \tag{11}$$

And hence,

$$\theta_2 = \arctan\left(\frac{1}{h_\alpha}\right) \tag{12}$$

The characteristic angle θ_1 and θ_2 are thus linked by the following relation:

$$\theta_1 = 2\theta_2 - \alpha \tag{13}$$

The corresponding bending moment M_1 is obtained by substituting θ_1 in (2).

$$M_2 = \frac{PR}{2}\left[(\sin\alpha - \sin\theta_2) - h_\alpha(\cos\theta_2 - \cos\alpha)\right] \tag{14}$$

The expression of the minimum bending moment M_2 can be modified using (12), some elementary trigonometry and the fact that $h_\alpha > 0$:

$$M_2 = \frac{PR}{2}\left[\sin\alpha + h_\alpha\cos\alpha - \sqrt{1+h_\alpha^2}\right] \tag{15}$$

It is easy to verify that, for the most studied case when $\alpha = \pi/2$, these formulas lead to well known results:

$$h_\alpha = \frac{2}{\pi} \tag{16}$$

$$M_0 = \left(1-\frac{2}{\pi}\right)\frac{PR}{2} \quad \text{and} \quad M_2 = \left(1-\sqrt{1+\frac{4}{\pi^2}}\right)\frac{PR}{2} \tag{17}$$

$$\theta_1 = 2\arctan\left(\frac{\pi}{2}\right) - \frac{\pi}{2} \quad \text{and} \quad \theta_2 = \arctan\left(\frac{\pi}{2}\right) \tag{18}$$

For other values of the opening angle, numerical applications are conducted and gathered in table 2.1. One remarks that the values of the characteristic angles are very similar (less than 1% difference) and confirmed the impression of figure 2.3. In a first approximation one can thus say that the bending moment is zero for θ = 0.28 α and that it reaches a minimum for θ = 0.64 α.

α	π/12	π/6	π/4	π/3	5π/12	π/2
θ_1/α	0.2800	0.2799	0.2797	0.2794	0.2789	0.2782
θ_2/α	0.64	0.6399	0.6398	0.6397	0.6395	0.6390
M_2/M_0	-0.4640	-0.4676	-0.4737	-0.4826	-0.4946	-0.5103

Table 2.1: Characteristic parameters of the bending moments.

One more characteristic of the elastic phase is the vertical displacement at crown v_0 which is found by double integration of the bending moment:

$$\frac{d^2v}{R^2 d\theta^2} = \frac{M}{EI} \tag{19}$$

and taking into account, the boundary conditions and the symmetry of the deformed configuration:

$$v(\alpha) = 0 \quad \text{and} \quad \frac{dv}{d\theta}(0) = 0 \tag{20}$$

So that finally:

$$v_0 = \frac{PR^3}{4EI}\left[2\left(h_\alpha + \alpha\right) - \left(\sin\alpha + h_\alpha \cos\alpha\right)\left(2 + \alpha^2\right)\right] \tag{21}$$

2.1.3. The plastic phase

The plastic phase begins when the bending moment at crown M_0 (10) reaches the limit elastic bending moment, which means, when $M_0 = f_y W_{el}$. The corresponding applied load is then given by:

$$P_{el} = \frac{f_y W_{el}}{R} \frac{2}{\sin\alpha - h_\alpha(1 - \cos\alpha)} \tag{22}$$

For $P < P_{el}$, the results of previous section are valid (as long as the hypothesis of small displacement is verified which will be checked numerically later). For load higher than P_{el}, the section starts to yield partially and looses strength. To simplify the analytical

model, this softening is neglected, so that it is supposed that, until the first plastic hinge appears, all previous expressions (1-21) are still valid. The first plastic hinge appears, when the bending moment at crown (still given by (10)) reaches the plastic moment $M = f_y W_{pl}$. The corresponding applied load is $P=P_{pl}$ which is given by:

$$P_{pl} = \frac{f_y W_{pl}}{R} \frac{2}{\sin\alpha - h_\alpha (1-\cos\alpha)} \tag{23}$$

When the first plastic hinge appears, the arch still stands because it turns from an hyperstatic scheme (see left side of figure 2.4) to the isostatic scheme of a three hinged arch (see right side of figure 2.4). Hence for calculating the bending moments in the arch, one has to separate the applied load P in two parts: P_{pl} the load which causes the first plastic hinge and $\Delta P = P - P_{pl}$ the additional load.

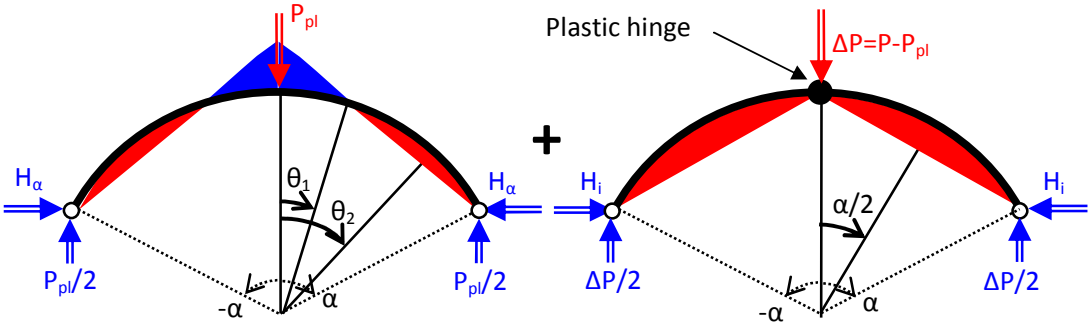

Figure 2.4: Distribution of bending moment after the first plastic hinge has appeared

The first part of the load P_{pl} is constant and induces constant bending moments in the arch which have the distribution shown on the left side of figure 2.4 and can be evaluated from (7) and (23)

$$M_{pl} = \frac{P_{pl} R}{2}\left[(\sin\alpha - \sin\theta) - h_\alpha(\cos\theta - \cos\alpha)\right] \tag{24}$$

The second part of the load ΔP varies with the applied load and induces bending moments which have the distribution shown on the right side of figure 2.4. They can be evaluated by modifying the expression of the bending moment given in (2):

$$M_i = \frac{\Delta P\, R}{2}(\sin\alpha - \sin\theta) - H_i R(\cos\theta - \cos\alpha) \tag{25}$$

H_i is the horizontal reaction due to the additional load ΔP. It is found writing in (25) that the additional bending moment at crown ($\theta = 0$) is zero:

$$H_i = \frac{\Delta P}{2} \frac{\sin\alpha}{1-\cos\alpha} \tag{26}$$

This expression of the horizontal reaction can be rewritten in a non-dimensional manner introducing the parameter h_i:

$$H_i = h_i \frac{\Delta P}{2} \text{ where } h_i = \frac{1}{\tan \alpha/2} \tag{27}$$

It can then be shown easily that the additional bending moment M_i is maximal for $\theta = \alpha/2$ and its value is:

$$M_{\alpha/2} = \frac{R\Delta P}{2} \frac{\cos \alpha/2 - 1}{\sin \alpha/2} = -\frac{R\Delta P}{2} \tan \frac{\alpha}{4} \tag{28}$$

So, finally, the total bending moment in the arch ($M_{tot} = M_{pl} + M_i$) is given by:

$$M_{tot} = \frac{PR}{2}\left[(\sin\alpha - \sin\theta) - \left(h_i\left(1 - \frac{P_{pl}}{P}\right) + h_\alpha \frac{P_{pl}}{P}\right)(\cos\theta - \cos\alpha)\right] \tag{29}$$

From the derivative of expression (29), one finds the angle for which the total bending moment is maximum:

$$\theta_3 = \arctan\left(\frac{P}{h_i(P - P_{pl}) + h_\alpha P_{pl}}\right) \tag{30}$$

Introducing (30) into (29), one finds then the value of the maximum bending moment:

$$M_3 = \frac{PR}{2}\left[(\sin\alpha - \sin\theta_3) - \left(h_i\left(1 - \frac{P_{pl}}{P}\right) + h_\alpha \frac{P_{pl}}{P}\right)(\cos\theta_3 - \cos\alpha)\right] \tag{31}$$

The ultimate load P_{ult} will be reached when the bending moment M_3 will reach the capacity of the section $f_y W_{pl}$. As expression (31) is a non-linear function of the external load, the exact value of the ultimate load can only be determined numerically. However, from the variations of M_i and M_{pl}, one knows that the maximum of the total bending moment M_3 is reached for an angle comprised between the maximum of M_i and the maximum of M_{pl} (which means $\theta_3 \in]\alpha/2, \theta_2[$) and that:

$$M_3 < \min\left(M_{tot}(\alpha/2), M_{tot}(\theta_2)\right) \tag{32}$$

So that one can find an upper bound of the ultimate load P_{ult} from the value of the limit load in $\alpha/2$ and θ_2 :

$$P_{ult} < \min\left(P_{\alpha/2}, P_{\theta_2}\right) \tag{33}$$

where:

$$P_{\alpha/2} = \frac{-2 f_y W_{pl}/R - P_{pl}\left(h_i - h_\alpha\right)\left(\cos\alpha/2 - \cos\alpha\right)}{\left(\sin\alpha - \sin\alpha/2\right) - h_i\left(\cos\alpha/2 - \cos\alpha\right)} \quad (34)$$

$$P_{\theta_2} = \frac{-2 f_y W_{pl}/R - P_{pl}\left(h_i - h_\alpha\right)\left(\cos\theta_2 - \cos\alpha\right)}{\left(\sin\alpha - \sin\theta_2\right) - h_i\left(\cos\theta_2 - \cos\alpha\right)} \quad (35)$$

2.1.4. Synthesis

It is proposed here to summarize the results of the two preceding section and to illustrate them through an application to a specific case which is related to the experimental program DeReStAr. This specific case consists in a rectangular hollow section (RHS100x50x5) bent around the weak axis (I_z = 52.45 cm^4, W_{el} = 20.98 cm^3 and W_{pl} = 24.95 cm^3 according to DIN EN 10219-2). The span of the arch is fixed by the dimensions of the laboratory (s = 4.75 m) and the height is varied from 0.65 m to 0.95 m. The grade of steel is S235, so that the Young modulus E is 210 GPa and the elastic limit stress f_y is 235 MPa.

The results are gathered in three tables. The first one (table 2.2) shows the characteristic parameters of the behavior of the arch. The second one (table 2.3) concerns the characteristic loads of the different arches and the third one (table 2.4) some important characteristic at first yield and ultimate load. In this last table, one remarks that the displacement at crown at first yield, is relative small (1/448th of the span), so that it seems reasonable to consider that the hypothesis of small displacements and linear behavior of the arch will be valid all along the experiment.

f (in m)	0.65	0.75	0.85	0.95
R (in m)	4.664	4.135	3.743	3.444
α (in rad)	0.534	0.612	0.687	0.761
L (in m)	4.984	5.060	5.146	5.241
h_α	2.810	2.423	2.125	1.889
h_i	3.654	3.167	2.794	2.500
θ_1 / α	0.280	0.280	0.280	0.280
θ_2 / α	0.640	0.640	0.640	0.640

Table 2.2: Characteristic parameters of the arches

f (in m)	0.65	0.75	0.85	0.95
P_{el} (in kN)	17.98	17.67	17.34	16.98
P_{pl} (in kN)	21.38	21.01	20.62	20.19

$P_{\alpha/2}$ (in kN)	32.66	32.08	31.45	30.78
P_2 (in kN)	32.19	31.61	30.98	30.31

Table 2.3: External loads characterizing the behavior of the arches

f (in m)	0.65	0.75	0.85	0.95
H_{el} (in kN)	25.25	21.40	18.42	16.04
H_{ult} (in kN)	49.78	42.23	36.36	31.72
M_0 (in kN.m)	4.93	4.93	4.93	4.93
M_2 (in kN.m)	-2.31	-2.31	-2.31	-2.31
v_0 (in cm)	-0.98	-1.00	-1.03	-1.06

Table 2.3: Characteristic values at first yield and ultimate load

2.2. Out- of- plane orthogonal stresses in arches with a rectangular hollow section.

In this paragraph the existence of out- of plane orthogonal stresses is investigated. These stresses are created by the curvature of a curved beam. Although, the curvature is the special characteristic of a curved beam, it creates some special phenomena which are not presented to straight beams.

The flanges of curved members subject to in-plane bending or axial loads must also resist the out-of-plane component of loads resulting from the curvature of the member. This applies to both open and box sections. Figure 2.5a shows a typical box section subjected to bending. Due to the direct stresses σ_1, the forces at the ends of a slice are not in equilibrium because they are inclined. This inclination causes a radial component of load all along the slice, which must be resisted by out-of-plane bending in the flange, as shown in figure 2.5b.

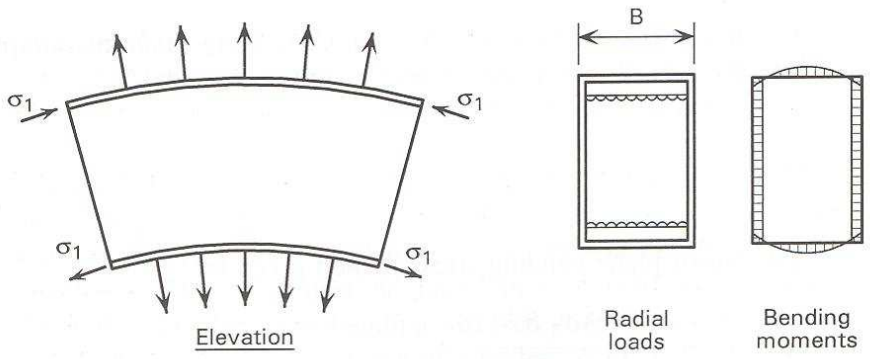

Figure 2.5 Stress diagrams at a curved box section

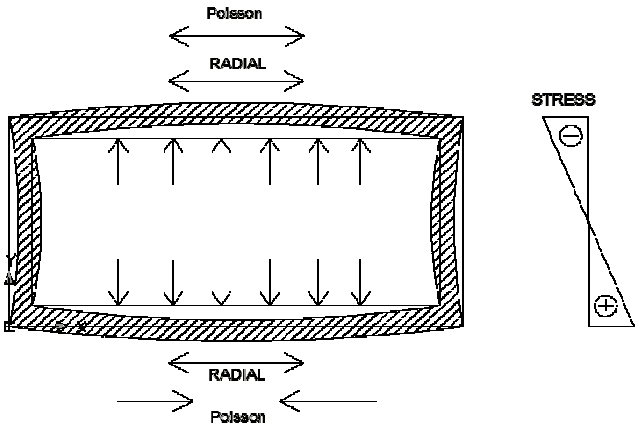

Figure 2.6 Internal strains in the section during the loading

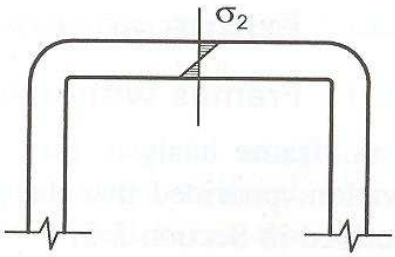

Figure 2.7 Stress diagram of the out of plane stresses, inside the flange of a box section

For the flanges of a box section, conservatively assuming simple supports at the box corners, the maximum moment cannot exceed:

$$M = \left(\frac{T\sigma_1}{R}\right)\left(\frac{B^2}{8}\right) \tag{36}$$

The out of plane bending stress is then given by:

$$\sigma_2 = \frac{M}{W_{fl}} \tag{37}$$

Where

$$W_{fl} = \frac{T^2}{6} \tag{38}$$

Substituting

$$\sigma_2 = \frac{3\sigma_1 B^2}{4RT} \tag{39}$$

Where:

T is the thickness of flanges

B is the width of flanges

R is the curvature of flanges

σ_1 is the longitudinal orthogonal stress

In this part a more accurate calculation of these extra out of plane stresses will be presented. The method for the following calculations is the force method for hyperstatic structures. Before the calculations, some assumptions are taken account.

a) The neutral axis of the section does not move, as the theory indicates and it remains at the section-center.

b) The distribution of the stresses on the wall of the section is linear and symmetric, instead of the real parabolic, according to Timoshenko's theory.

c) The distribution of stresses at the flanges is also linear and constant.

d) The cross section is modeled as a perfect rectangular, whose dimensions are these of the mid-surface of the real section. A more accurate model would be a rectangular section with the corners of the rectangle curved.

e) A linear theory of small displacements, are considered for the section.

The geometrical problem is a hollow rectangle subjected to symmetric uniform distributed load at its flanges, as figures 2.8 shows.

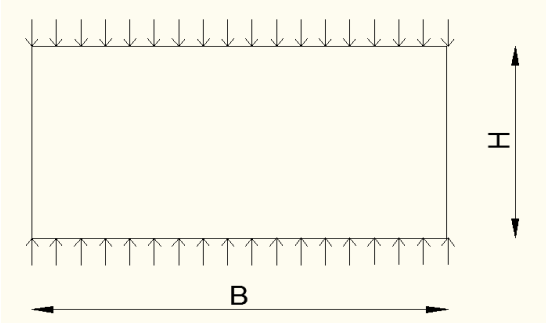

Figure 2.8 Hollow rectangle subjected to radial orthogonal stress.

Due to the symmetry, this symmetrical problem is converted to another simpler problem which is shown at figure 2.9.

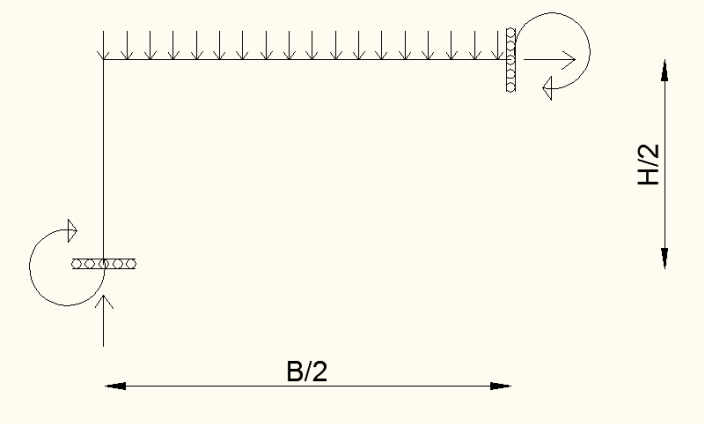

Figure 2.9 Simplified symmetric problem.

In this figure, the unknown reactions are shown. It is one time hyperstatic and it will be solved with the force method.

The problem is again converted to two same isostatic structures. The first one has the real loads and the other one has an artificial unit load similar to the erased hyperstatic magnitude. The equivalent problem is shown below at figure 2.10.

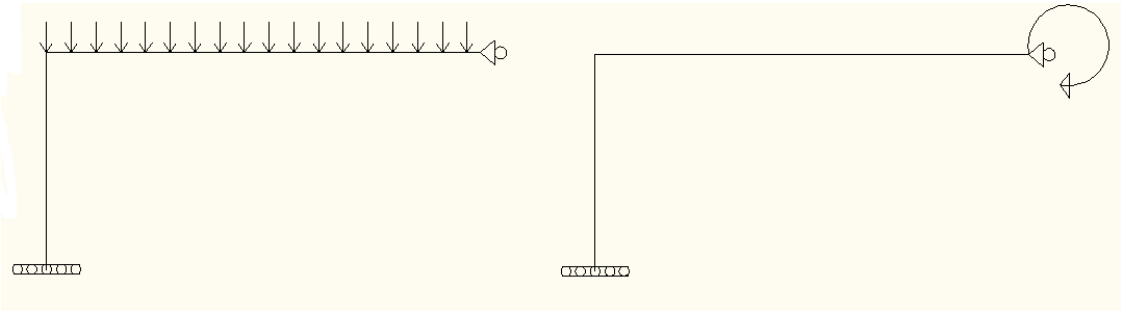

Figure 2.10 Two equivalent isostatic structures.

The unit moment is the hyperstatic magnitude which is presented as X_2. The length and the height of the members are the half of the initial shape, but for an easier process they are referred as B and H. They will be replaced later by the real half values.

Point 1 is the left-down support, whose reactions are referred with index 1 and point 2 is the up and right support whose reactions have the index 2, respectively. Symbols V and H are used for the vertical and horizontal forces respectively, while the symbol M for the moments.

The reactions for each structure are:

$$V_1^L = Pb \qquad V_1 = 0$$

$$M_1^L = Pb^2/2 \qquad M_1 = 1 \qquad (40)$$

$$H_2^L = 0 \qquad H_2 = 0$$

The bending moment diagrams below are constructed from these reactions.

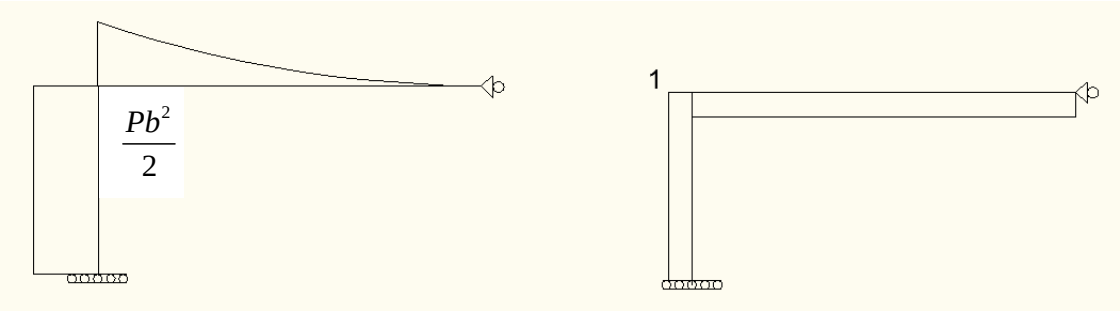

Figure 2.11 Bending moment diagrams.

$$\Delta_2^s = \Delta_2^L + F_{22} X_2 \qquad (41)$$

$$\Delta_2^L = \int M_2 \frac{M_L}{EI} dx = \frac{Pb^3}{6EI} + \frac{3Pb^2 h}{6EI} \qquad (42)$$

$$F_{22} = \int M_2 \frac{M_2}{EI} dx = \frac{6(b+h)}{6EI} \qquad (43)$$

The fact that the hyperstatic magnitude is a bending moment the Δ_2^s is the rotation of the member at point 2. However, the real support is a fixed support, so $\Delta_2^s = 0$.

Substituting the (38-39) to (40),

$$0 = \frac{3Pb^2 h}{6EI} + \frac{Pb^3}{6EI} + \frac{6(b+h)}{6EI} X_2 \qquad (44)$$

Solving in the hyperstatic moment, the result is:

$$X_2 = -\frac{Pb^2(b+3h)}{6(b+h)} \qquad (45)$$

Now the final moment diagram of the initial hyperstatic structure is like in figure 2.11.

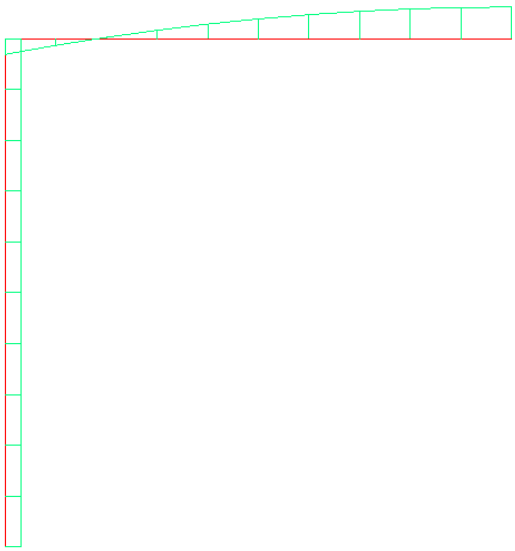

Figure 2.12 Diagram of bending moments

Taking into consideration that $b = b/2$ and $h = h/2$, the maximum moments at the flange and the web are respectively:

$$\max M_f = \frac{Pb^2(b+3h)}{24(b+h)} \tag{46}$$

$$\max M_w = \frac{Pb^3}{12(b+h)} \tag{47}$$

It is considered that load P which is applied in the cross section is given at the Timoshenko's *Theory of elasticity* as:

$$P = \frac{T\sigma_{xx}}{R} \tag{48}$$

The (46) can be modified by substituting with (48):

$$\max M_f = \frac{T\sigma_{xx}b^2(b+3h)}{24R(b+h)} \tag{49}$$

For a simple bending:

$$\sigma_{yy} = \frac{M}{W_{el}} \tag{50}$$

If the elastic modulus of flanges per unit length is given by:

$$W_{el} = \frac{T^2}{6} \tag{51}$$

Substituting the (49) and (51) at (50):

$$\sigma_{yy} = \frac{\sigma_{xx} b^2 (b+3h)}{4Rt(b+h)} \tag{52}$$

All above are referred to stresses. But stresses are not possible to be measured in an experiment. The measured magnitudes are strains. So, the previous expressions will be modified to strain terms.

Taking into consideration that the total strain of out of plane deformation, are resulted from two different components, the expression of this total strain is given for the upper flange (see figure 2.6) by:

$$\varepsilon_{yy} = \varepsilon_{yy}^{ov} + \varepsilon_{yy}^{pois} \tag{53}$$

The first component (ε_{yy}^{ov}) is the strains from the bending of flanges, due to the out of plane load and it is similar to the ovalization strain, which is appeared at a circular section.

The second one (ε_{yy}^{pois}) is the component of Poisson's phenomenon.

Considering the elastic theory with a plane strain assumption, (53) is modified to:

$$\varepsilon_{yy} = \frac{\sigma_{yy}}{E} - \nu\varepsilon_{xx} = \frac{\sigma_{yy}}{E} - \nu\frac{\sigma_{xx}}{E} = \frac{1}{E}(\sigma_{yy} - \nu\sigma_{xx}) \tag{54}$$

Substituting the expression of the σ_{yy} from (52) to (54):

$$\varepsilon_{yy} = \frac{\sigma_{xx}}{E}\left(\frac{b^2(b+3h)}{4Rt(b+h)} - \nu\right) \tag{55}$$

And in terms of strains:

$$\varepsilon_{yy} = \varepsilon_{xx}\left(\frac{b^2(b+3h)}{4Rt(b+h)} - \nu\right) \tag{56}$$

This expression gives the out of plane strain of the section in a function of the in plane strain. The ratio of these strains depends on the geometric characteristics of the arch and the section, and the Poisson ratio. Thus, in the same arch at the same point, two

different flanges seem to have different strain- ratio. The radius of the upper and lower flange is a little different.

Finally, relationship (52) in a common example differs from relationship (39). The first, gives always values smaller than the second one. The main difference is that the (52) includes the height of the section, instead of the (39). Relationship (39) has been produced assuming simple supports at the flanges, that is, simple hinges. Nevertheless, the behavior of web and flange is not independent between them. In a theoretical case, when the height of section approaches infinite, the two relationships extract exactly the same results. So, equation (39) is more conservative than (52).

2.3. Residual stresses.

The present paragraph presents a process to estimate analytically the residual stresses, due to the curving of a straight beam. For this process some assumptions took place.

a) The section remains planar and vertical to the deformed member.

b) Local buckling does not occur at the section.

c) The mechanical properties of the material are constant in the whole member.

d) The Poisson phenomenon is neglected.

e) The deformation of flanges is neglected. In other case the neutral axis of the section would be moved towards the center of curvature.

The beam theory is used to investigate the magnitude of residual stresses. During the curving process the section is bended and it enters very inside the plastic region. While the beam passes out from the rollers, which they curve it, an elastic unloading takes place. This phenomenon is called sprig-back. Summing the stress distributions of the (first) bending process from the (second) unloading process, an approximated expression for the residual stresses is resulted.

More accurately, a radius some smaller than the final-desirable is selected, to bend the initially straight beam, because the spring-back process open the arch, and thus the final radius would be bigger than the estimated. The created strains by this curving process are calculated.

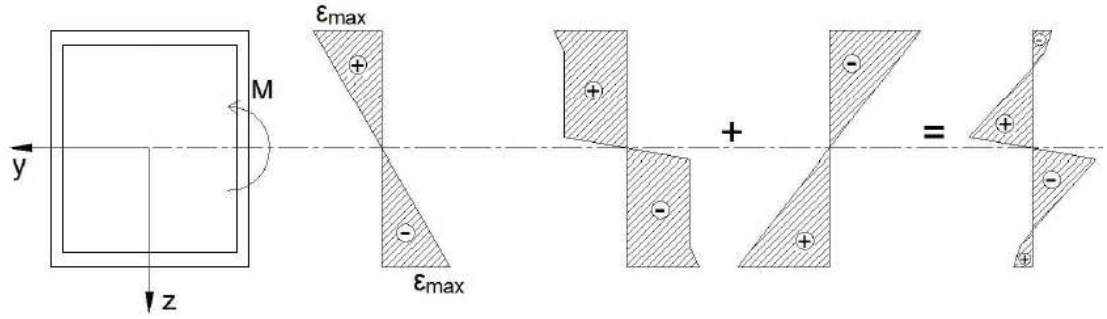

2.13 Stress diagrams during the curving process

$$\varepsilon_{\max} = \frac{h}{2R_c} \tag{57}$$

Where:

h is the height of section

R_c is the initial given radius

With a linear distribution in the height of the section, the matrix of deformations $[\varepsilon_i]$ is resulted.

We can have a multilinear material of j lines-parts. In order to calculate the stress tensor of the section the following expression is useful:

$$[\sigma_{ci}] = \begin{cases} \varepsilon_i E, & \varepsilon_i \le \varepsilon_y \\ f_{y(j-1)} + E_{sj}(\varepsilon_i - \varepsilon_{sj}), & \varepsilon_i > \varepsilon_y \end{cases} \tag{58}$$

Where:

E the Young modulus

E_{sj} the Young modulus of j part of the material

ε_i the strain of the layer

ε_{sj} the end-strain of j part of the material

$f_{y(j-1)}$ the maximum stress of the *j-1* part of material

Knowing the stress tensor we can calculate the force of each layer by the following relationship:

$$[P_i]=[\sigma_{ci}]\begin{bmatrix} t_i b, & z > h/2 - t_w \\ 2t_i t_w, & z < h/2 - t_w \end{bmatrix} \quad (59)$$

Where:

t_i the thickness of the layer

t_w the thickness of the web

b the width of the flange

z the height of the layer

Multiplying these forces with the respect distances of each layer until the neutral axis, the moment which appeared in each layer can be calculated. Summing the moments of all layers, we calculate the bending moment in which the beam has been subjected in order to take the given curvature.

$$M_c = \sum_1^n [P_i]\{Z_i\} \quad (60)$$

After the curving process, the spring-back takes place. Due to the equilibrium

$$M_c + M_{sb} = 0 \quad (61)$$

Thus, the member is unloaded elastically with a moment equal to the previous curving moment.

The spring-back process creates elastic stresses, which are expressed by

$$[\sigma_{sb}] = \frac{M_{sb}}{I}\{z_i\}. \quad (62)$$

Where:

I the moment of Inertia of the section

Finally, the expression for residual stresses is given by:

$$[\sigma_r] = [\sigma_c] + [\sigma_{sb}]. \quad (63)$$

It is useful to note that the spring-back opens the arch with an opposite curvature, which is given by:

$$R_{sb} = -\frac{EI}{M_c} \tag{64}$$

Hence, assuming that

$$\frac{z}{R_f} = \frac{z}{R_c} + \frac{z}{R_{sb}} \tag{65}$$

The final curvature of the beam is given by:

$$R_f = \left(\frac{1}{R_c} + \frac{1}{R_{sb}} \right)^{-1} \tag{66}$$

3. Design of the experiment

3.1. Introduction

This chapter presents the process which was followed to select the experimental set-up and the specimens which have been used for the experiment. Basically the planned set-up is an in- plane bending test of two hinged arches through the application of concentrated load at crown (see figure 3.1). The two phenomena which will be investigated experimentally are the influence of residual stresses due to the curving process and the influence of out- of0 plane bending stress on the behavior of arches. The different parameters, namely the geometry of the arches, their supports, the applied loads and the quality of the material, have to be chosen- so that these phenomena appear clearly and lead to values with large measurable magnitudes with a load as low as possible. The analytical models developed in previous chapter will be used to quantify the different parameters and to guide the final choices.

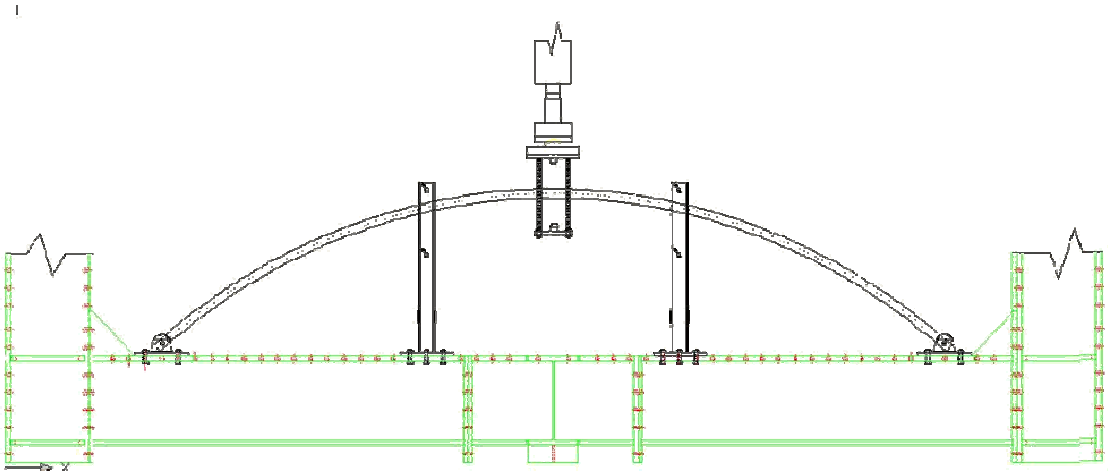

Figure 3.1 Drawing of the laboratory-frame

3.2. Geometry of arches

The first thing which needs to be chosen is the geometry of the arches. The main constrain for this choice is the dimensions of the experimental frame which already exists in the laboratory. The arch must be placed into this frame, in order to be supported and loaded. The maximum span of the arch which matches the frame is 4725 mm and it was chosen because the larger the span the larger the bending stresses at arch crown. In the same way, taking into consideration equation (2.10) of the

analytical part, it is noticed that the higher the arch, the higher the bending moments at crown. For an equivalent stress level, increasing the height of the arch allows thus to reduce the magnitude of the load. Another reason for preferring high arches is that the out-of-plane stresses increase with the curvature (and thus with the height) as shown in (2.56). Indeed the out-of-plane stresses are proportional to the longitudinal stresses and to the curvature which both increase with the height. The higher the bending moments are, the higher the magnitude of orthogonal stresses. And thus, to study the influence of out-of-plane stresses, the higher the arch, the better.

Nevertheless, the other purpose of this experiment is the study of the influence of residual stresses on the arch behavior. Concerning this phenomenon, the reference equation is (2.57) and it shows that the lower the arches radius (thus, the higher the height), the higher the residual stresses. All this leads to choosing the largest possible height. When the hydraulic jack is at its highest position, the available height bellow the load cell is 110 cm. A plate shall be introduced between the load cell and the arch so that the load is applied in a proper way (see section 3.4). A couple of centimers shall be foreseen for this purpose. Moreover, we intend to do tension and compression tests to investigate the influence of residual stresses because these stresses are not symmetrical throughout the section height and shall therefore lead to different behavior in tension and in compression. So, for the tension tests, it is necessary to lower the jack about 10 cm so that it can then go up to apply the upward load. Moreover, taking into consideration that the arch will be supported by hinges and that these hinges have the center of their pin-holes at 7 cm, the maximum possible height is 93 cm, from the center of the pin- hole to the upper flange. So finally, two different heights of arches were selected to have two different values of curving radius: the first one is 85 cm (some space was arranged between the different pieces for practical reasons) and the second one 75 cm. In the following the first ones will be described as high arches and the second as low arches.

3.3. Cross section

The next choice concerns the cross section of the arch. The criterion for choosing the cross section is that it must show high magnitude of out-of-plane stresses when compared to axial stresses. As equation (2.56) shows, a big flange width of the section gives a high out-of- plane orthogonal stress. It is also better to have low loads to have an easier and safer experiment. So, a small cross section should be preferred, in order to have a small resistance. The smallest I-beams are HEA100 or IPE80. However, if the I-beams are loaded until their ultimate resistance, they are extremely vulnerable to lateral-buckling. For sure, curving them along the weak axis will reduce the risk of lateral buckling and, in the same way, reduce the load required for yielding of the section, but this will also nullify the out-of-plane bending stresses which appear only on bent flanges. So, the better compromise seems to use a rectangular hollow section (RHS) instead of I-beams. These closed sections have high resistance to

lateral buckling and also allow out-of-plane bending stresses to develop. An RHS 100x50x5mm is thus chosen, bent the weak way.

Firstly, the major axis is activated against a lateral movement consequently the out of plane critical load is increased, avoiding lateral buckling. Secondly, a big flange width is achieved, in which high values of out of plane orthogonal stresses could be measured. Especially, the theoretical model indicates that in this case, the orthogonal stresses reach the 40% of the main longitudinal stresses, considering the given geometry of the arches known. Finally, this solution gives enough area to place easier the strain gauges so that the measurements of the experiment will be successfully completed. The thickness of the sections was the only parameter which does not optimize our measurements. Equation (2.56) shows that a small thickness would give higher magnitudes. However, the manufacturer of the arches suggested a minimum thickness of 5 mm, in order to complete safely the curving process, without local buckling of the section. Figure 3.2 shows the cross section and how it was placed.

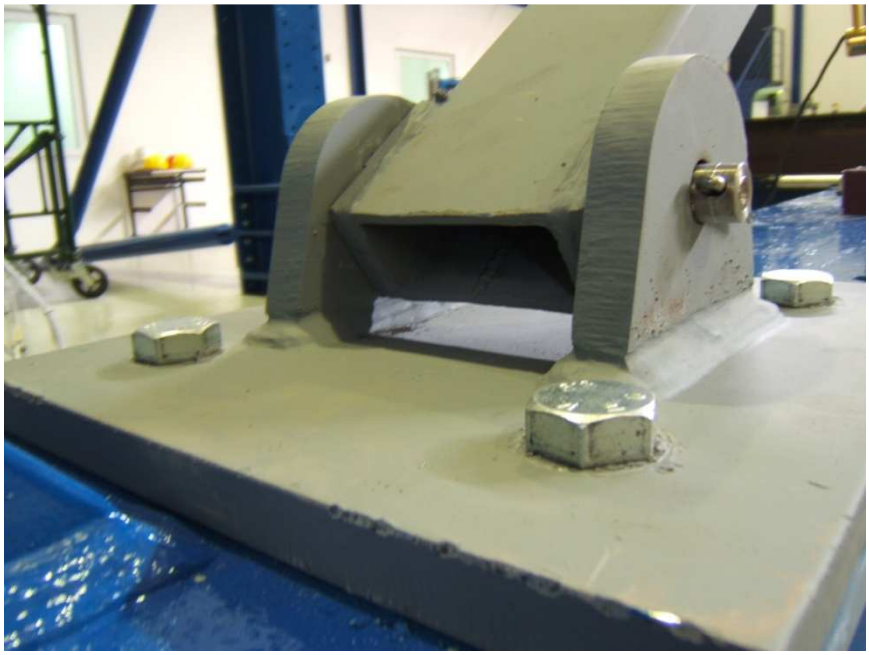

Figure 3.2 The section of the arch at the support

3.4. Lateral supports

In spite of the previous disposition of the cross section, there still might be a risk of lateral buckling of the section due to geometrical imperfections of the arches. Some lateral support might thus be necessary. Numerical simulations are thus conducted in section 4.2 taking into account the conservative assumption that the

hinged supports described in section 3.3 have no out-of-plane stiffness so that the arches are considered as hinged out-of-plane. It appears that it is necessary to support laterally the arch. Members for that purpose are thus installed at 1/3 and 2/3 of the span so that the first possible out-of-plane buckling mode is the third one which occurs much later than the full yielding of the section. Moreover, these positions are away from the measuring devices so that there will not be any problems with the management of the devices and their cables. Figure 3 shows the location of lateral supports at the experiment and figure 4 shows a detail of these.

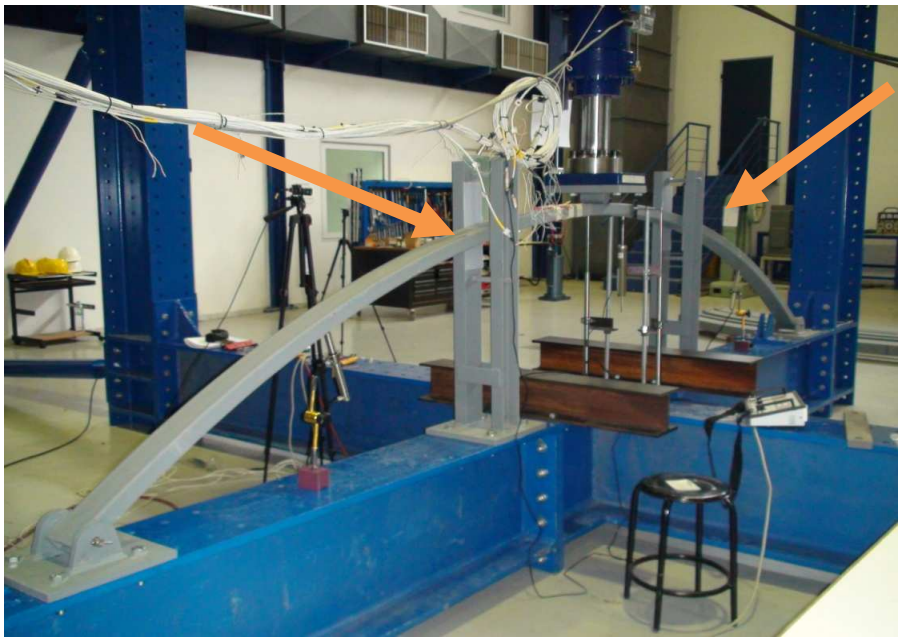

Figure 3.3 The overall setting of the experiment

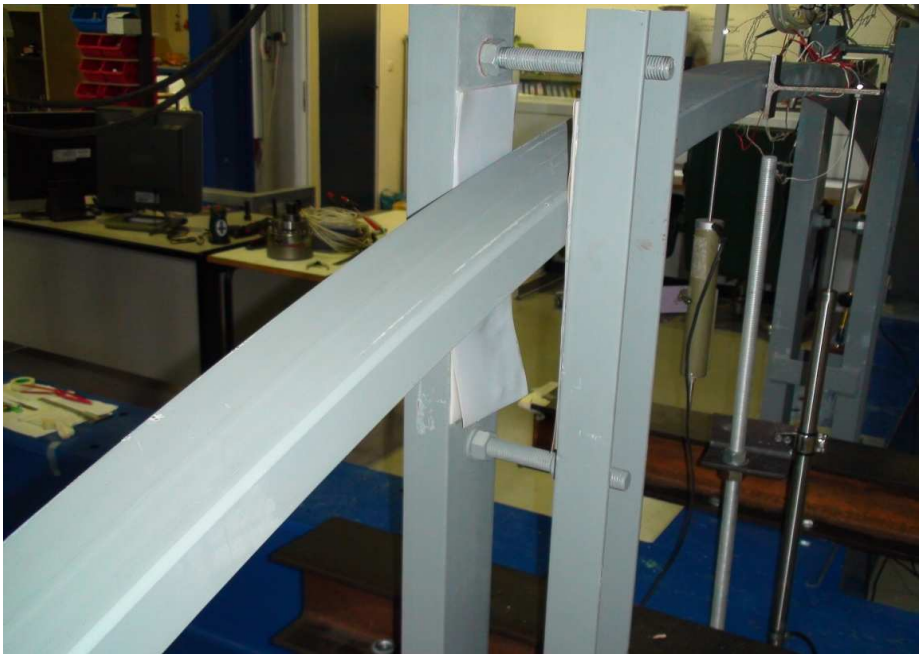

Figure 3.4 Detail of a lateral support

The detail of the lateral support indicates the way it embraces and supports the arch. Two UPN100 are welded on a plate, which are connected to the frame of the laboratory by bolts. The arch passes through the UPN and the two bolts which are shown in the figure are screwed until the UPNs almost touch the arch. These bolts also offer an extra stiffness at an out of plane movement. Otherwise, the two UPN would be independent, and they would behave as flexible cantilevers, due to their big length (960 mm) and their low moment of inertia. Moreover, the white tape in the detail of supports is a Teflon tape, which was placed to each internal side of the support in order to decrease the friction coefficient in case of contact between support and arch.

3.5. Loads

A concentrated load at the crown of the arch is the easiest load to apply. This load is not usual for arches since it does not use the advantages of arch behavior (Arches work well under distributed loads and not well under concentrated loads). A concentrated load creates large moments in the arch and thereby accelerates its collapse.

Two different settings were created to apply these loads. A removable plate connected by bolts to the load cell was used to this end. The concentrated load is managed thorough a semi-cylinder which is welded to the plate. The same method was used for the tension test, reversing the plate and the semi-cylinder and as a result the plate touches the arch on the lower flange. Figures 3.5 and 3.6, show the compression and tension experimental set-up, respectively.

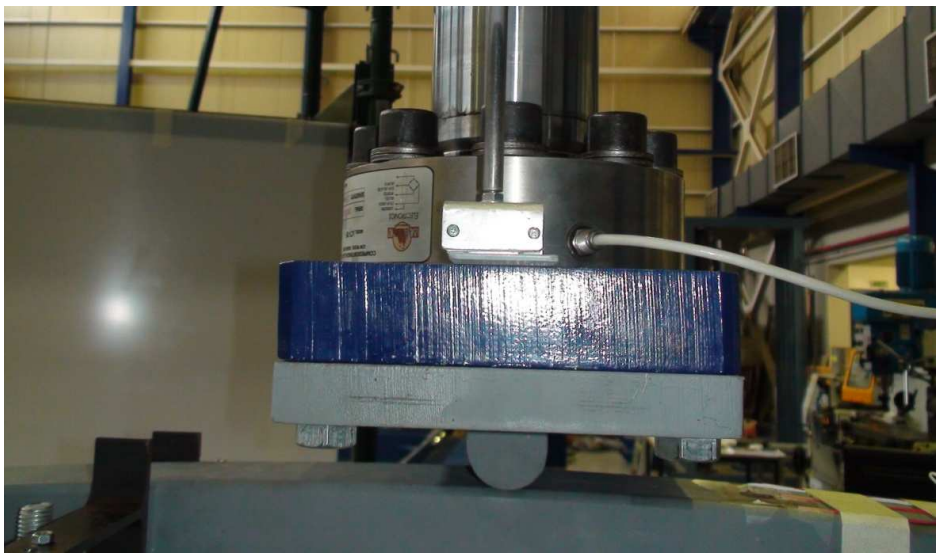

Figure 3.5 Load cell and load plate in the compression test arrangement

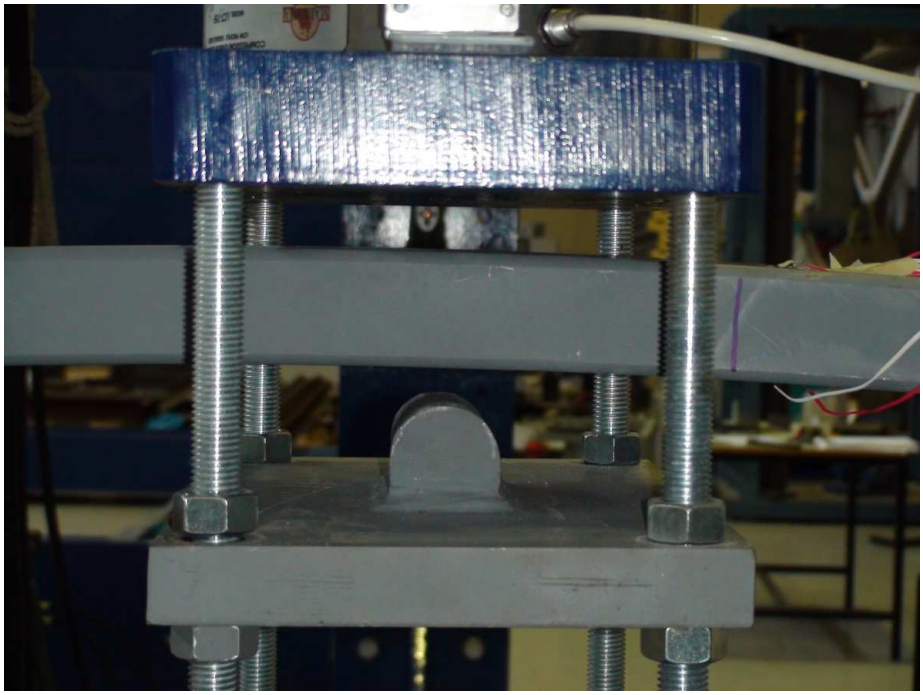

Figure 3.6 Loading plate in the tension test arrangement

The plate shown above has a thickness of 30 mm and the semi- cylinder a height of 48 mm. The thickness of the plate was chosen not only to have enough bending resistance, but also to minimize the displacements from its bending deformations during the tension tests. In other case the measurements would have been affected by these deformations. With this specific thickness the deformation of the plate presents values which did not exceed the noise of the load cell.

3.6. Material

The desire for this experiment is low loads, for safety reasons and for better handling of the members after the end of the loading. Following this, steel S235 is the appropriate material, because it is the lowest-quality standardized constructional steel. Analytical and numerical model will thus be based on this assumption. Experimental tests will show latter that the quality of steel used by the manufacturer was different and also that its characteristic behavior after curving will be very different from that suggested by EC3 (see section 7.1)

4. Numerical models

4.1. Linear analyses

In this section, a number of linear analyses will be presented. Firstly, it is supposed that the material is elastic with properties similar to steel S235, and that small displacements theory is used. The results from these models are useful to estimate the behavior of the arch. ADINA software is used to run the numerical analyses.

The first analysis includes the loading of the two chosen arches. As it is referred in chapter 3, the arches are loaded at their crown by a concentrated load. The load is vertical; at one time it is applied upwards, while at the other one, downwards. The magnitude of the load is typically equal to 10 kN. The structure is completely linear and as a consequence the magnitudes of every load- value are proportional to the initial value.

Beam elements are allowed in the models, according to the ratio of *radii/section-height*. The supports are simple hinges, and the problem is solved as a 2-dimensional problem, as the arch is unbalanced out of its plane, due to the simple in-plane supports. The useful results from this analysis are the diagrams of the bending moment, the axial force and the shear force. However the results that come up for either the tension or the compression load are the same, since the arch is symmetric and the load just changes direction. Table 4.1 shows the results from the analyses described above.

Load P=10 kN	4.725-0.85(1st arch)	4.725-0.75(2nd arch)
Maximum moment (kNm)	2.76	2.81
Maximum axial force (kN)	11.66	13.00
Maximum shear force (kN)	4.92	4.92

Table 4.1 Typical magnitudes from linear analysis

Although the previous results are far from the real values, the deformed shape of the arches does not change. The deformations of the shallow and the higher arch are similar to each other. Figure 4.1 and 4.2 shows the deformation for the tension load and the compression load, respectively. The displacements are surely magnified for a better visualization of the results.

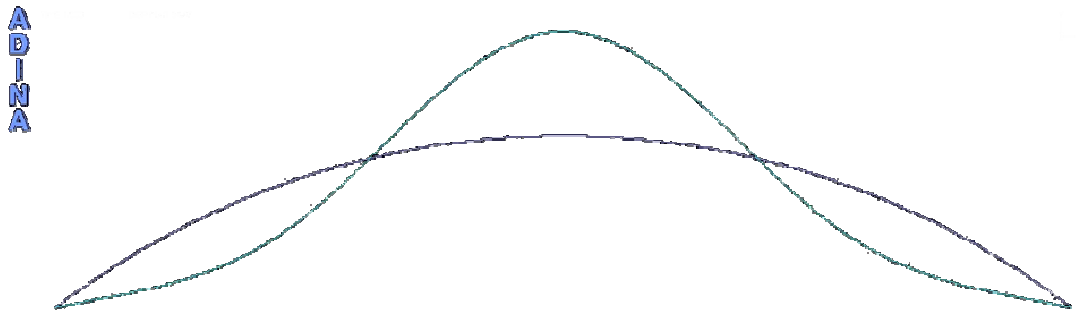

Figure 4.1 Typical arch deformation under a tension concentrated load at the middle

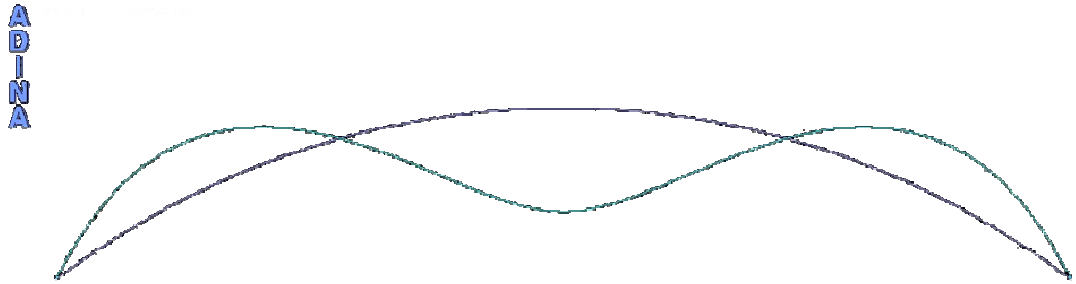

Figure 4.2 Typical arch deformation under a compression concentrated load at the middle

4.2. Buckling analysis.

A buckling analysis of the arches is presented in this paragraph. Shell elements are used for the simulation of the cross section, while the material remains elastic. The critical load for an out of plane buckling is calculated through this analysis.

The simple hinges at the ends of the arch make it extremely sensitive to out-of-plane buckling. In fact, as it is shown in figure 3.2, the pin and the specific setting of support offer a significant out-of-plane stiffness to the arch. However, it is extremely difficult to calculate this stiffness accurately and it is not enough to ensure that such buckling does not occur. The shape of this out-of-plane buckling is shown in figure 4.3.

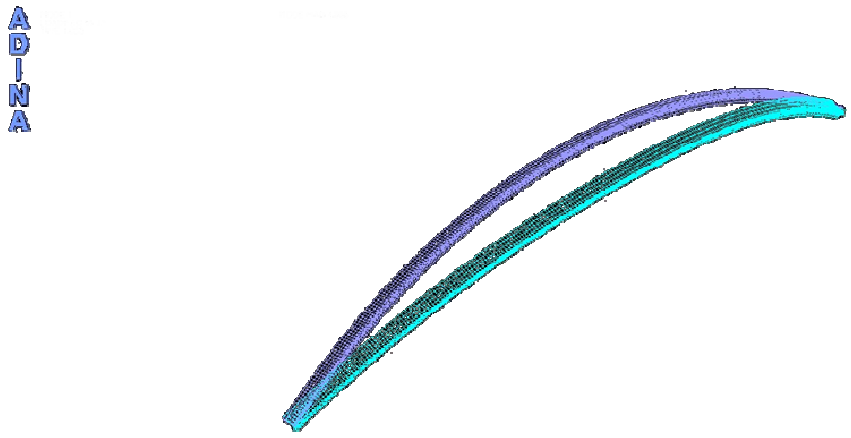

Figure 4.3 Out of plane buckling mode

For safety reasons, as described in paragraph 3.4, two lateral restrains are added in order to prevent such a lateral movement. However, the model changes and a buckling analysis re- run. Now, the first buckling mode is an in plane anti-symmetric one. Figure 4.4 shows this 1st buckling mode. The buckling shape is the same for the two different arches. In the following figure the shape of the shallow arch is presented.

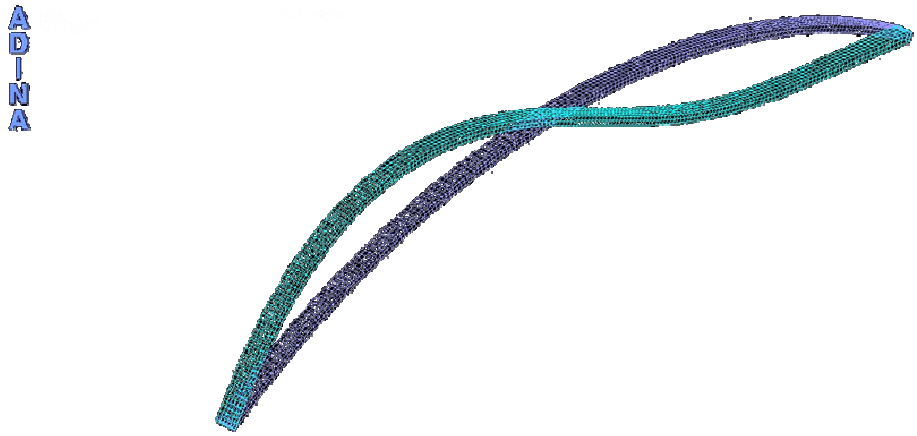

Figure 4.4 1st mode for the shallow arch.

The critical load for this buckling mode is 138 kN for the shallow arch and 150 kN for the high arch; loads under which the arches would have already collapsed from other more complicated reasons.

4.3. Nonlinear analyses

4.3.1. Geometrical nonlinearities

In this part the geometrical nonlinearities of the arches are taken into account. Arches, in general are nonlinear structures. Specifically, this depends on the geometry of the structure and on the kind of load. The current load of the experiment creates high values of bending moments and leads to large deformations. These deformations make the arch change continuously its shape and its stiffness.

The existence of initial imperfections increases more the nonlinearity of the arch. Initial imperfections change the geometry of the arch and make it more sensitive to buckling. The construction process for arches is a difficult and non-perfect process, so the imperfections are significant. Eurocode 3, part 2, gives the appropriate initial imperfections for more accurate analyses.

Two different analyses are presented in this section. Both of them are nonlinear, but the first one refers to a perfect arch, while the second to an imperfect member, according to the imperfections of Eurocode 3. Although, it is described analytically in chapter 5, the imperfections are similar to the anti-symmetric shape, as figure 4.4 shows, and their magnitude is 11 mm at the extreme point of this mode. Diagram 4.1 shows the equilibrium path of the high arch of a nonlinear analysis (NG), a nonlinear analysis of an imperfect member (NG-IMP) and a linear analysis (LINEAR).

Initially, the behavior of the arch is almost the same for the 3 different analyses. However, for higher values of loads the influence of the imperfections is more significant. This influence is only shown in the last part of diagram 4.1. In this case, the critical load is reduced, but this reduction does not exceed the 15%.

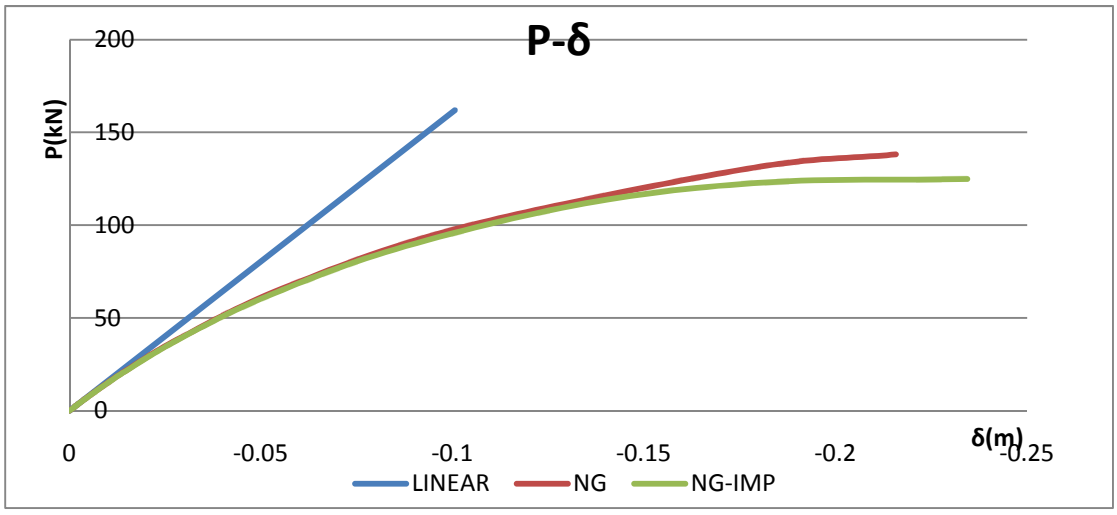

Diagram 4.1 Equilibrium path of high arch

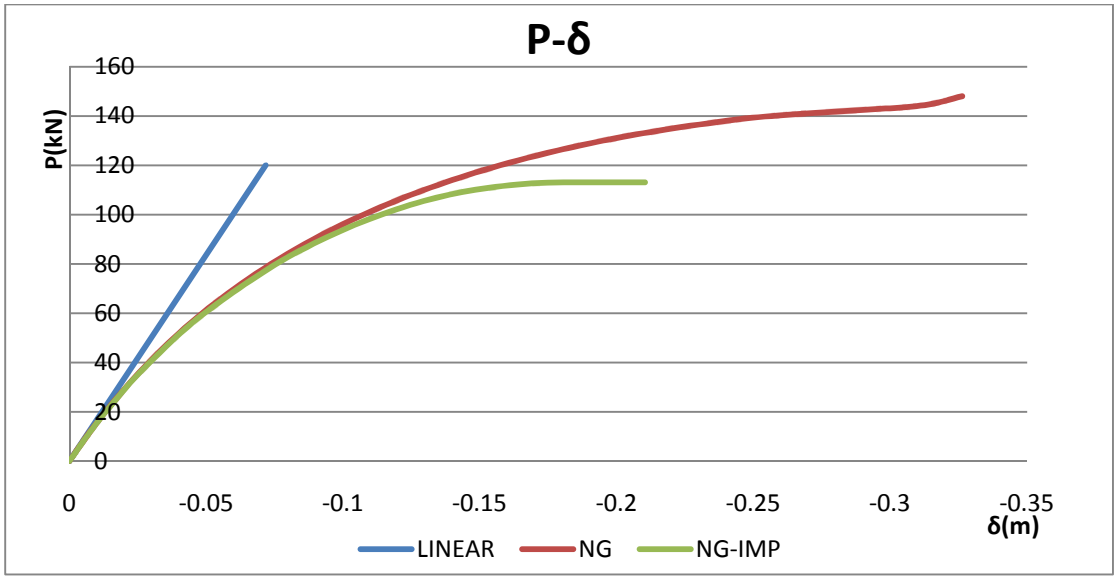

Diagram 4.2 Equilibrium path of shallow arch

The same analyses take place for the shallow arch. Diagram 4.2 shows the same conclusions with diagram 4.1. In the case of the shallow arch the imperfections are more significant. The reduction of the critical load exceeds the 25%.

4.3.2. Material nonlinearities.

In this part the nonlinear behavior of the material is taken into consideration. These analyses are unavoidable, because the real behavior of the arch is nonlinear, due to the yield of the material. The arch enters quickly into the plastic region due to the high magnitude of the stress. The material used for the analyses is a steel S235 and especially the Gioncu and Mazzolani (2002) model. It is a little more accurate than this of Eurocode elasto-plastic material because it takes accounts the steel hardening. The properties of the material are presented below.

$$f_y = 235000kPa$$
$$f_u = 360000kPa$$
$$\varepsilon_y = 0.12\%$$
$$\varepsilon_{sh} = 1.41\%$$
$$\varepsilon_u = 14\%$$

The analyses which take place are completely nonlinear (geometrical and material nonlinearities). Each diagram presents the curves from two different analyses; the one of a perfect member (NGM) and the other from an imperfect member (NGM-IMP), as described above in 4.3.1.

The results for nonlinear analyses are only presented, which are the most accurate for this experiment. The material is a multilinear steel according to Gioncu and Mazzolani material model (2002).

Diagram 4.3 presents a nonlinear arch behavior, for a downwards load. The nonlinear behavior starts from low load values, in comparison with the buckling loads of diagram 4.1. The material yields very early and the imperfections have no influence on the final collapse load.

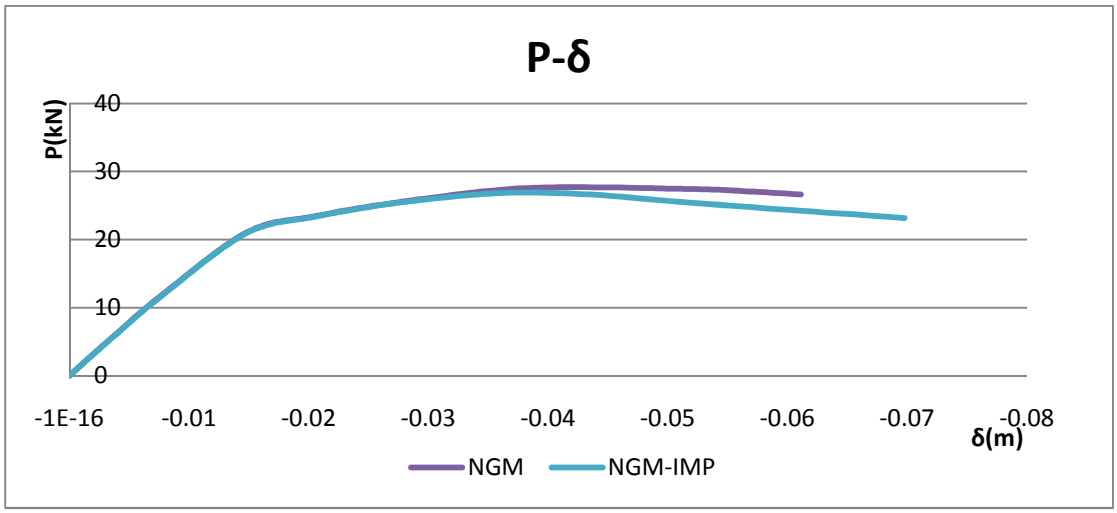

Diagram 4.3 Equilibrium path of high arch

Same results are shown in diagram 4.4, for the shallow arch under a downwards load. The imperfections, which are taken account, do not affect the critical load which varies in low load values.

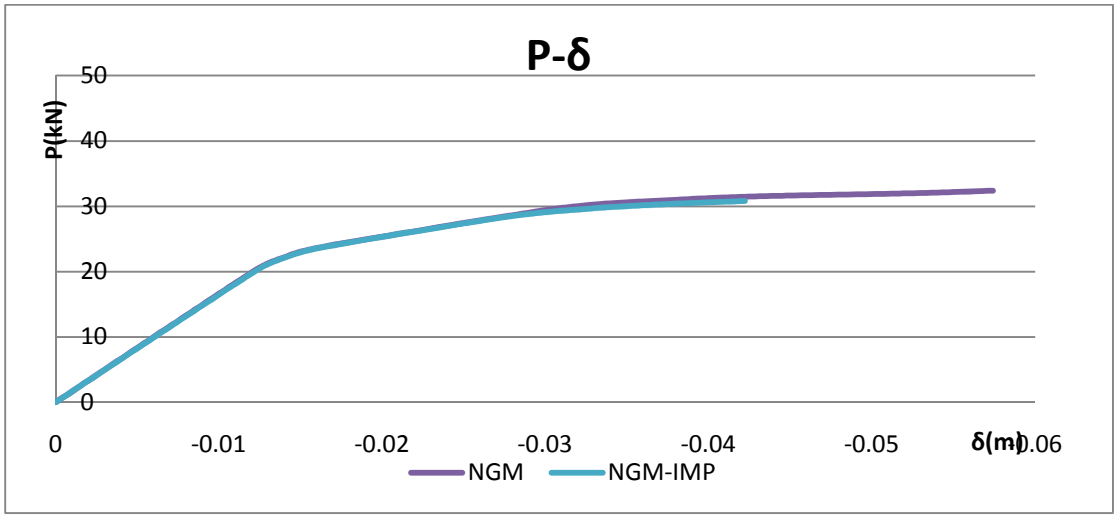

Diagram 4.4 Equilibrium path of shallow arch

Experiments are also carried out for an upwards load. A typical deformed shape for a tensional concentrated load at the middle of the arch is shown below.

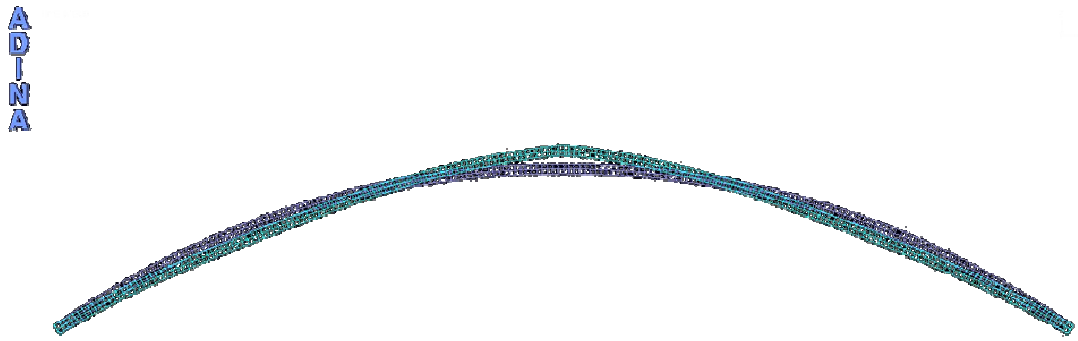

Figure 4.5 Deformed shape of shallow arch for the tensional load

The diagram represents the arch behavior under a tensional concentrated load. After the first plastic hinge in the middle of the span which occurs at 24kN, the high arch continues to be stiffened as a tension member, so the complete collapse occurs only when the steel cracks. The end of this experiment is subjective. The load values are extremely high in case of fracture, so the experiment will be terminated a little after the first plastic hinge.

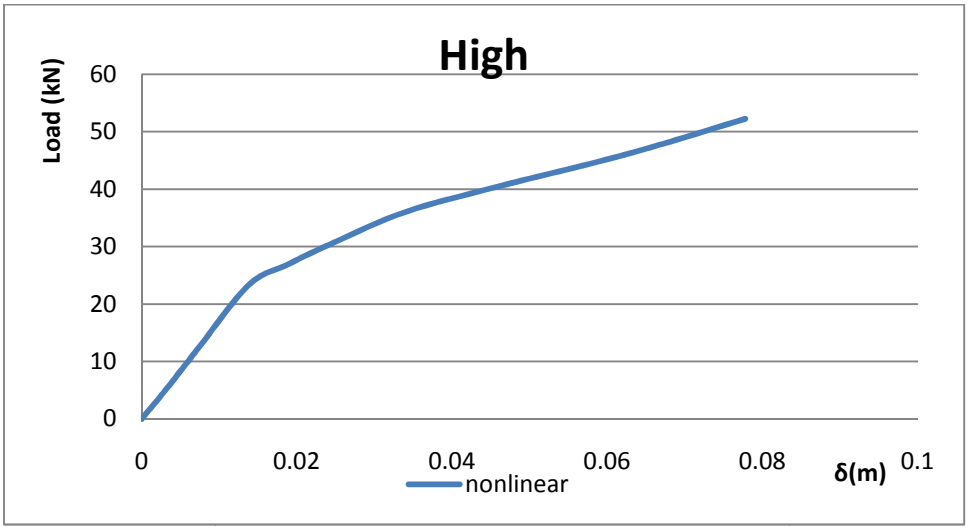

Diagram 4.5 Equilibrium path for high arch and tension load.

In diagram 4.6 one can see exactly the same results and conclusions for the shallow arch. A plastic hinge is developed at 28 kN and an upward path continues until the fracture of steel.

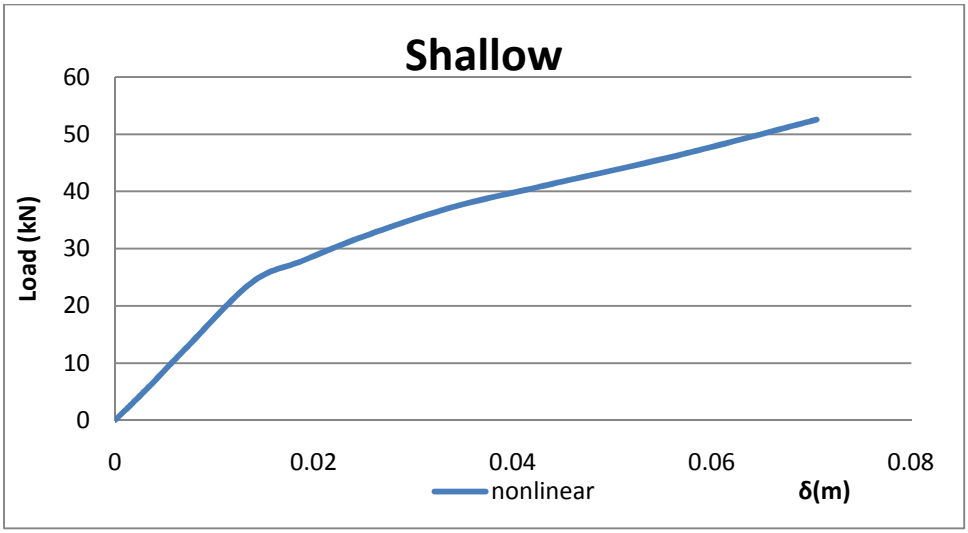

Diagram 4.6 Equilibrium path of shallow arch for a tension load.

4.4. Curving process

The initial goal of this paragraph is to simulate, in a simple manner, the curving process. In fact, a straight beam passes through bending rollers, which bend the beam and deform it, giving it the appropriate radius (see Appendix 2). In simulation of this process, prescribed rotations at the free ends of a straight beam are applied. Reaching the appropriate rotation, the arch is allowed to unload (or to spring-back, as referred in chapter 2). The unloading is completely elastic, in contrast to the loading process. After the unloading, the edges of the arch change into hinges and a prescribed concentrated displacement is applied, in small steps, at the crown.

Figure 4.7 presents the initial straight beam and the final curved beam of the curving process. Due to the unloading process, it is difficult to reach the appropriate radius of the arch; one or two trials are enough to complete successfully the process with the help of paragraph 2.3 and the relationship 2.66 about the final radius. These trials are used because the relationship is produced for an elasto-plastic material, while the model uses a material with strain hardening.

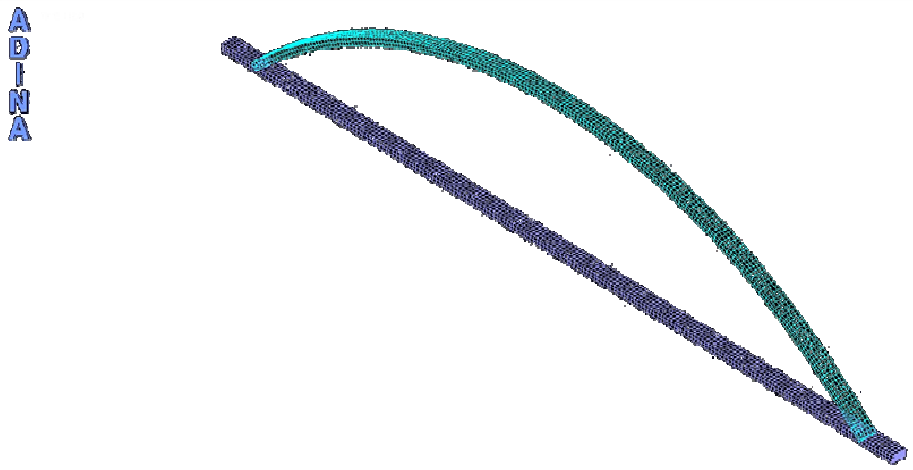

Figure 4.7 Straight and curved beam, before and after the curving process.

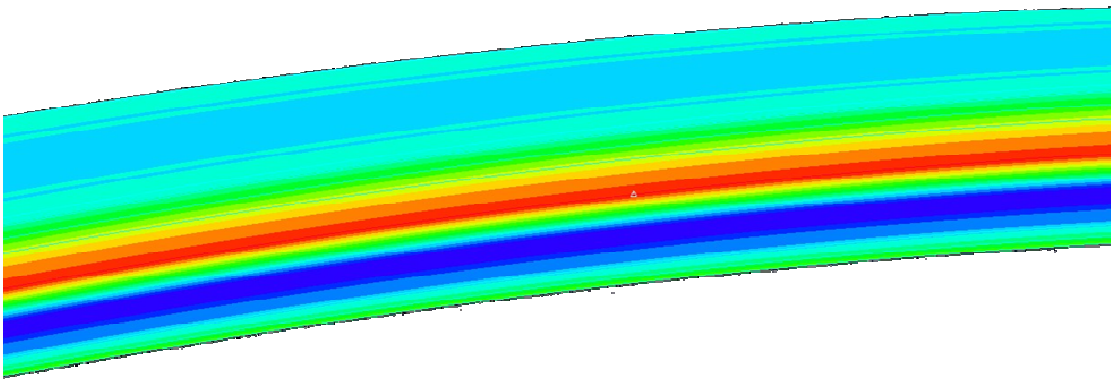

Figure 4.8 Contour of residual stresses from simulation

Figure 4.8 is a typical contour diagram of residual stresses. Theoretically, the residual stresses are the same in the whole member, except for its ends, due to the Saint- Venant principle. The red and blue colors indicate that the stresses have different sign. A more accurate diagram 4.7 is shown below. It presents the residual stresses in the height of section according to the theoretical method described in section 2.3 and from ADINA. The results of software ADINA have been extracted with linear interpolation at mid-surface of each element. Moreover, the diagram refers to the web of the section.

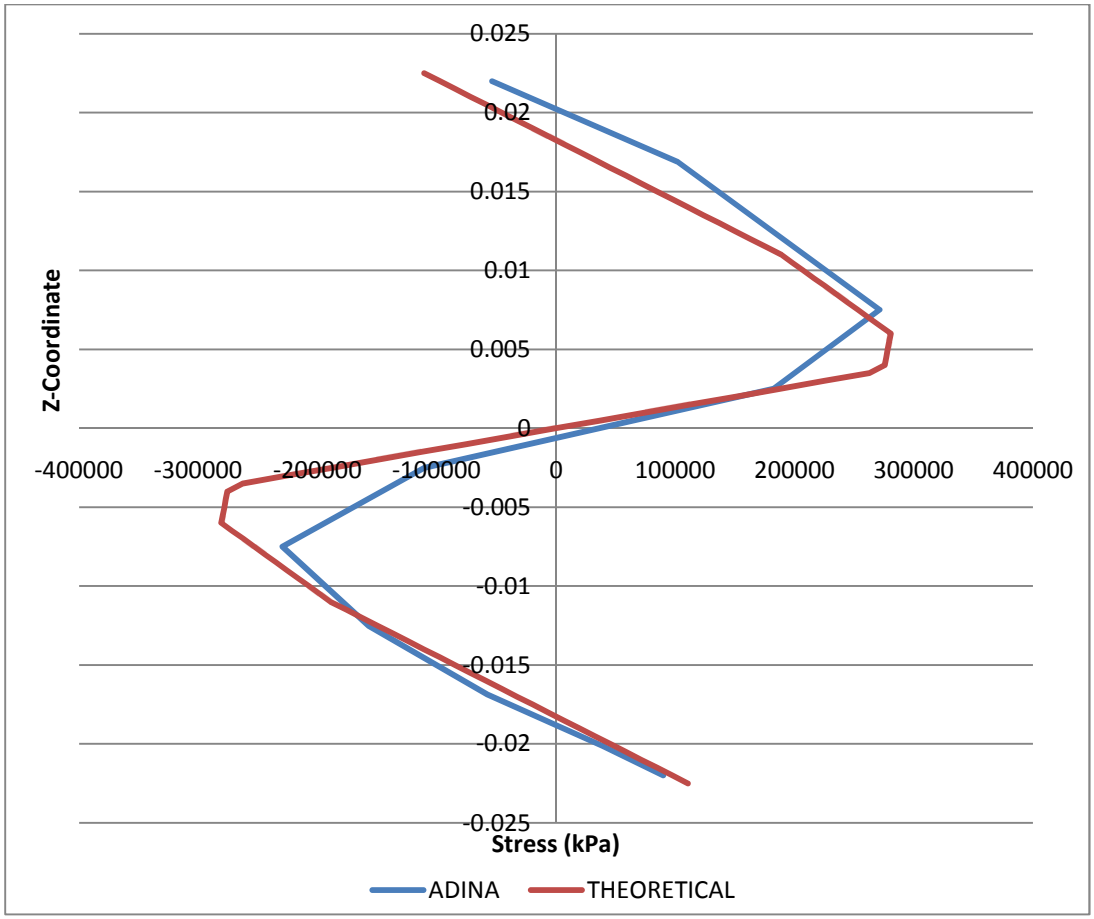

Diagram 4.7 Residual stresses in height of section

Diagram 4.7 presents some disturbances between the numerical and analytical curves. The differences are not significant, but there are interesting phenomena. As it is referred among the assumptions of paragraph 2.3 the neutral axis of the section is at the center of mass. However, having the opportunity to run an analysis according to the *large displacements/ large strains* theory, it is noticed that the neutral axis has been moved towards the center of curvature. This phenomenon is referred in the bibliography, firstly by Timoshenko and later by Roark et al., giving theoretically the accurate displacement of neutral axis.

5. Design of arches according to Eurocode3.

5.1. Generally

The design of arches is not well described in Eurocode3, but only with some references and guides at part 2 of Eurocode 3, about steel bridges. Although Eurocode is generally accepted for the design of buildings and other structures, it cannot be applied to special experiments, which demand extra accuracy. The current purpose is to estimate accurately, as possible, the critical strengths of the experiment- members. In spite of these, the design according to Eurocode 3(EC-3) is a very good initial point or a good approximation. The checks which must be made are about the bearing capacity of the cross section, that of the arch and that of the peripheral settings, like restrains and hinges. All are presented above.

5.2. Arch

5.1.1. Design Load

First of all, it must be calculated the situation in which the arches are subjected. It is considered that the structure is in the linear region, something that is a little far from the reality. Otherwise, the error which appears, does not exceed the 10%. So, a simple linear and elastic analysis of the given geometry results the lower down. The results refers to a vertical concentrated load of 10kN at the middle of arch and the final critical load, calculated multiplying these results with a final load factor.

Load P=10 kN	4.725-0.85(1st arch)	4.725-0.75(2nd arch)
Maximum moment (kNm)	2.76	2.814
Maximum axial force (kN)	11.66	13
Maximum shear force (kN)	4.928	4.926

TABLE 5.1 RESULTS FROM LINEAR ANALYSES

During the experiment both of compression and tension loads will be applied. The M, Q, N diagrams for the two different forces are the same, so all the results are referred to both loads.

Unfortunately, the material yielding makes the linear behavior completely wrong about the forces which are applied at the abutments. So, the forces with which we will design the abutment members will be resulted from nonlinear analyses, which appeared in chapter 3. Especially, the used loads in the checks below are referred to the maximum tension load, which appears in a nonlinear analysis, because these are the maximum magnitudes which are appeared.

5.1.2. Classification of section

The next step is to classify the cross section and to be ensured if a plastic analysis is possible. The geometric characteristics give a ratio *flange length/ thickness=16*. Using table 5.2 of part 1-1 of EC-3, for steel S235, the cross section is classified to class1. The class 1 of the section permits the use of a 2nd order nonlinear and plastic analysis.

$$c/t = 16 < 33 \cdot \varepsilon \tag{5.1}$$

Where,

$$\varepsilon = \sqrt{\frac{235}{f_y}} = 1 \tag{5.2}$$

5.1.3. Bending resistance

The first check is to verify the bending resistance of the section. Bending moment creates the main stresses in the section. According to paragraph 6.2.5 of EC-3-part 1-1, it must be

$$M_{Ed} < M_{Rd}, \tag{5.3}$$

Where

$$M_{Rd} = \frac{W_{pl} \cdot f_y}{\gamma_{M_0}} = \frac{0.00003258 \cdot 235000}{1.1} = 6.96 kNm. \tag{5.4}$$

$$M_{Ed} = 6.95 kNm \tag{5.5}$$

This bending moment appears due to a load of 25.4kN.

5.1.4. Axial resistance

According to paragraph 6.2.3 of EC3- part 1, the axial resistance of the section is given by:

$$N_{Rd} = A \cdot f_y / \gamma_{M_0} = 0.00137 \cdot 235000/1.1 = 292.68\text{kN} \quad (5.6)$$

The axial compressive force that corresponds the maximum bending moment to the arch is given by:

$$N_{Ed} = 40kN \quad (5.7)$$

So, $N_{Ed} < N_{Rd}$ (5.8)

and the check is correct.

5.1.5. Shear resistance

Next check is this of the shear force. The known maximum load gives also a maximum shear force equal to $V_{Ed} = 26kN$. (5.9)

The shear resistance of the cross section is given from the following formula:

$$V_{Rd} = \frac{A_v \cdot f_y}{\sqrt{3} \cdot \gamma_{M_0}} = \frac{0.000445 \cdot 235000}{\sqrt{3}} = 60.42kN \quad (5.10)$$

and it is:

$$V_{Ed} < V_{Rd}. \quad (5.11)$$

5.1.6. Combination

Besides, the interaction between moment and axial force and/ or shear force must be checked.

If the shear force is less than the half of plastic shear resistance, it is allowed not to reduce the moment resistance.

Equivalently, for the axial force and the major axis is:

$$N_{Ed} \le 0.25 N_{pl,Rd} = 73.33kN$$

and

$$N_{Ed} \le \frac{0.5 h_w t_w f_y}{\gamma_{M_0}} = 48.72kN \qquad (5.12)$$

And for the minor axis is:

$$N_{Ed} \le \frac{h_w t_w f_y}{\gamma_{M_0}} = 42.72kN \qquad (5.13)$$

Then, there is no reduction of the bending resistance due to the interaction of axial force and bending moment.

Finally, the load case which suppresses the arches gives such forces as do not have need of reduction at the resistance of cross section.

5.1.7. Buckling

According to the EC3- part2, paragraph D-3, the critical buckling load is derived for the following formulas:

$$N_{cr} = \left(\frac{\pi}{\beta s} \right)^2 EI_y \qquad (5.14)$$

Where

s is the half length of the arch

β is the buckling length factor (EC3, part2, table D-4)

EI_y is the in plane flexural stiffness of the arch.

The final critical buckling load does not exceed the 120kN. The real axial load of arches during the material collapse is far from the buckling load.

EC3, part2, table D-8 gives the initial imperfection which must be applied to the arch. Because of the restrains which offer out of plane stability, the imperfection which was used is the second mode, that of antisymmetric shape. The cross section is a cold forming rectangular hollow section and thus, the buckling curve for the RHS 100X50X5 is c. These data give a suggested initial imperfection of $a = L / 400 = 4.725 / 400 = 0.011m$. (5.15)

This imperfection has been considered during the analysis of an imperfect member.

5.2. Other elements

After the checks of the arch, it is necessary to make checks about the peripheral settings of the arch. It means checks for the hinges and restrains. Especially, we will check the plates, the pin, the welded connections, the bolted connections and the arch, locally at the hinges.

5.2.1. Design loads

The maximum critical load for the arch, between compression and tension, was calculated through a nonlinear analysis with imperfection of the 1st antisymmetric mode is about 40kN and is shown analytically in chapter 3. There is a disturbance between the critical load of EC3 and that of analyses by finite elements. It is preferred to use the maximum of the two different loads, in order to maximize the safety factor of the peripheral settings. In case of a collapse, it is necessary to happen at the arch and in any case at the non-replaceable peripheral members.

The current concentrated load (40kN) gives a horizontal force at the hinges of the arch about 51kN. This force suppresses the joints which connect the hinge with the laboratory frame, the welded connection between the plates of the hinge and the pin. The verification of the joints is described in EC-3, part 1-8.

5.2.2. Design of bolts

Table 3.3 of EC-3, part 1-8, suggests the maximum and minimum spaces of the holes in a joint connection. Respectively the table 3.4 gives specific rules about the design resistance for individual fasteners, subjected to shear and/or tension.

Failure mode	Bolts	Rivets
Shear resistance per shear plane	$F_{v,Rd} = \frac{\alpha_v \, f_{ub} \, A}{\gamma_{M2}}$ - where the shear plane passes through the threaded portion of the bolt (A is the tensile stress area of the bolt A_s): - for classes 4.6, 5.6 and 8.8: $\alpha_v = 0,6$ - for classes 4.8, 5.8, 6.8 and 10.9: $\alpha_v = 0,5$ - where the shear plane passes through the unthreaded portion of the bolt (A is the gross cross section of the bolt): $\alpha_v = 0,6$	$F_{v,Rd} = \frac{0,6 \, f_{ur} \, A_0}{\gamma_{M2}}$
Bearing resistance [1), 2), 3)]	$F_{b,Rd} = \frac{k_1 \, a_b \, f_u \, d \, t}{\gamma_{M2}}$ where α_b is the smallest of α_d ; $\frac{f_{ub}}{f_u}$ or 1,0; in the direction of load transfer: - for end bolts: $\alpha_d = \frac{e_1}{3d_0}$; for inner bolts: $\alpha_d = \frac{p_1}{3d_0} - \frac{1}{4}$ perpendicular to the direction of load transfer: - for edge bolts: k_1 is the smallest of $2,8\frac{e_2}{d_0} - 1,7$ or 2,5 - for inner bolts: k_1 is the smallest of $1,4\frac{p_2}{d_0} - 1,7$ or 2,5	
Tension resistance [2)]	$F_{t,Rd} = \frac{k_2 \, f_{ub} \, A_s}{\gamma_{M2}}$ where $k_2 = 0,63$ for countersunk bolt, otherwise $k_2 = 0,9$.	$F_{t,Rd} = \frac{0,6 \, f_{ur} \, A_0}{\gamma_{M2}}$
Punching shear resistance	$B_{p,Rd} = 0,6 \, \pi \, d_m \, t_p f_u / \gamma_{M2}$	No check needed
Combined shear and tension	$\frac{F_{v,Ed}}{F_{v,Rd}} + \frac{F_{t,Ed}}{1,4 F_{t,Rd}} \le 1,0$	

1) The bearing resistance $F_{b,Rd}$ for bolts
- in oversized holes is 0,8 times the bearing resistance for bolts in normal holes.
- in slotted holes, where the longitudinal axis of the slotted hole is perpendicular to the direction of the force transfer, is 0,6 times the bearing resistance for bolts in round, normal holes.

2) For countersunk bolt:
- the bearing resistance $F_{b,Rd}$ should be based on a plate thickness t equal to the thickness of the connected plate minus half the depth of the countersinking.
- for the determination of the tension resistance $F_{t,Rd}$ the angle and depth of countersinking should conform with 2.8 Reference Standards: Group 4, otherwise the tension resistance $F_{t,Rd}$ should be adjusted accordingly.

3) When the load on a bolt is not parallel to the edge, the bearing resistance may be verified separately for the bolt load components parallel and normal to the end.

Table 5.1 Design of bolted connections

For a bolt M8.8 the resistance is calculated from the formula:

$$F_{v,Rd} = \frac{a_v f_{ub} A}{\gamma_{M2}} = 122kN \qquad (5.16)$$

And

$$F_{b,Rd} = \frac{k_1 \cdot a_b \cdot f_u \cdot d \cdot t}{\gamma_{M2}} = 324kN \qquad (5.17)$$

The shear resistance of a connection of four bolts is $4F_{v,Rd} = 488kN$. The bearing resistance is also $4F_{b,Rd} = 1296kN$. The force at the hinges (51kN) is much less than the resistances of the connection and the safety factor on them is very high.

5.2.3. Design of the pin

EC-3, part 1-8, § 3.13 describes the design of a pin connection. Because of the small height of the cross section, the hole of the pin is necessary to have a low value of (maximum) 21mm. According to table 3.9, EC-3, part 1-8, the geometrical requirements for pin ended members are proposed as follows.

Failure mode	Design requirements
Shear resistance of the pin	$F_{v,Rd} = 0{,}6\, A f_{up}/\gamma_{M2} \geq F_{v,Ed}$
Bearing resistance of the plate and the pin If the pin is intended to be replaceable this requirement should also be satisfied.	$F_{b,Rd} = 1{,}5\, t\, d\, f_y/\gamma_{M0} \geq F_{b,Ed}$ $F_{b,Rd,ser} = 0{,}6\, t\, d\, f_y/\gamma_{M6,ser} \geq F_{b,Ed,ser}$
Bending resistance of the pin If the pin is intended to be replaceable this requirement should also be satisfied.	$M_{Rd} = 1{,}5\, W_{el}\, f_{yp}/\gamma_{M0} \geq M_{Ed}$ $M_{Rd,ser} = 0{,}8\, W_{el}\, f_{yp}/\gamma_{M6,ser} \geq M_{Ed,ser}$
Combined shear and bending resistance of the pin	$\left[\frac{M_{Ed}}{M_{Rd}}\right]^2 + \left[\frac{F_{v,Ed}}{F_{v,Rd}}\right]^2 \leq 1$

d	is	the diameter of the pin;
f_y	is	the lower of the design strengths of the pin and the connected part;
f_{up}	is	the ultimate tensile strength of the pin;
f_{yp}	is	the yield strength of the pin;
t	is	the thickness of the connected part;
A	is	the cross-sectional area of a pin.

Table 5.2 Design of a pin- ended connection

It is useful to have a replaceable pin, so another check must be satisfied.

$$\sigma_{h,Ed} \le f_{h,Rd} \tag{5.18}$$

$$\sigma_{h,Ed} = 0.591\sqrt{\frac{EF_{Ed,res}(d_0 - d)}{d^2 t}} \tag{5.19}$$

$$f_{h,Rd} = 2.5 f_y / \gamma_{M6,res} \tag{5.20}$$

Where:

d_0 is the diameter of the pin hole

d is the diameter of the pin.

The total force which is subjected to the pin, is the vector-summary of the vertical and horizontal force which suppress the arch. Especially, for the tension load which occurs the maximum forces:

$$F = \sqrt{V^2 + H^2} = \sqrt{51^2 + 23^2} = 55kN \tag{5.21}$$

The pin of the arch is a M20, 10.9, with a pin hole of 21mm diameter. The thickness of the connected plate, which belongs to the hinge, is 20mm, while the thickness of the cross section is 15mm (being reinforcement).

The shear resistance of the pin, is

$$F_{v,Rd} = 188kN \ge F_{v,Ed} = \frac{55}{2} = 27.5kN \tag{5.22}$$

The force is derived with two, due to the 2 shear planes of the pin. The bearing resistance of the pin and the plate (considering that the pin is replaceable) is:

$$F_{b,Rd,ser} = 0.6 \cdot t \cdot d \cdot f_y = 42.3kN \ge \frac{55}{2} = 27.5kN \tag{5.23}$$

The bending resistance of a replaceable pin is:

$$M_{Rd,ser} = 0.8 \cdot W_{el} \cdot f_{yp} / \gamma_{M6,ser} = 0.56kNm \tag{5.24}$$

The bending to which is subjected the pin is more complicated. It is calculated about 0.51kNm but it coexists with the shear force. The combined criterion is the following:

$$\left[\frac{M_{Ed}}{M_{Rd}}\right]^2 + \left[\frac{F_{v,Ed}}{F_{v,Rd}}\right]^2 = 0.85 \le 1. \tag{5.25}$$

The last check for the serviceability of the pin is the check of the contact bearing stress.

$$\sigma_{h,Ed} = 0.591\sqrt{\frac{EF_{Ed,res}(d_0 - d)}{d^2 t}} \le f_{h,Rd} = 2.5 f_y / \gamma_{M6,res} \quad (5.26)$$

5.2.4. Welded connection.

All the members of the experiment have welded connections. So, a check must be made for the force which each connection can transmit. The resistance is a function of the length of the weld. The EC-3, part 1-8, §4.5.3.3 suggests

$$\sqrt{\sigma_{\perp}^2 + \tau^2} \le f_{vwd} \quad (5.27)$$

Where:

$\sigma_{\perp}$ is the design value of the stress which is vertical to the weld.

τ is the design shear stress of the weld.

$f_{vw,d}$ is the design shear strength of the weld.

$$f_{vw,d} = \frac{f_u / \sqrt{3}}{\beta_w \gamma_{M2}} = 20.8 kN / cm^2 \quad (5.28)$$

where:

f_u and β_w are defined in 4.5.3.

The maximum force to which is subjected the welded members of the experiment is 55kN. This force is much higher from the resistance of the welded connections, the thickness of which has been chosen as 5mm.

Especially, the kinematic characteristics of the weld are given by:

$$I = 4 \cdot \frac{l^3 a}{12} = 4 \cdot \frac{(13cm)^3 0.5cm}{12} = 366 cm^4 \quad (5.29)$$

$$A_w = 4a \cdot l = 26 cm^2 \quad (5.30)$$

The forces on the weld are a horizontal force which creates shear and bending in the weld, while a vertical load creates tension in the connection.

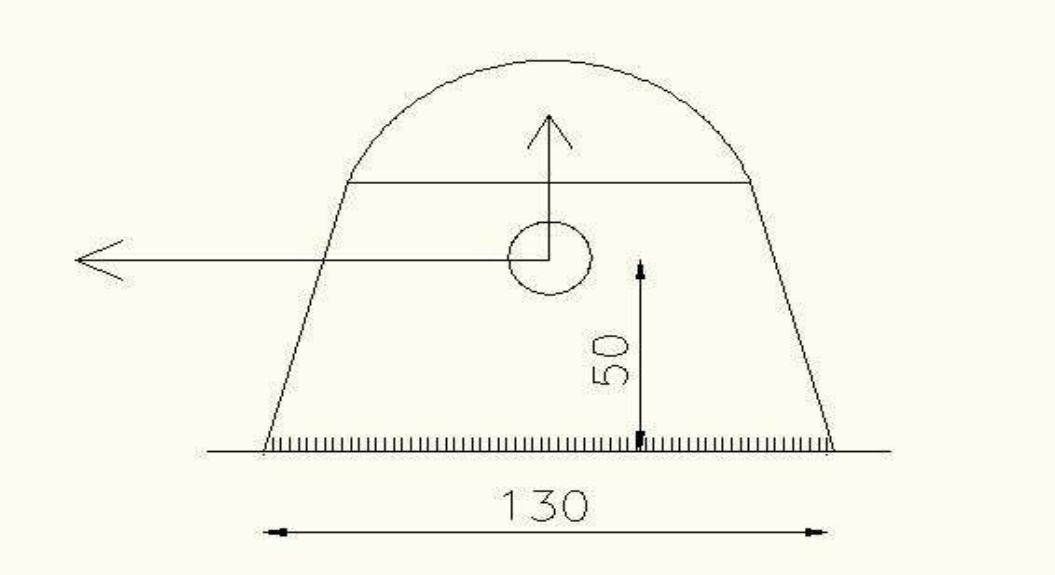

The horizontal force has the maximum value of 51kN and the vertical load 23kN. Thus:

$$\sigma_{\perp} = \frac{M}{I} z + \frac{N}{A_w} = \frac{51kN \cdot 5cm}{366cm^4} + \frac{23kN}{26cm^2} = 5.5kN/cm^2 \tag{5.31}$$

$$\tau = \frac{H}{A_w} = \frac{55kN}{26cm^2} = 2kN/cm^2 \tag{5.32}$$

$$\sqrt{\sigma_{\perp}^2 + \tau^2} \approx 7kN/cm^2 \le f_{vwd} \tag{5.33}$$

where:

$$f_{vw,d} = \frac{f_u/\sqrt{3}}{\beta_w \gamma_{M2}} = 20.8kN/cm^2 \tag{5.34}$$

6. Measuring devices

6.1. Introduction

In this chapter, a description of the measuring devices takes place. In other words, the characteristics, the used methods and the calibration process of each device are presented. This chapter is useful to assure the accuracy and the quality of the experimental results.

6.2. Measuring devices

6.2.1. Load cell

The main devices of this experiment are the load cell and the strain gages. The first one controls the load. The load cell is a transducer that is used to convert a force into electrical signal. The electrical signal output is typically in the order of a few millivolts and requires amplification by an instrumentation amplifier before it can be used. The output of the transducer is plugged into an algorithm to calculate the force applied to the transducer. The specific load cell of the laboratory has a maximum capacity of 300 kN. This device applies the concentrated load at the crown of the arch and therefore it is located at the middle of the laboratory- frame. Figure 6.1 shows the load cell and its location. The cables shown in the figure provide oil- pressure to the device. The accuracy of this load cell is 0.02 kN. The frequency of the taken data, via software, is 10 Hz that means 10 measurements per second. This frequency is selected, in order to reduce the error of the measurements due to the noise of the device.

The load cell can apply load or displacement to the arch, working in the same manner as described in the previous paragraph. For safety reasons, a displacement control method was selected, applying a specific displacement with a known rhythm. This rhythm is given via a *displacement- time* function, which shown in diagram 6.1. The purpose of this function is the initial loading, into the elastic region, with a low load value in order to eliminate all system imperfections. That means that the arch has to completely touch the hinges, the pins touch the plates and the load-plate touch the whole flange. After these, the arch is unloaded until the half displacement and is reloaded until a specific displacement, in which it is estimated that the arch will have been collapsed. After the collapse, the arch is completely unloaded. Between each change in the loading history, a plateau region exists to stabilize the measurements.

Figure 6.1 The load- cell

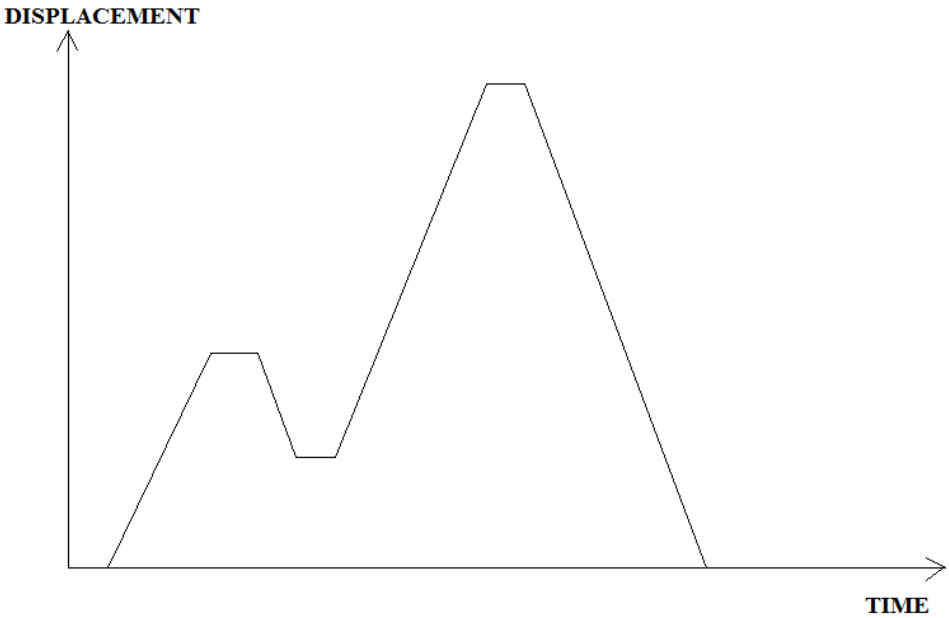

Diagram 6.1 Time function of the applied displacement

6.2.2. Strain gages

The next devices used are the strain gages. These measure the strain of steel at specific points, which have been selected on advance. In practice, the magnitude of measured strain is very small. Therefore, strain is often expressed in microstrains (μs), which is e x 10^{-6} strains. Therefore, the strain experienced by the test specimen is transferred directly to the strain gage, which responds with a linear change in electrical resistance. Strain gages are available commercially with nominal resistance values from 30 to 3,000 Ω, with 120, 350, and 1,000 Ω being the most common values. It is very important that the strain gage be properly mounted onto the test specimen so that the strain is accurately transferred from the test specimen, through the adhesive and strain gage backing, to the foil itself. A fundamental parameter of the strain gage is its sensitivity to strain, expressed quantitatively as the gage factor (GF). Gage factor is defined as the ratio of fractional change in electrical resistance to the fractional change in length (strain):

$$GF = \frac{\Delta R / R}{\Delta L / L} = \frac{\Delta R / R}{\varepsilon}$$

The gage factor for metallic strain gages is typically around 2.

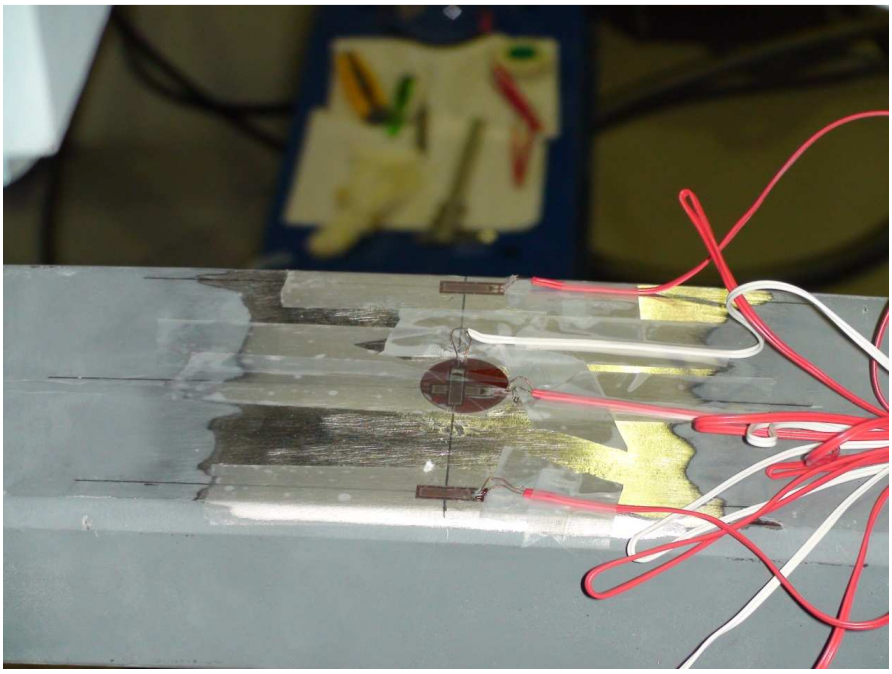

Figure 6.2 The strain gages

The normal procedure to verify the output of a strain gage measurement system relative to some predetermined mechanical input or strain is called shunt calibration. Shunt calibration involves simulating the input of strain by changing the resistance of an arm in the bridge by some known amount. This is accomplished by connecting a large resistor of known value (Rs) across one arm of the bridge, creating

a known DR. The output of the bridge can then be measured and compared to the expected voltage value. The results are used to correct span errors in the entire measurement path, or to simply verify general operation to gain confidence in the setup.

6.2.3. LVDT

Finally, five LVDT are used to measure the displacements on the arches at specific points. A first goal of this measurement is to have a general view of the deformed arch and to measure, if possible, the internal deformation of flanges. The linear variable differential transformer (LVDT) is a type of electrical transformer used for measuring linear displacements. In the experiment three LVDTs had a range of 10 cm and two of 20 cm. The error of these devices is 0.02 mm and there is the necessity of an appropriate device to calibrate these LVDTs. A mechanical micrometer, the accuracy of which is 0.002 mm, was used to calibrate the LVDTs. The measurements of LVDT were supposed to be zero at a specific point where it almost touches the micrometer. Giving a current value of displacement on the micrometer and comparing the measurements of the two different devices, the LVDT factor is calculated. Figure 6.3 shows one LVDT of the experiment.

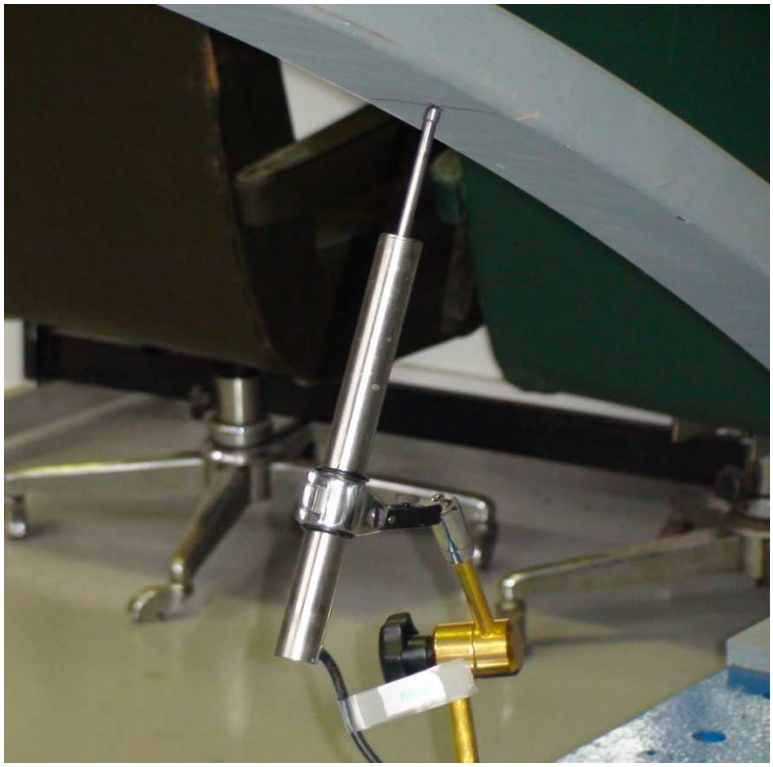

Figure 6.3 The LVDT

6.2.4. Tensile testing machine

Another significant part of the experiment is the tension tests of the material. The device is a special tensional-test machine, which works with the help of an extension-meter. Test pieces are screwed into or gripped in jaws and stretched by moving the grips apart at a constant rate while measuring the load and the grip separation. This data is plotted as load vs extension and then converted to engineering stress (load/original area) vs engineering strain. The extension meter measures the strain and the elongation of the tested specimen, while software converts these to load and engineering stress.

6.2.4. Other devices

The other devices used, are simply helpful for the experiment, but not necessary. These devices are two different cameras, the described micrometer, a measure and computers for the control of the experiment. The computers are shown in figures 6.4 and 6.5. Cameras are used to have a better control of the experiment, to record if something special happens and to have a complete view of the arch from the interior room. Measures are used to calculate the real imperfections of the arches, measuring the geometry of each arch at specific points and comparing to the theoretical perfect circular arch.

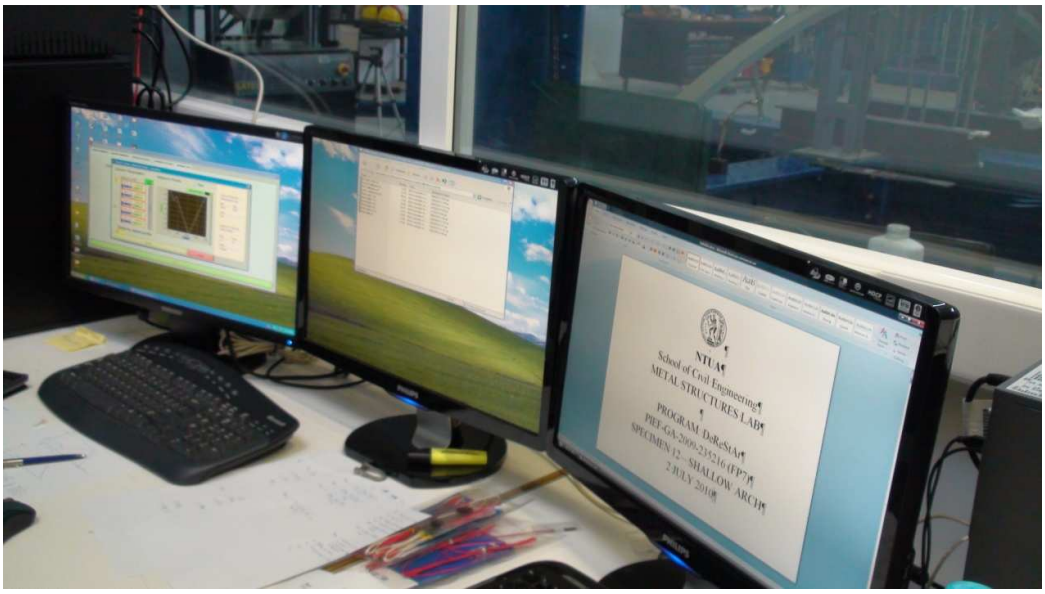

Figure 6.4 Screens of the computers on the interior room of the laboratory

Figure 6.5 The connection of the devices on the computers

7. Experimental results

7.1. Material tests

In this paragraph, a description about the material of the experiments takes place. Firstly, the theoretical model of a constructed steel is presented and secondly the results from the real material of arches. The stress- strain diagram of the real material is resulted with tension tests of specimens, taken from each beam before their curving.

7.1.1. Theoretical model

The chosen material of the experiments is an industrialized constructional steel S235. The quality of this steel was decided as described in paragraph 3.6. The estimated stress- strain diagram of this specific steel is shown in figure 7.1.

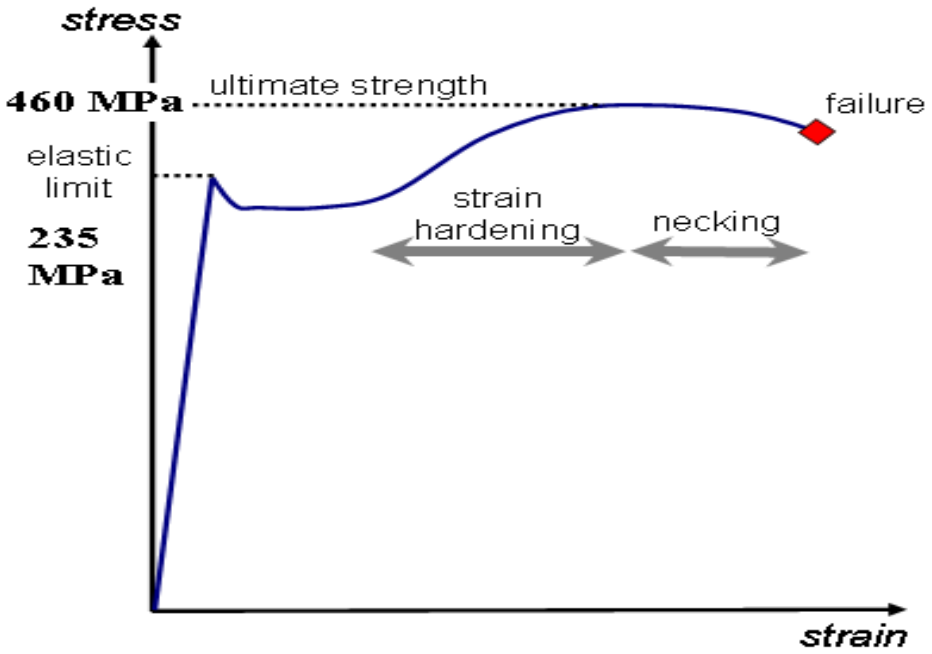

Figure 7.1 Estimated material law of Steel S235

The elastic limit will be at 235 MPa. A distinct yielding point is shown next to the elastic limit and after, a region of plateau and strain hardening should be presented until the necking and the failure of the specimen.

7.1.2. Material tests

In this paragraph the results of the experiments about the material stress-strain diagram are presented. To complete successfully the tension test, a necessity of having a perfect specimen according to a guide existed, in order not to have complicated phenomena to the measurements. The suggestions of DIN are the appropriate guide to construct the specimens for our tension tests.

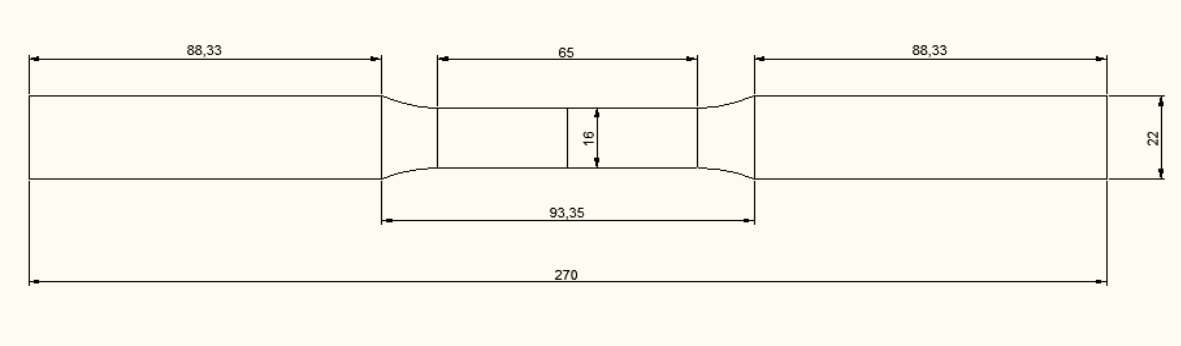

Figure 7.2 Geometry of the specimen

Figure 7.2 shows the dimension of each tested specimen. The length at the edges are some bigger than the minimum of DIN suggestions, to have a better friction between the specimen and the graps. The neck is identical to the minimum values of DIN rules.

The measurements of the experiment were made via an extensionmeter and two extra strain gages, only for the specimen 9, for better control of the results. The strain gages are placed into two different directions as a cross, in order to measure not only the stress- strain diagram but also to estimate the Poisson ratio. The results from the extensiometer and the strain gages are similar to each other and some different models are made to simulate the material more accurately at the analyses. A multilinear model is the appropriate to complete the numerical analyses succesfully. The results of this experiment and these simulations are presented in the following diagram 7.1.

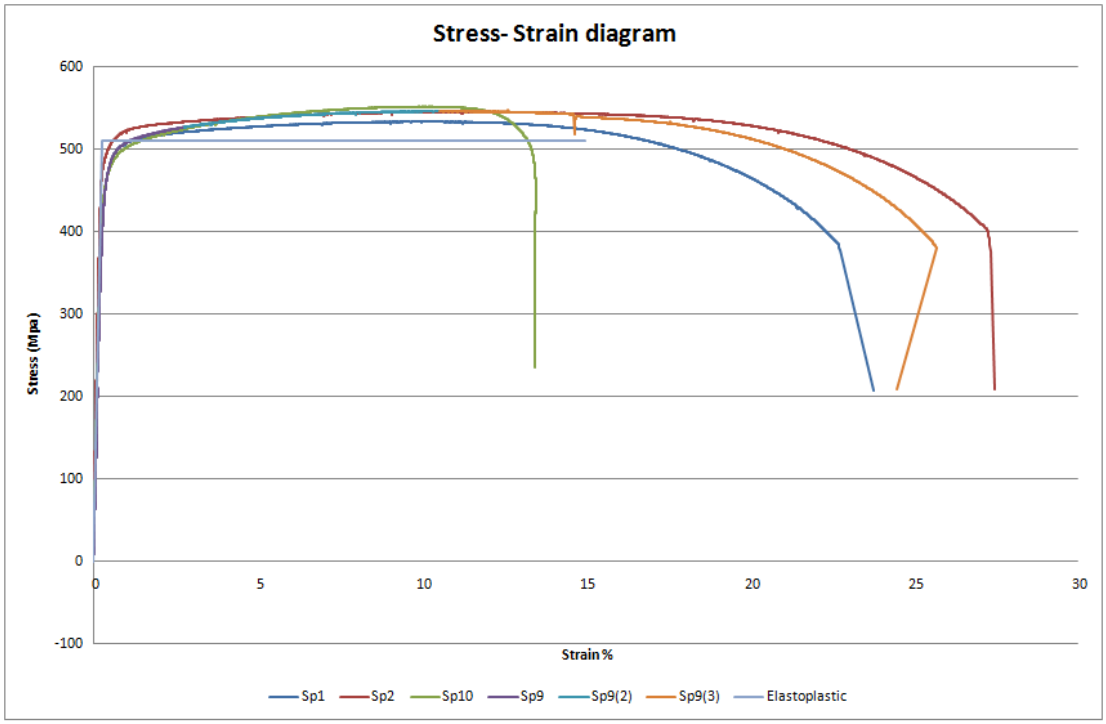

Diagram 7.1 Stress- strain diagram for the material tests

The previous diagram presents results which has no many similarities with the previous figure 7.1. The comments about these material results are:

a) The steel is not S235. The yielding point of this diagram is not easy-noticed, but due to the high fracture stress, at 550 MPa the material is for sure, a steel of higher quality.
b) The diagram does not present a distinct yielding point.
c) The diagram does not present a plateau region.

These notices create a difficult question about the properties of the real material. A first estimation about the quality of this steel is that it is an S355. The fracture stress of this (510 MPa) is very similar to the experimental fracture stress (550 MPa). As far as the notices about the absence of yielding point and plateau region is concerned, the hardening phenomenon is responsible. The steel during the cold forming process (to construct the section) and the curving process (to construct the arch) has entered very inside the plastic region. After these processes the steel is unloaded and returns to the zero stress point with significant residual strains. During the next loading process the material will follow another path, as indicated characteristically in figure 7.3.

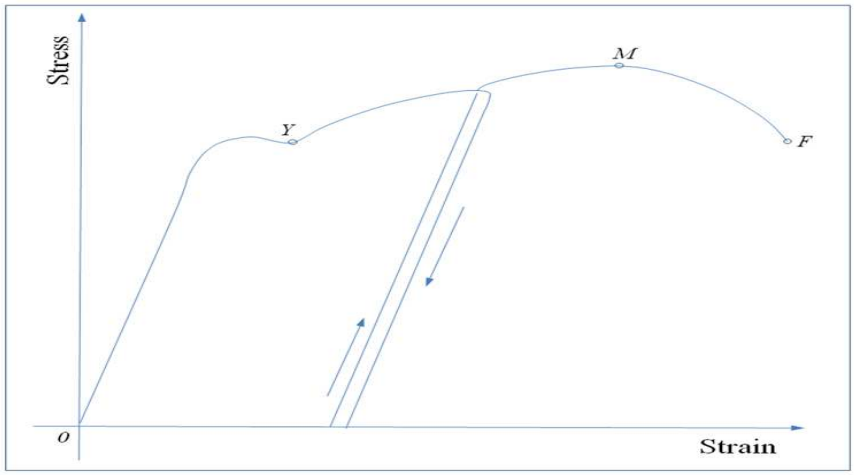

Figure 7.3 Stress-strain diagram for loading- unloading process

This figure indicates that the following path has overtaken the yielding point and the plateau region. Moreover, the yielding stress is shown to be higher than the initial one. This phenomenon is referred in the bibliography of earlier years, referring that the yielding stress is possible to be up to 7% higher than the initial- real yielding stress.

The bibliography explains completely the stress- strain diagram for our tensile tests. However, the yielding stress has yet not been found. It is difficult to see a specific point in which the material diverges from the elastic region. Eurocode 1 suggests that the stress corresponded to the strain 0.2% can be the yield point, at any tensile test in which it is not easy- noticed. This rule gives, from diagram 7.1- which has already been presented, a yielding point at 375 MPa. The decision about the Young modulus, exported from diagram 7.4, shows the initial elastic region of the tested specimens. The inclination of each line is similar to the others, fact that indicates a common Elastic Modulus of the material, yet the magnitude of this modulus is a complicated decision. The statistical dispersion of the elastic modulus, as a function of the selected results to calculate this modulus, is high enough to export a safe and typical value. The magnitude of the modulus ranges from 180 GPa to 270 GPa.

The last note on the stress strain diagrams is the negative strain- values on specimens 1, 2 and 9. The specimens of the arches are taken from a hollow rectangular section. These sections are constructed with a cold forming process. This process creates significant residual stresses and strains into the section as S.H. Li, G.Zeng, Y.F.Ma, Y.J.Guo and X.M.Lai have indicated. These residual stresses are responsible for the described hardening phenomenon as well. However, during the cutting of the specimen, a curving of this was appeared due to the residual stresses. The first values of strain referred to the process, where the specimen becomes straight. This fact is presented with the negative strain values on diagrams. The real tensile test is considered to begin after these negative strain values.

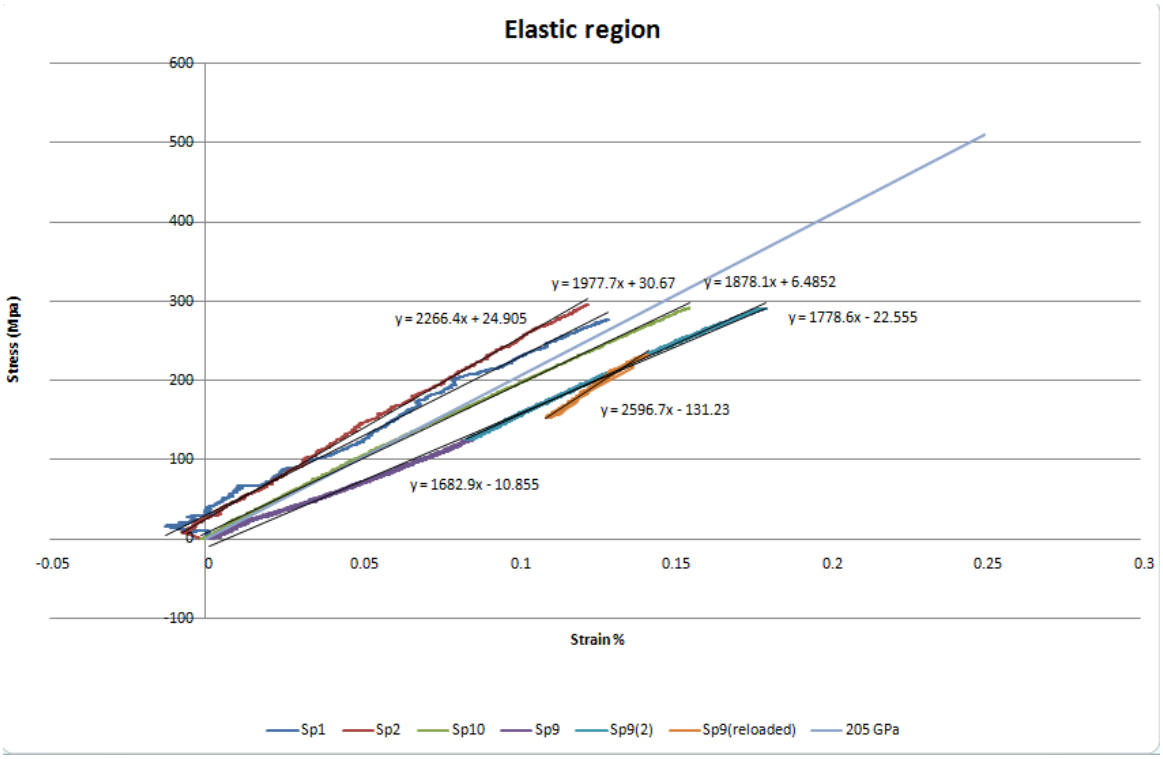

Figure 7.4 Elastic region of material tests

The elastic region of all the tested specimens seems to be similar the one to each other. In diagram 7.4 one can see the values of Young modulus of each curve and that of the decided elastic line, defined by a Young modulus equal to 205 GPa. The written equations from left to right show the elastic modulus of each curve as they are presented respectively, from left to right. Specimen 9 has been separated to three line and three elastic modulus values. The purple one refers to the whole resulted curve. Due to the unbalance of the results, the Sp(2) curve is presented, where the results of the specimens 9 seem to be normalized. Finally, the orange curve presents the unloading and reloaded process, which tested in the specific specimen. The elastic modulus for each curve is shown respectively. From all the presented values, the averaged one is decided to be the more representative for all the tested specimens; as already mentioned, this averaged value is equal to 205 GPa.

The final results of the material seem to be completely different to those of chapter 4. The pure elastoplastic material is far from the real material and the whole analyses of the previous chapter should be repeated with a more accurate material model. The new analyses include beam models analyses and shell models analyses. ADINA software asks a moment curvature diagram for the material law of the beam model. These diagrams constructed with respect of the relationships, given from Th. Papakonstantinou and Ch. Gantes for an elastoplastic material. Hence, the decision about a representative bilinear material law had to be taken. The properties of the decided bilinear model are shown in table 7.1.

Epsilon %	Sigma (MPa)
0	0
0.25	510
10	510

Table 7.1 Bilinear material model

Moreover, the model required for the shell models of ADINA software, is a multilinear model much closer to the real one and it is defined by the values presented in the next table 7.2.

epsilon %	sigma Mpa
0	0
0,182927	375
0,3	445
0,55	490
1,5	515
6	550

Table 7.2 The multi-linear description of material

During specimen 9, there was the ability to have an extra measuring device on the specific test. A strain gage, as a cross, is placed on the specimen in order to measure more magnitudes about the transverse and the longitudinal strains. In this way, one can estimate accurately the Poisson ratio with the ratio of the transverse and the longitudinal strains, as shown on diagram 7.5. In this diagram a trend line and its equation is also presented, with an inclination which represent exactly the Poisson ratio *v*. The equation of the trend line passes through zero point and it has an inclination equal to 0,3. The current value ensures the theory exactly, which shows the Poison ration of the constructional steel equal to the previous value.

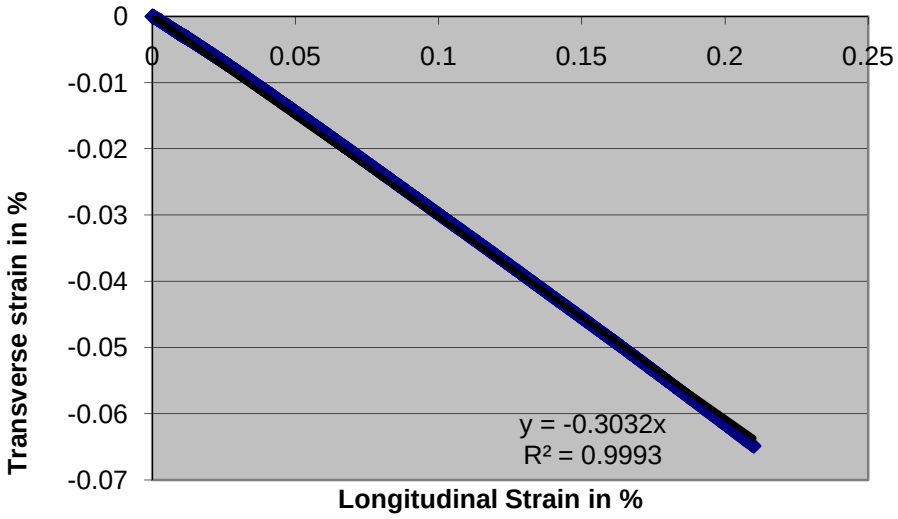

Diagram 7.5 Longitudinal- Transverse Strain

7.2. Tension tests

This part of the chapter presents the results from tension tests which took place in the laboratory. Six experiments were completed; three shallow arches and three high arches. All results are similar between them, with only some statistical differences. The whole results are presented and compared to the theoretical and numerical one. The latter includes analyses of shell elements in ADINA software, while the former, includes results from beam models via ADINA software, modifying with the relationships of the appropriate theory.

7.2.1. Global behavior

This paragraph presents results, referred to the total behavior of the arch; that means the deformations and the equilibrium path of the arch. Firstly, the equilibrium path of the arch is presented in diagram 7.6, which shows the relationship between the load and the displacement at the crown of the arch, as they are taken from the load cell-data, for all the tension experiments. The different colors show the curve of each arch. Three shallow and three high arches are investigated. The arches 7, 11, 12 are the high arches, while the rest are the shallow arches. Finally, the results from the beam models and shell models are presented for both high and shallow arches. The shell model refers to a two steps analysis. At the first step, a straight beam is curved, with prescribed rotation at its ends, until it reaches the given geometry, depending on the shallow or the high arch case.

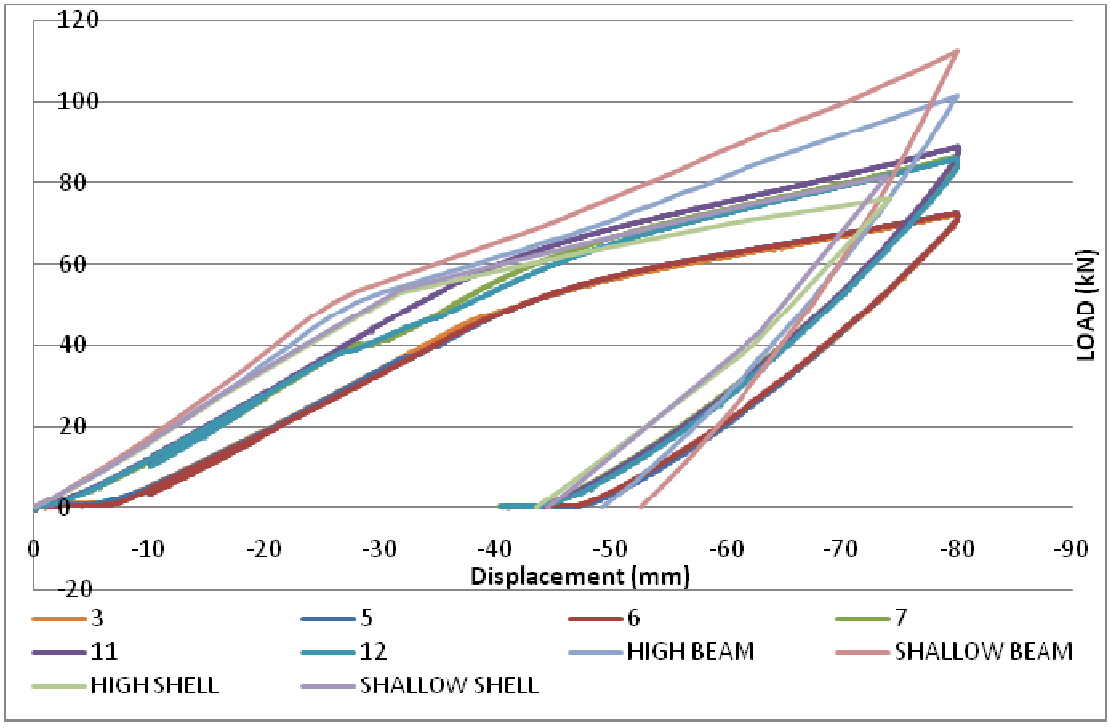

Diagram 7.6 Equilibrium path of arches

This diagram is a typical one as expected from chapter 4. A linear path is presented until the first plastic hinge occurs at the crown of the arch. This happens gradually about the 55 kN. Diagram indicates two teams of curves; three of the shallow and three of the high arches.

These curves from the experimental results seem to present an initial zero-inclination. This occurs mainly at the shallow arches. The specific phenomenon is presented due to the imperfect geometry and the flexibility of the arches and it is referred later, as sliding. The arches are not perfect constructed and they do not match completely to the laboratory frame, where the supports have already been placed. Thus, each arch suppressed, in order to be placed onto the hinges. When the pins passes through the holes the arch tends to return at its initial condition. So, the holes and the pins are not in a perfect touch in the right direction, such as to offer an external stiffness to the arch during the loading (see figure B.7). Hence, the first part of the loading is consumed to locate the arch in such a place, so all of the members to be completely touched and an external stiffness to exist in the arch.

The above phenomenon is responsible for the transformation of the curves far from the zero point. In this diagram, theoretical and numerical models are presented as well, but the comparison is difficult to be made due to this divergence. The shape of both theoretical and numerical models matches to the experimental ones. However, the beam models are characteristic, above all the rest curves, whilst the curves of the shell elements, are very close to the experimental. Beam models reach more load, since the local buckling of the flanges, which occurs after the plastic hinge, is impossible to be taken into consideration. Although the section is for sure a section of 1^{st} class, the local buckling happens because the deformations and the strains of the experiment are high enough. This phenomenon is well understood from the shell model, and that is why, it converges to the experimental in each case-that of the shallow and that of the high arch. In the diagram the shell model- curves are above the experimental curves, due to the sliding of the arches, which transform the curves.

Diagram 7.7 is referred to the longitudinal strain- displacement path of the arch. The results are taken from strain gages which are placed next to the point of loading and at the middle of the upper flange. Strain gages are also placed at the edges of the section; however the results are extremely similar to this of the middle one. The displacement is taken from the load cell data and it is referred at the crown of the arch. Each curve appears an ascending part, the inclination of which is continuously reduced. After a specific displacement the strain is reduced as well; this happens due to the redistribution of the stress and strains after the completely creation of the plastic hinge at the crown. This behavior is presented in the shell models results, the material law of which is the accurate. In contrast, the beam models maintain the maximum strain value, since the local buckling at the plastic hinge does not occur. Moreover, the maximum theoretical and numerical strain values are less than the measured one. It is owed partially to the sliding phenomenon, which creates some initial and significant strains.

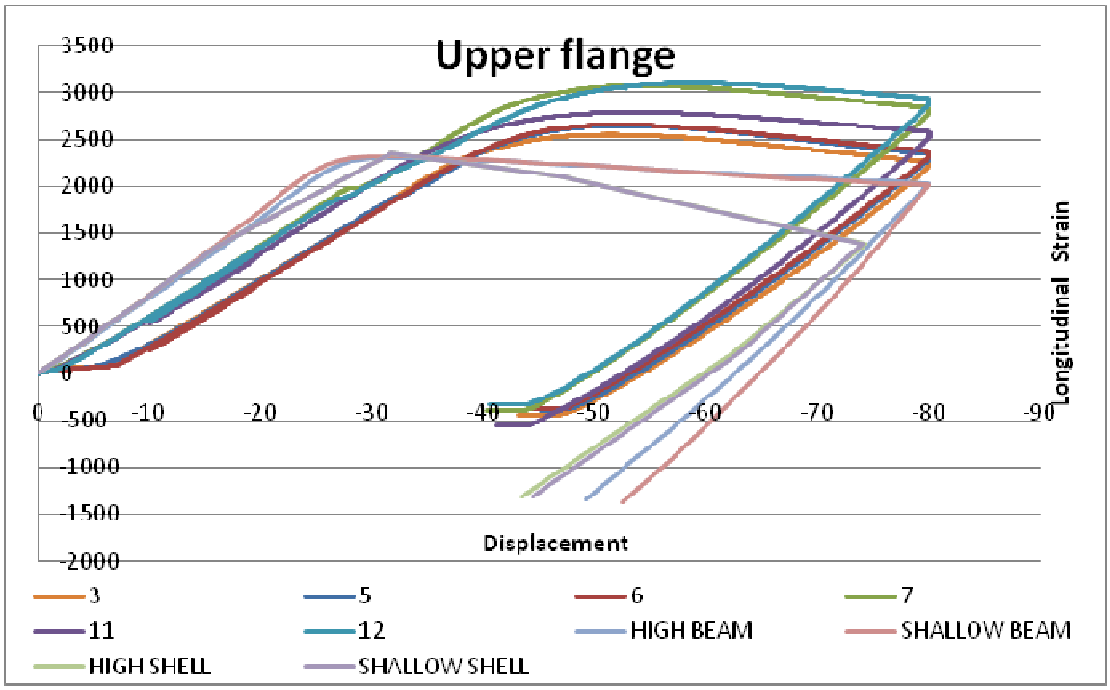

Diagram 7.7 Longitudinal strain- Load for upper flange

The same results of longitudinal strain- displacement of the arches about the lower flange are shown in diagram 7.8. The shallow arches present all together the same behavior, while the high arches 7 and 12 have very close results, in comparison with the specimen 11, where the differences are significant.

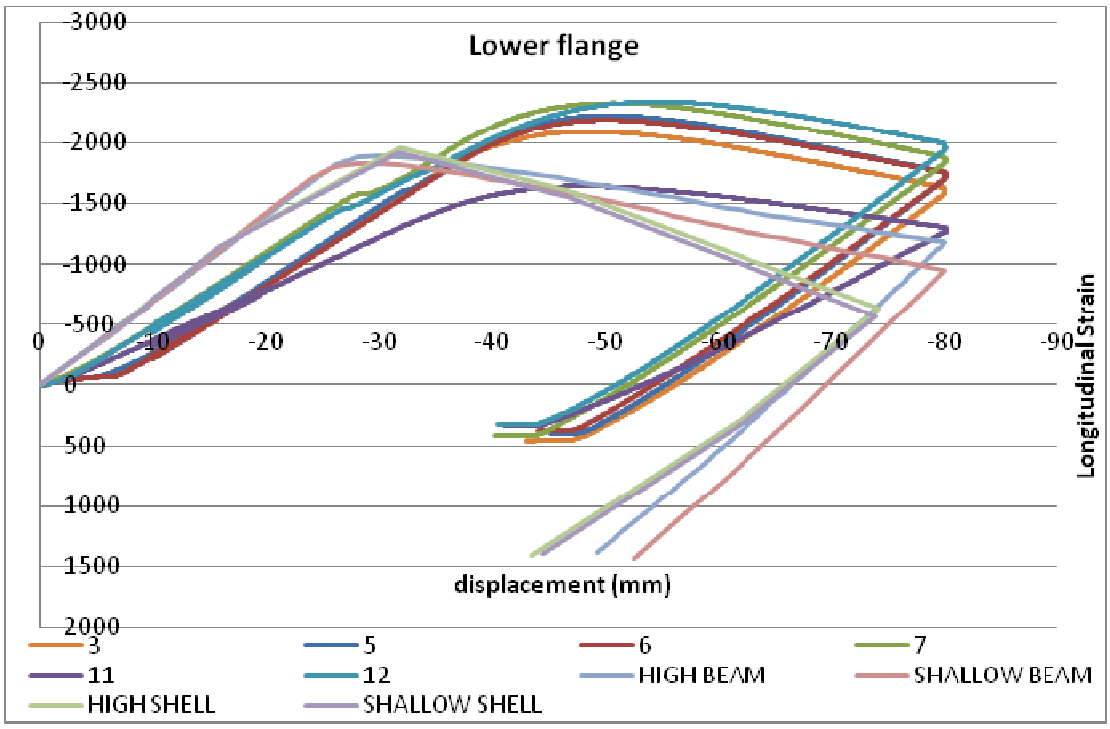

Diagram 7.8 Longitudinal strain- Load for lower flange

7.2.2. Local behavior

In this paragraph, results about local phenomena are presented. The relationship between the out-of- plane orthogonal strains and the in- plane main strains is presented, while the distribution of each strain during the experiment is given as well.

Diagram 7.9 presents the path of the transverse strain for the upper flange during the loading history. The different strains are taken from the middle of the flange, because in this location there is the maximum estimated value of transversal (out-of-plane) strain, as it is calculated from relationship (2.56). The measurements were taken from strain gages, as shown in figure 6.2. The displacement of each diagram is that of the crown of the arch, taken from the load cell data. The theoretical curves from beam models have been constructed from the longitudinal strains of the model multiplied with a linear factor resulted from relationship (2.56). The shell model curves are closer to the experimental because they may take into consideration the nonlinearities of the real relationship between the out of plane and the in plane strains. Nevertheless, all the diagrams are similar to each other, especially on the initial elastic part. Due to the more accurate material law of the shell models, these follow better the real curves.

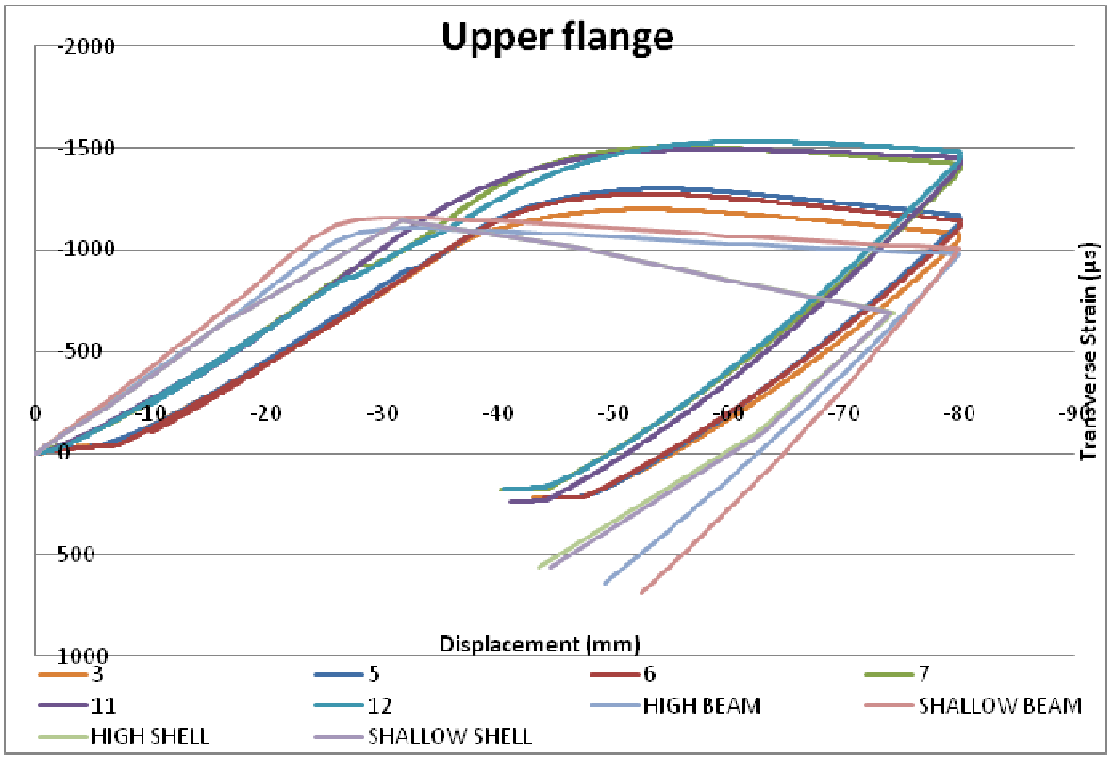

Diagram 7.9 Transverse strain- Displacement for the upper flange

The same conclusions are extracted for the next diagram 7.10 about the transverse strain- displacement of the lower flange. All curves have a same initial elastic part, which is curved in all the curves except from that of beam models, the curves of which is a direct function of the main longitudinal strains.

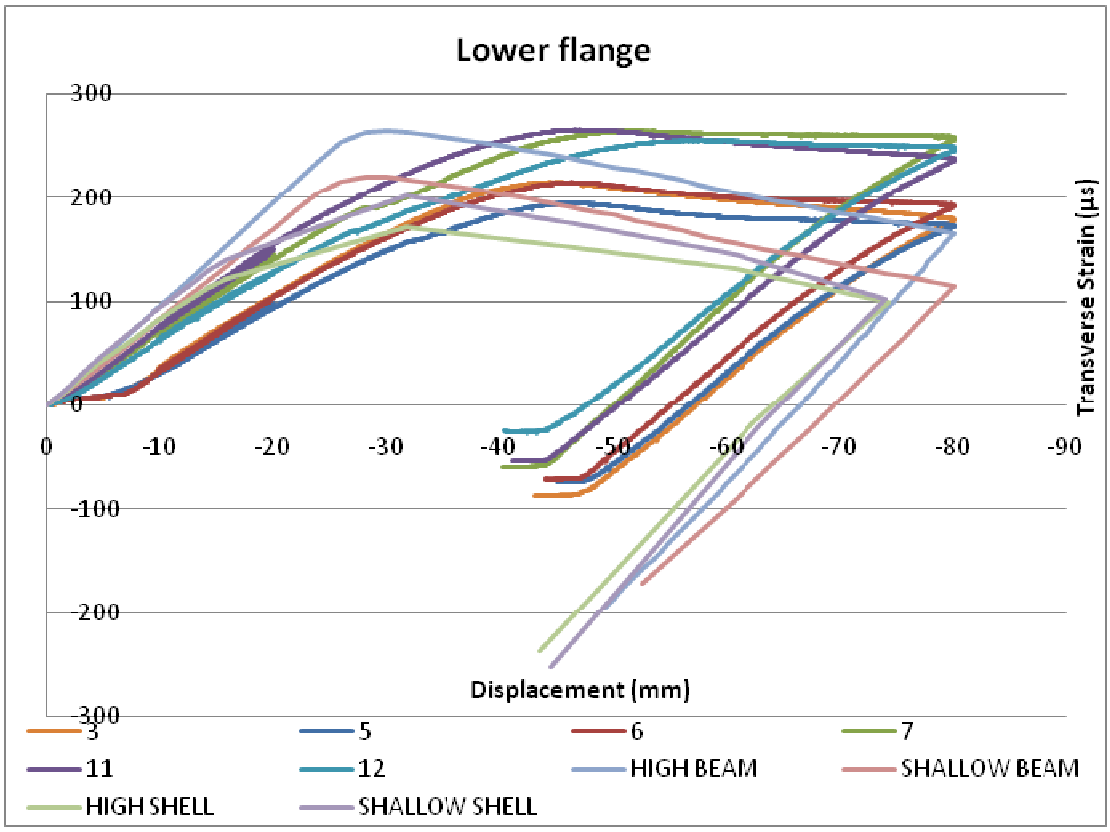

Diagram 7.10 Transverse strain- Displacement for the upper flange

Diagram 7.11 shows the relationship between the transverse and the longitudinal strain of the section. These strains are referred to the flanges of the section and they are taken from the middle strain gage which already exists there. In this point the out of plane – transverse strain is estimated in its maximum value. The diagram includes the curves from the experimental results and that of the shell (numerical) and the beam (theoretical) models. The beam models- curves has been resulted via the equation 2.56 with the longitudinal strain known from the beam models results. In this diagram one can notice the convergence of all the curves. The relationship between the two different strains is linear, so the beam models may follow these accurately. The inclination of each curve represents the value of the parenthesis of equation 2.56, and it ensures the validity of our calculations. The only diverged point is the high negative values of the strains, in the numerical and theoretical models, during the unloading process, which does not exist to the

experimental results. Finally, the inclination of the shallow arch curves is 0.48 and that of high arches 0.5, as expected.

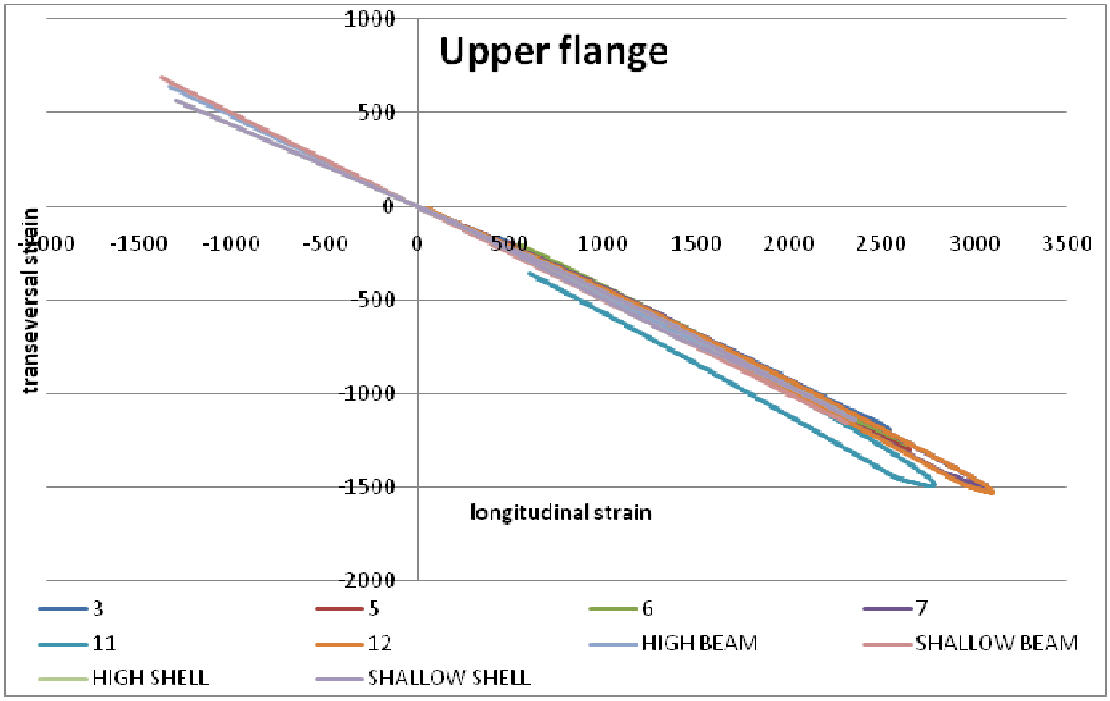

Diagram 7.11 Longitudinal strain- transverse strain for lower flange

The same results are presented in diagram 7.12 for the lower flange. The curves are the one close to each other. The inclination of each curve is similar for the shallow arches of the experiments and of the theoretical and numerical models. It is noticed that this is exactly the same conclusion for the curves of high arches.

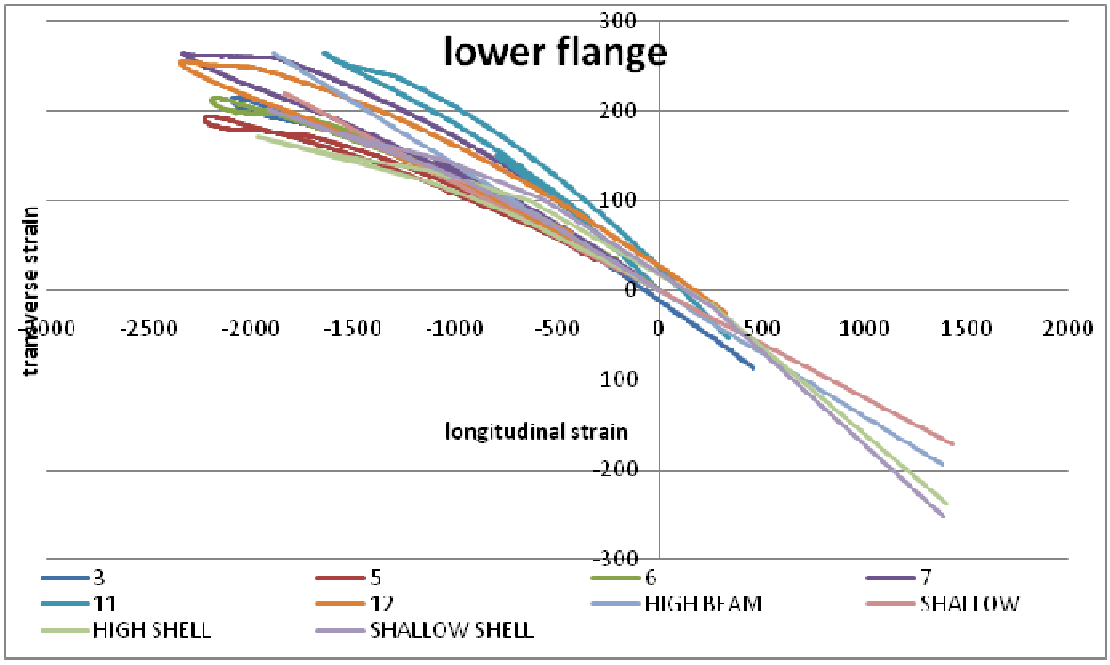

Diagram 7.11 Longitudinal strain- transverse strain for lower flange

The qualitatively differences between the two diagrams o f the upper and the lower flange is the curving of the lines. The relationship between the transverse and the longitudinal strains do not remain linear, as in the case of the upper flange. During the loading the internal to the curvature flange, enters more quickly to the plastic region, where the Poisson ratio, which affects directly the relationship of the two strains, changes from 0.3 to 0.5, as it is referred in bibliography. Another reason of this curving is the continuous change of the arch radius. Due to the extreme deformations of the experiment, the radius of the arch is also extremely changed. This term is on the denominator of the relationship 2.56 and creates changes in the parenthesis values. However, although the beam models curves remain linear, the shell models curves follows exactly the experimental results.

7.2.3. Figures of deformed arches

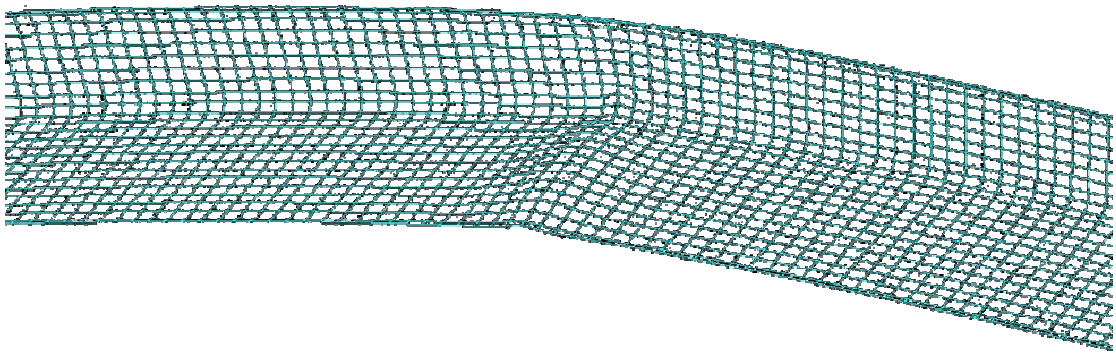

Figure 7.4 The deformed arch after a tension test

Figure 7.4 shows the section of the arch after the end of a tension test. This picture refers to the loaded point, where a local buckling has already been occurred after the plastic hinge. Same situation is regarded at the real experiment in the same time.

7.3. Compression tests

This paragraph presents the results, as above, for the tests where the load were downwards. These tests are called compression tests, because the axial force of the arch is the mainly compression. The results present not only similarities but also significant differences. Theoretical results are also compared to the experimental results. Numerical models are investigated with ADINA software and the shell and beam elements.

7.3.1 Global behavior

Firstly, results from the global behavior of the arch are investigated. It is important to see the behavior of the arch under the load before checking the internal elements like strains. Diagram 7.12 presents the equilibrium path for all the compression tested arches. They are three shallow and three high arches. The results are shown below together with the results from a shell model and a supplementary of beam model.

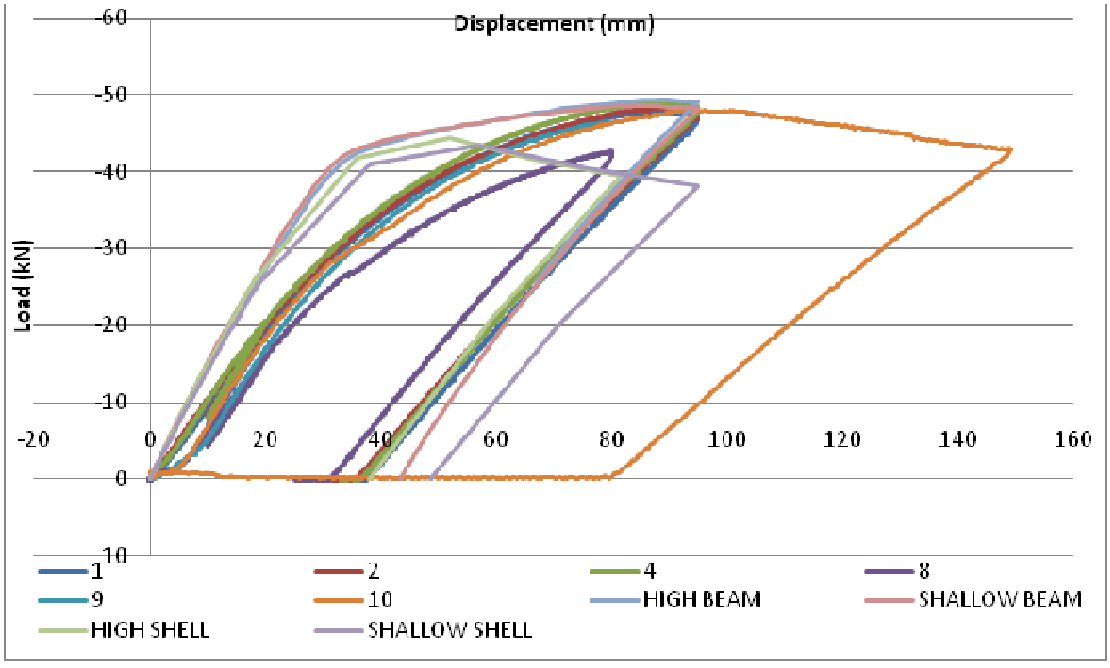

Diagram 7.12 Equilibrium paths for compression tests

The different colors present the different specimens. Arch 10 and 8 seem to be irrelative to the others. In the case of specimen 10, its behavior is very close to the others, but the final displacement in which the test stopped, differs. It is the first tested specimen. After this test the current final displacement, was considered exaggerated. Thus, it was decided to terminate each test at a displacement of 95 mm.

Moreover, during the test of arch 8 a problem on the time function appeared and the load cell applied the load in a faster way. The test was terminated violently and the results could not be considered static. The theoretical results from the beam models and the numerical results from the shell models show a common behavior, more stiffen than the real one. Moreover, the beam models reach the maximum strength of the arches, instead of the shell models. Shell models lost the stiffness after the plastic hinge due to a local buckling, occurred from the way, in which the displacement is applied. This is under investigation.

The next diagram, 7.13, shows the longitudinal strains, as given by the middle strain gage of the upper flange and the displacement of the arch at the crown, according to the results of the load cell. In this diagram the separation between the shallow and high arches is clear. The curve of arch 8 presents a strange behavior, due to the violent termination of the test.

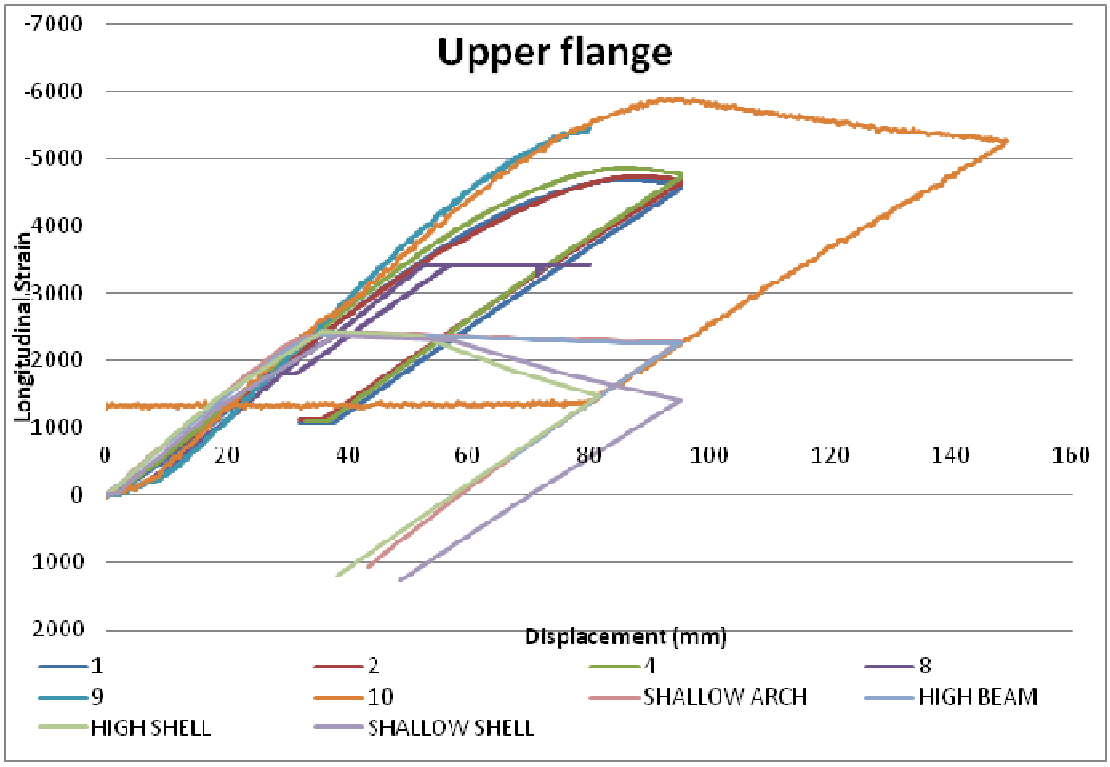

Diagram 7.13 Longitudinal strain- Displacement for the upper flange

Diagram 7.14 presents the same results as previous for the lower flange. The results are taken again from the middle strain gage of the lower flange. In this diagram the separation of the shallow and the high arches is difficult enough. Qualitatively the results seem to be similar to the previous of the upper flange. The curve of arch 10 presents some waves; this unbalance of the results is presented due to the noise of the measurements. Arch 10 was the first tested specimen and the frequency of the taken results was small enough. This problem was noticed and corrected in the next tests. The theoretical and numerical curves seem to move very close to the experimental curves, but the extreme values of the diagram present a significant difference. One

can calculate these differences about 100% or more. This remarkable difference is presented in all diagrams and the reason is not known yet.

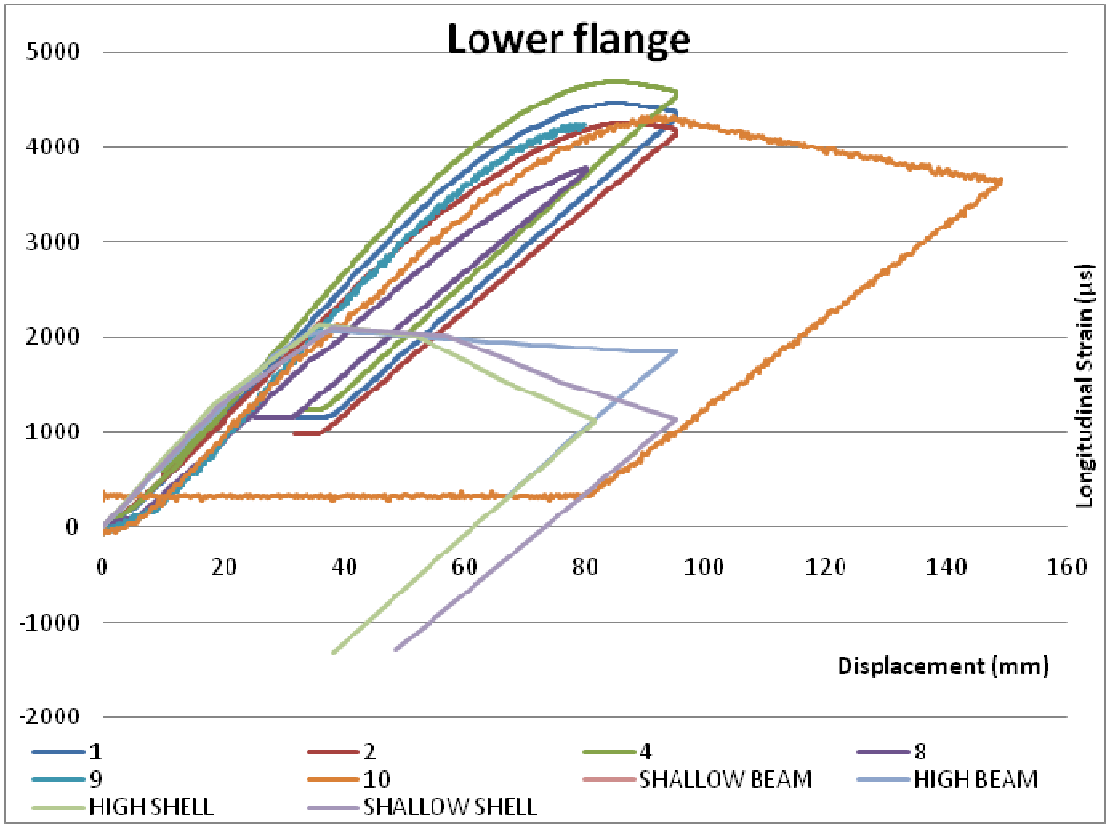

Diagram 7.14 Longitudinal strain- Displacement for lower flange

7.3.2 Local behavior

This part of the chapter presents the results at a local level of the arches, for the compression tests. That means the behavior of the section during the loading history. What it is important for the section in this thesis, is the transversal strains, out of plane of the arch. These strains are taken from the strain gage at the middle of the flanges, where these strains are estimated to be maximized.

Diagram 7.15 shows the transverse strains of the upper flange in a function to the crown displacement. Qualitatively, the curves of the experimental and theoretical and numerical results are similar. However, the extreme values are not comparable. Initially all diagrams present the same inclination, until the curving of the experimental curves, which are very close followed by the numerical curves. Shell elements can include exactly what affect the transverse strains. Regarding the unloading section of the diagram, one can see the similarities of the inclination of all the presented curves. This is extremely helpful, because the initial part of the curves is not directly comparable, due to the sliding, described in previous paragraph.

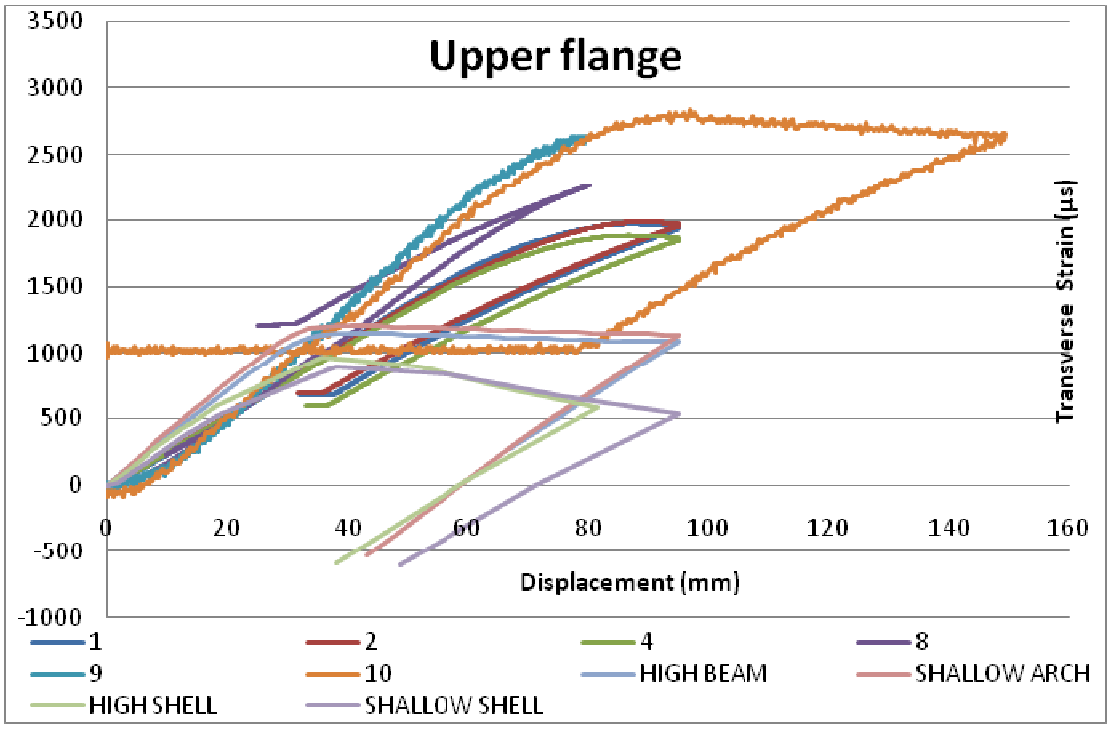

Diagram 7.15 Transverse strain- Displacement for the upper flange

Regarding the diagram 7.16 one can understand the same conclusions, as above. The inclination of the curves gives a qualitatively similarity, in contrast to the quantitatively differences in the maximum values of the transverse strains.

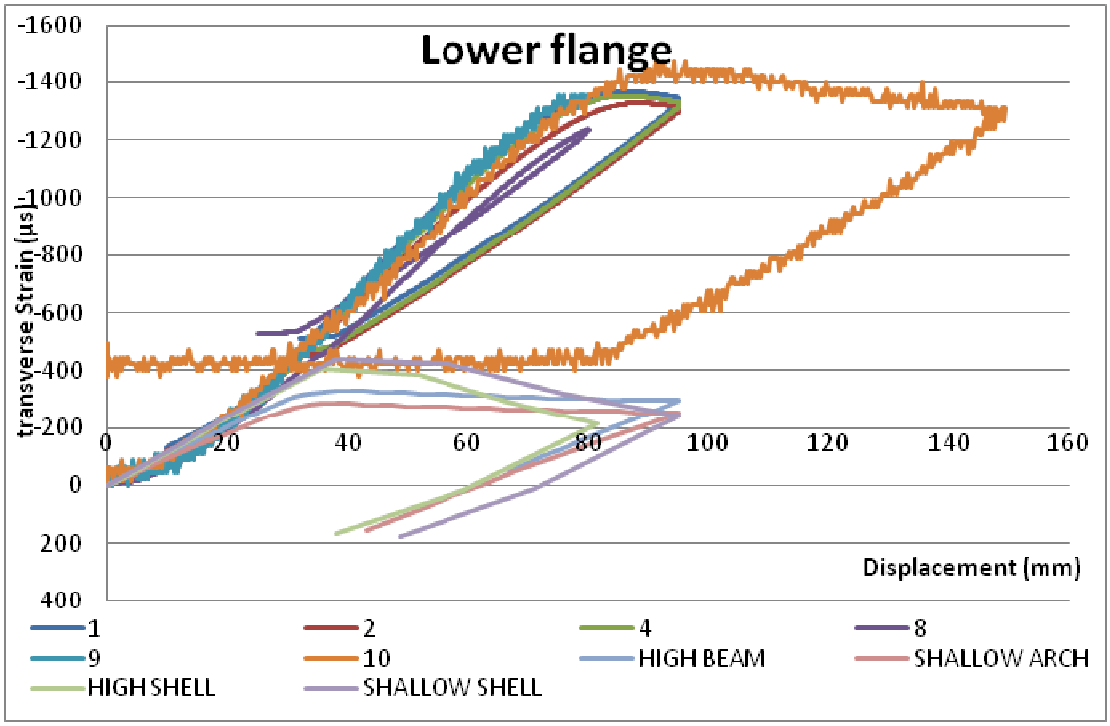

Diagram 7.16 Transverse strain- Displacement for the lower flange

Diagram 7.17 shows two different teams of curves, one about the transverse strains and the other about the displacement applied at the crown. Those of shallow and high arches have some differences in the inclination of their curves. The value for the shallow arches reaches the 0.47, while that for the high arches is about 0,5. The internal differences between the shallow arches and those of the high arches are explained due to constructional imperfections of the arches. The thickness of the section, the radius of each arch and the external dimensions of the section has some differences due to the cold formed processes of the curving and the cold- formed section- construction. The curve of arch 8 is strange due to an incorrect range of strain gages and the violent termination of the test. The numerical and the theoretical curves are assured by the experimental results. Qualitatively the curves are similar one to each other, however, regarding the extreme values, they differ as already has been described.

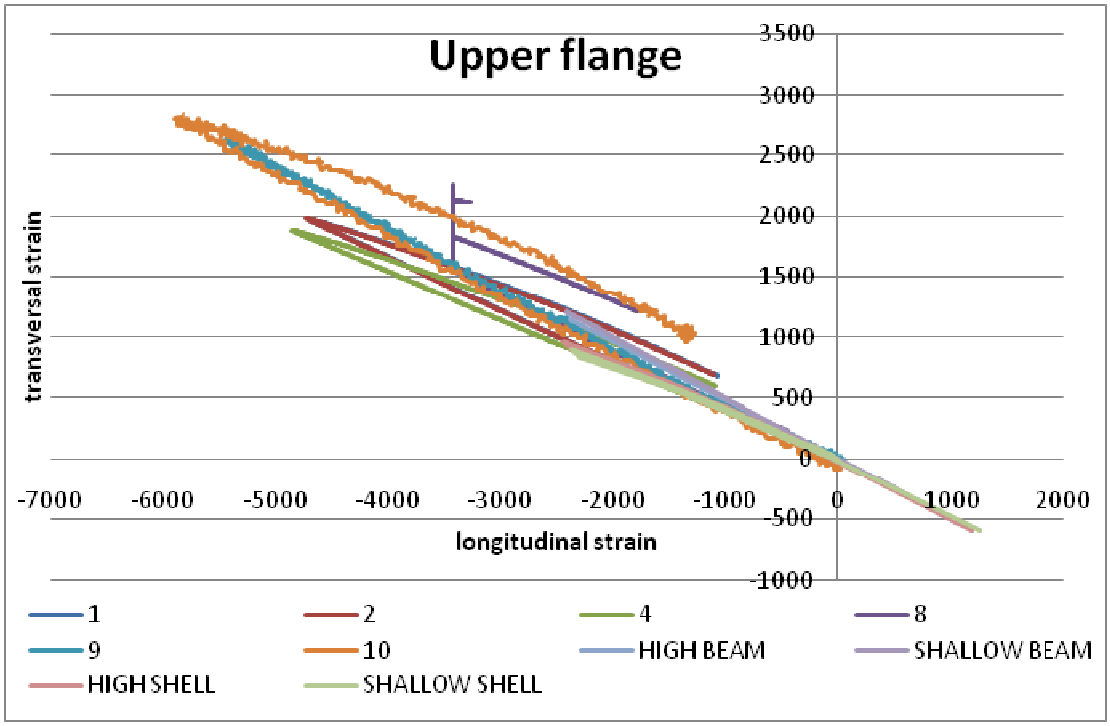

Diagram 7.17 Longitudinal- transverse strain for the upper flange

The same diagram and conclusions are about the lower flange, in diagram 7.18. A curving of all the lines is noticed, in contrast to the previous diagram, where the lines remain approximately linear. The fact that the lower flange enters more quickly the plastic region, changes the Poisson ratio and the diagrams are presented curved. The value of the first- loading part of the curves is initially about 0.1 for the shallow arches and about 0.12 for the high arches.

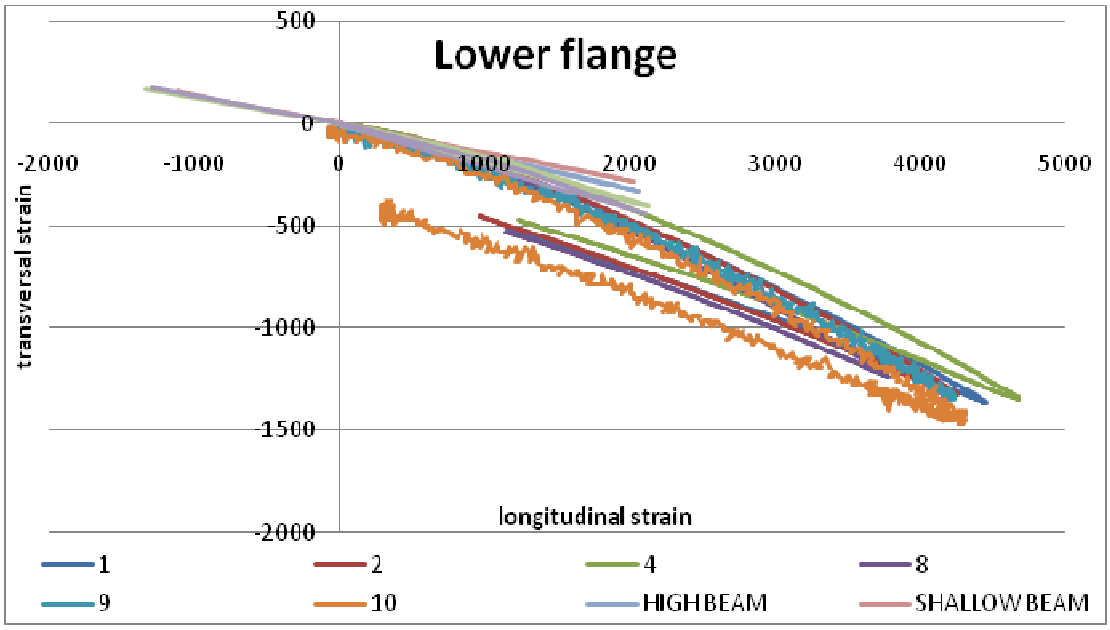

Diagram 7.18 Longitudinal strains- transverse strains for lower flange

7.3.3. Figures from deformed arches

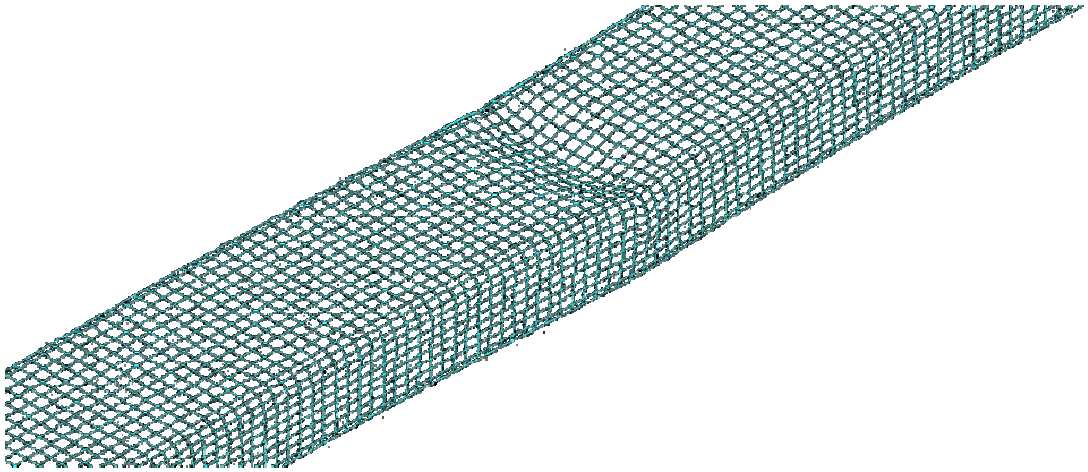

Figure 7.5 The deformed arch after a compression test

Figure 7.5 shows the section of the arch after the end of a compression test. This picture refers to the loaded point, where a local buckling has already been occurred after the plastic hinge. Same situation is regarded at the real experiment in the same time, as figure 7.6 presents.

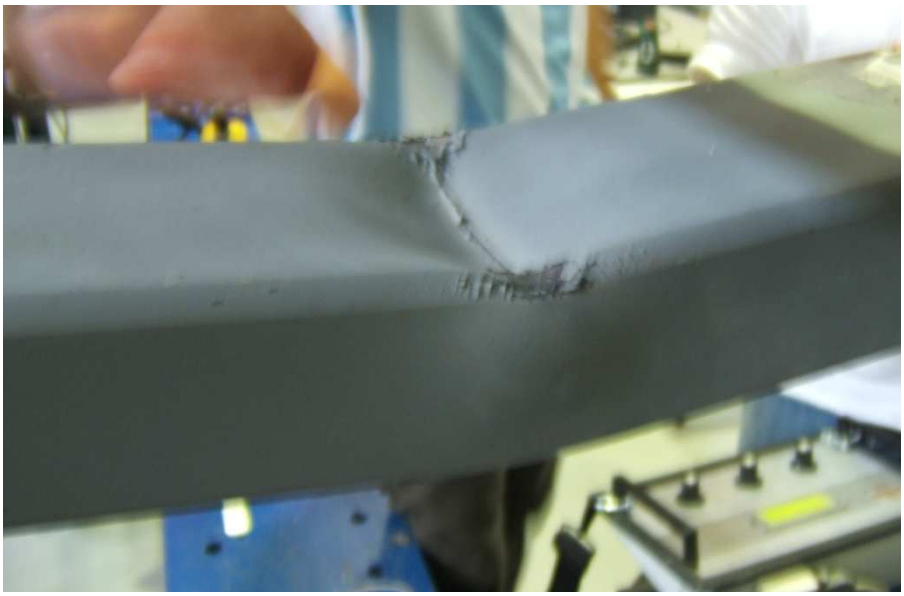

Figure 7.6 Deformed section after the compression test

8. Conclusions

8.1. Influence of out- of- plane stresses- strains

A main part of the present thesis investigates the existence and the significance of the out of plane stresses and strains, which are created due to the curvature of the curved beams, as it has been described in chapter 2. The diagrams of chapter 7 ensure what was proved in chapter 2. The relationship between the main longitudinal strains and those of the out of plane secondary strains is proved in each diagram. Although there are already analytical expressions of the accurate relationship of the two strains, there are also approximated relationships, which are not so close to the real ones. The equation 2.56 indicates the direct relationship of the strains and also the factors which affect the magnitude of the out of plane strains. What affect this magnitude are the geometry of the section and the radius of the curved beam in each situation. In our experiment the geometry of the arch and the section, were chosen in order to maximize the magnitude of these strains.

As it is referred in previous chapters the ratio of the in plane and the out of plane strains is 0.48 for the upper flange and 0.12 for the lower flange. This number indicates what percentage of the main strains, are the out of plane strains. The previous number shows an extreme value which gives the out of plane strains equal to the half of the main longitudinal strains. In fact, the magnitude of the strains is not so significant. The stress values are the most significant and their magnitude is given by relationship 2.52. Because stresses are a mathematical model, they are impossible to be measured directly in an experiment. Thus, the strains are the appropriate magnitudes to conclude safely what happens with the stresses. In our case, the averaged percentage of the out of plane stresses from the in plane reaches the 20%. It is not a typical value of any structure, but it is possible for structures to have such high values of the out of plane stresses.

These stresses can influence the final strength of the section, due to the interaction of the stresses in different directions. Hence, the yield may appear in lower loads than the estimated. Another phenomenon which can be created by these out of plane stresses and strains is the deformation of the flanges, which incline to the internal of the section. This fact is capable to cause the appropriate imperfection and to make easier a local buckling. Finally, the previous deformation of flanges may reduce the moment of inertia of the section, to increase the total external deformation of the structure and to reduce also the ultimate strength.

8.2. Residual stresses

The next part of the present thesis refers to the influence of the residual stresses to the behavior and the strength of arches. These residual stresses are created during the curving process, when a straight beam passes through bending rollers to take the appropriate curvature. These stresses are measured by previous experiments and have been estimated numerically and analytically in chapters 2 and 4, respectively. The magnitude of these stresses is extremely high to be ignored. It is a direct function of the given curvature, but in an averaged case the stresses are close to the yielding stress. The distribution is not constant in the height of the section, but there are regions of the section, where significant residual stresses appear. The experiments and their results in chapter 7 are not the safe path to extract a valid conclusion. Thus, only analytical and numerical methods are used to conclude.

The shell elements are an extremely useful medium to estimate these residual stresses. Two different models constructed to be compared. The first one is an arch, same to the experimental arches, which is loaded by tension and compression load, as described in chapter 4. The second one, is a straight beam that is curved via prescribed rotations at the ends and after this curving process, it is loaded until the ultimate strength. The second model includes the theoretical residual stresses before the loading process begins. The next diagrams show the results of all analyses, which include analyses about a high and a shallow arch under a tension and a compression load. In comparison to the previous, beam model results are presented together.

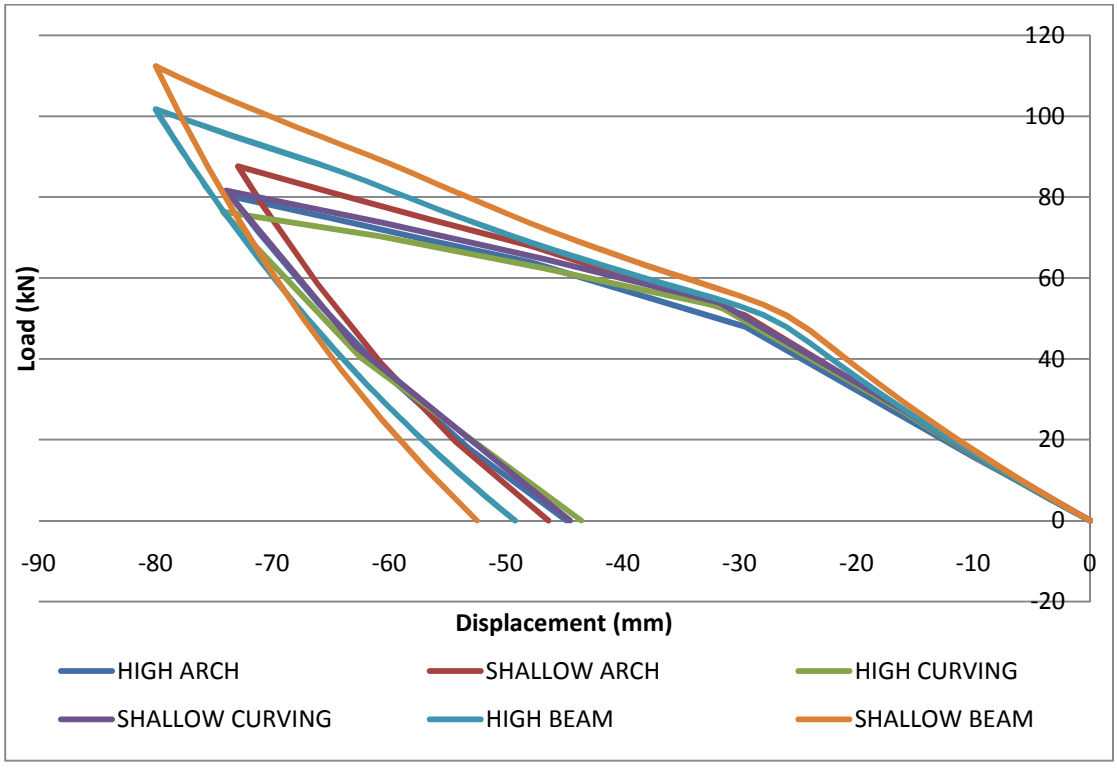

Diagram 8.1 Equilibrium paths for the tension test

Diagram 8.1 shows all the curves in a same path. Beam models are a little far from the more accurate shell models, because they cannot include the local buckling of the plastic hinge in extreme deformations. However, regarding the results of each model (with and without the curving process) for each arch (high and shallow) a noticeable difference at the ultimate strength exists. For each one of the two different arches, a difference of 5% in the final critical load is considered. This difference is for the arches without the curving process that means that they overestimate the real strength of the structure.

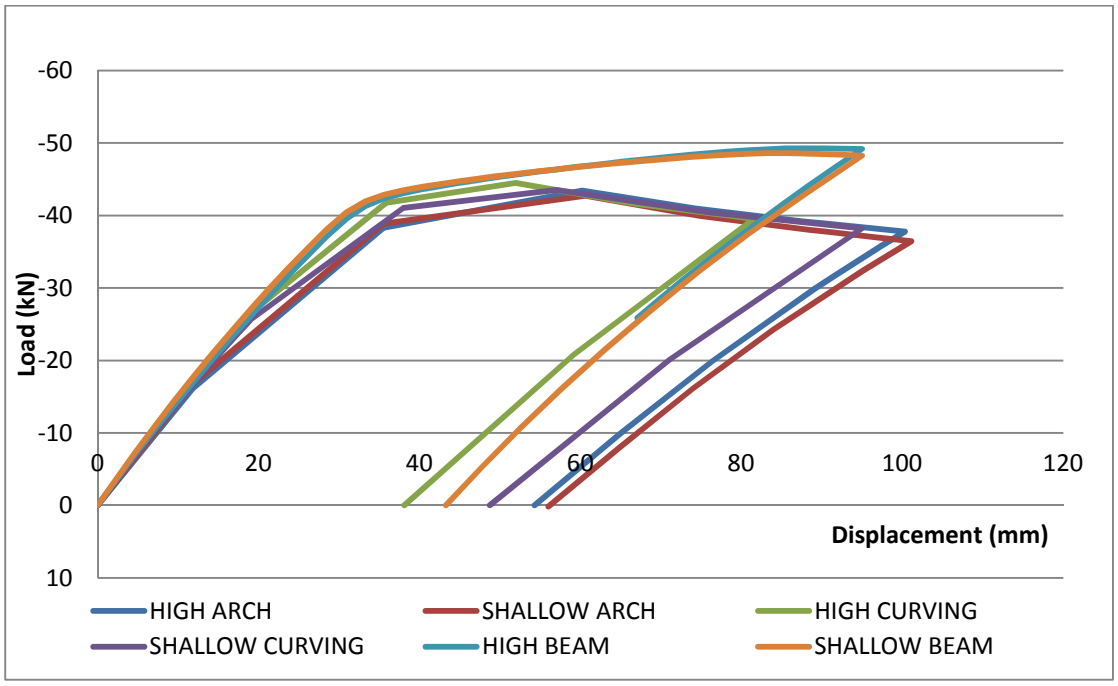

Diagram 8.2 Equilibrium paths for the compression test

In the case of diagram 8.2 the results are similar to the previous. The beam models overestimate the behavior and the strength of the arch, due to the approximated material law and the incapability of the local buckling to appear in this model, much after the plastic hinge occurs. However, the curved arches seem to be more stiffened and strengthen than the perfect ones. This difference is small enough and one can ignore this, because it ranges around the 2 %.

The two following diagrams, diagram 8.3 and 8.4 present the distribution of the longitudinal main stress in the height of the flange, at the final loading step; a moment before the unloading. The first diagram refers to the compression test, while the next one to the tension tests. In these two different cases the distribution is not the same, between the curved arches and the initially perfect arches. Due to the initial residual stresses, which exist at the curved member, the final distribution is different enough. In the region close to the center of the mass the values are extremely different; in this region the residual stresses are in a maximum, as diagram 4.7 shows. Nevertheless, the values of stresses at the extreme fiber are very close to each other.

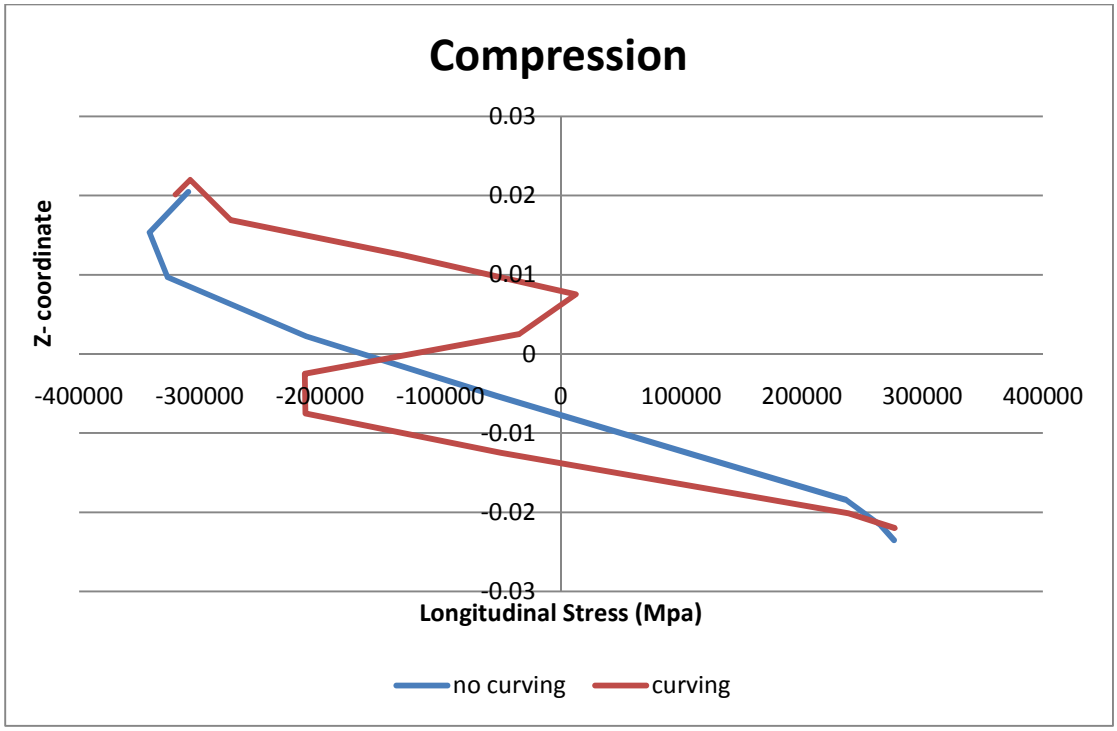

Diagram 8.3 Stress distribution in the height of section for the compression test

Diagram 8.4 presents the same results and conclusions for the tension test, at the time when the loading process ends. The distribution, which does and does not take into account the residual stresses, differs. The major difference is not the deviation of the ultimate stresses, but the opposite sign of stresses into the section near to the center of mass, where the residual stresses are in a maximum.

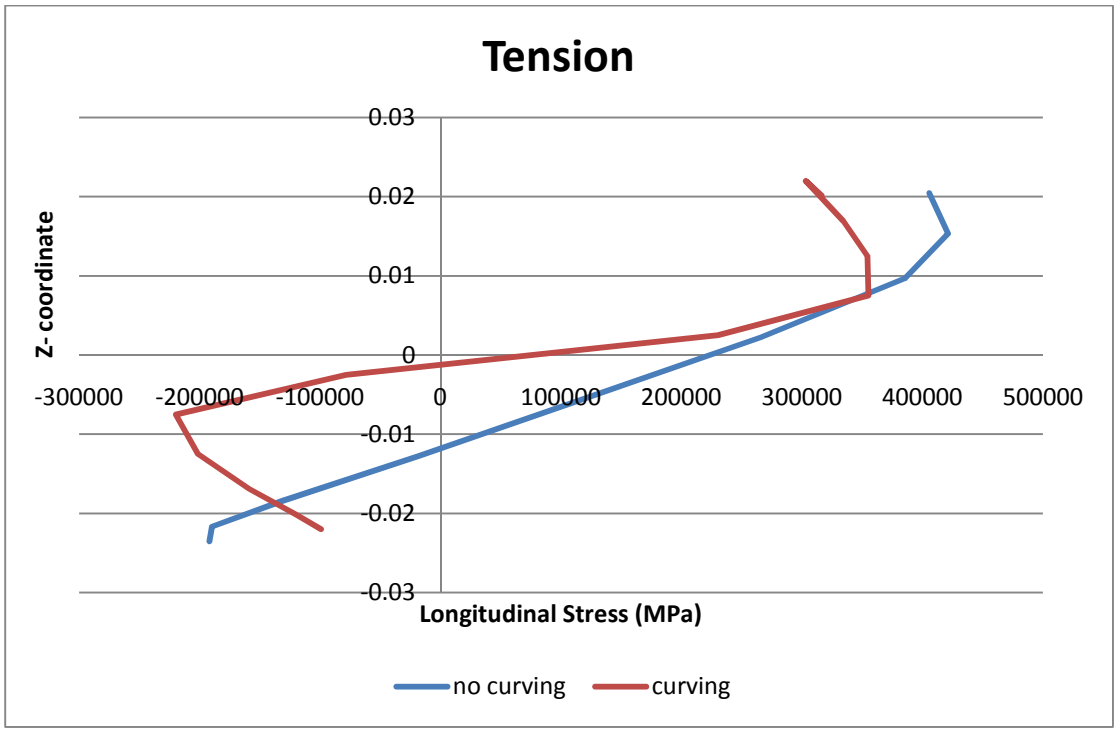

Diagram 8.4 Stress distribution in the height of section for the tension test

8.3. Suggestions

The appropriate suggestions of this thesis refer mainly the ideas for a perfect and valid experiment. The tension test helps one to exceed what exactly is necessary for a conclusion, but the compression test makes the whole issue complicated. The numerical and theoretical models are far from the experimental results, although qualitatively the diagrams seem similar, quantitatively were imperfect. Thus, a theoretical investigation of the difference between the two experiments, are necessary, in order to decide about the significance of the residual stresses and the out of plane stresses.

The high values of the out of plane strains, which are possible to appear in special structures make necessary the estimation of an interacted equivalent stress during the calculation of the ultimate strength. In other words, it is considered reasonable to take into account the interaction of the different stresses and not to be ignored.

Finally, regarding the residual stresses, it is possible to influence the ultimate strength of a structure, either in the final section strength, or in the stability of each member. A safe conclusion is impossible to be made, but it is considered interesting and important to be investigated.

9. REFERENCES

1. Cook, R. D., and W. C. Young: ‘‘*Advanced Mechanics of Materials*,’’ 2nd ed., Prentice-Hall, 1998.
2. Douthe, C., Unpublished report of the MCIEF 235196 DeReStAr Program, 2010
3. Eurocode 3, *Design of steel structures, Part 1: General rules and rules for buildings*, ENV 1993-1-1. CEN, Brussels, Belgium, 1992.
4. EUROPEAN CONVENTION FOR CONSTRUCTIONAL STEELWORK (ECCS), Manual on stability of steel structures- Committee 8, Stability 1976.
5. Galambos, T. V. (ed.), *Guide to stability Criteria for Metal Structures, Structural Stability Research Council (SSRC), 5th edition* , John Wiley and sons, New York, NY, USA 1998.
6. King,C.M., Brown D.G., Design of curved steel, Steel Construction Institute, The, 2001.
7. Li, S.H., Zeng G., Ma Y.F., Guo J.Y., Lai X.M., *Residual stresses in roll-formed square hollow sections*, Thin-Walled Structures 47 (2009) 505–513.
8. Papakonstantinou, T., Gantes C.J., Elastoplastic moment curvature – axial force relations of rectangular solid and hollow and I-sections, unpublished report.
9. Paulsen, F., Welo, T., *Cross-Sectional Deformations of Rectangular Hollow Sections in Bending Part I - Experiments* -, International Journal of Mechanical Sciences 43 (2001) 109-129.
10. Paulsen, F., Welo, T., Sovic, O.P., *A design method for rectangular hollow sections in bending*, Journals of Materials Processing Technology 113 (2001), 699-704.
11. Paulsen, F., Welo, T.,, *Cross-sectional deformations of rectangular hollow sections in bending Part II - analytical models* - International Journal of Mechanical Sciences 43 (2001) 109-129.
12. Peter W. Key & Gregory J. Hancock *A Theoretical Investigation of the Column Behaviour of Cold-Formed Square Hollow Sections*.
13. Pi, Yong- Lin, Trahair, N.S., *Out of Plane Inelastic Buckling and Strength of Steel Archesjournal of Streuctural Engineering*, February 1998, 174-183.
14. *Roark's Formulas for Stress and Strain*, 6th edition, McGraw-Hill, New York, 1989.
15. Sophianopoulos, D.S, Asteris, P.G., Athanasiadou, D. , *The Effect of Thermal-Induced Residual Stresses on the Elastoplastic Behavior and Capacity of Non-Slender Steel I-Shaped Members under Combined Loading*, Techn. Chron. Sci. J. TCG, I, No 1-2, 2006.
16. Timoshenko, S. P. and Goodier, J. N., *Theory of Elasticity*, 3rd edition, McGraw-Hill, New York, 1970.
    a. από χάλυβα.
17. Αρμενάκας, Α.Ε., Στατικη ραβδωτών φορέων- Υπερστατικοί φορείς, 1992.
18. Βάγιας Ι., Ερμόπουλος Ι., Ιωαννίδης Γ.,(2005) Σχεδιασμός δομικών έργων
19. Χατζηιωάννου, Μ., αναλυτικές μέθοδοι υπολογισμού διαγραμμάτων αλληλεπίδρασης διατομών διπλού ταυ, διπλωματική εργασία ΕΜΠ, 2010

Appendix A

This first appendix presents the drawings and the details of all the members which were used in the experiments. Among others, there are drawings of the laboratory frame, the arches, the supports, the loading plate and the lateral restrains. All the drawings was sent and modified for the construction by EMEK Company.

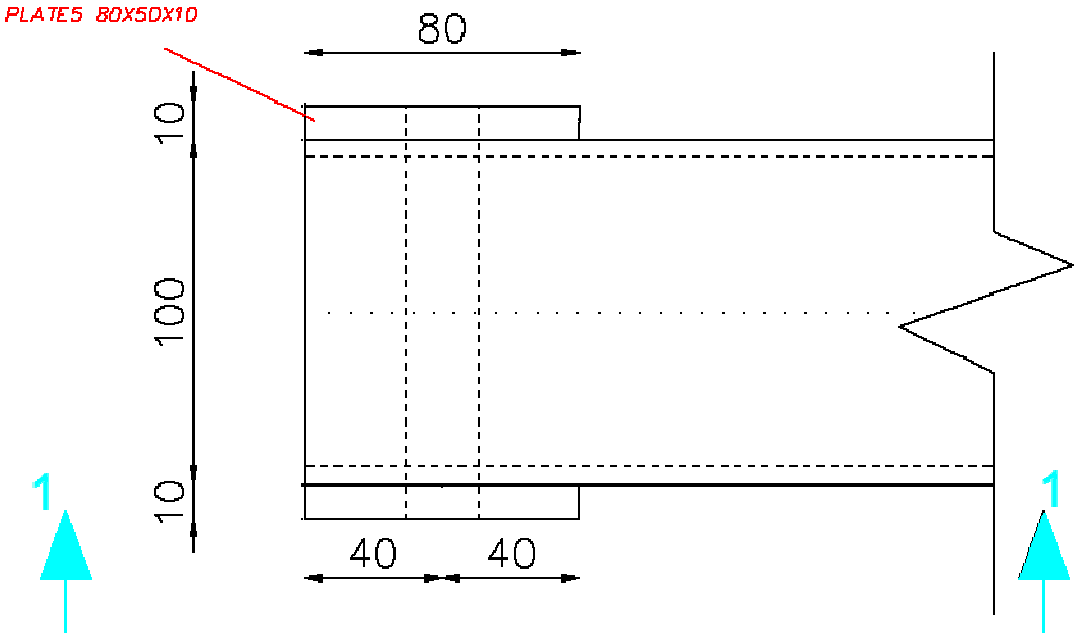

Figure A.1 Detail of the end of each arch

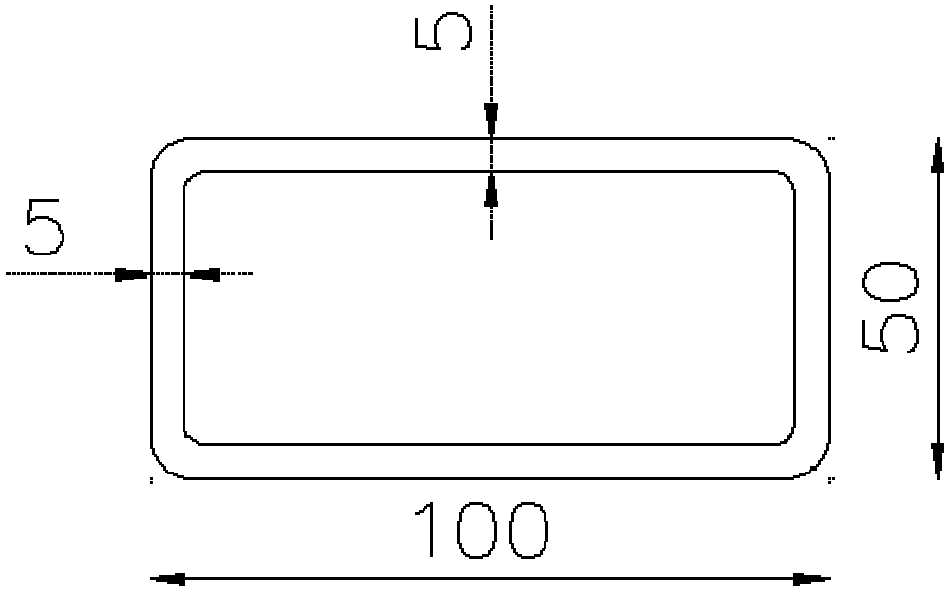

Figure A.2 The section of the arches

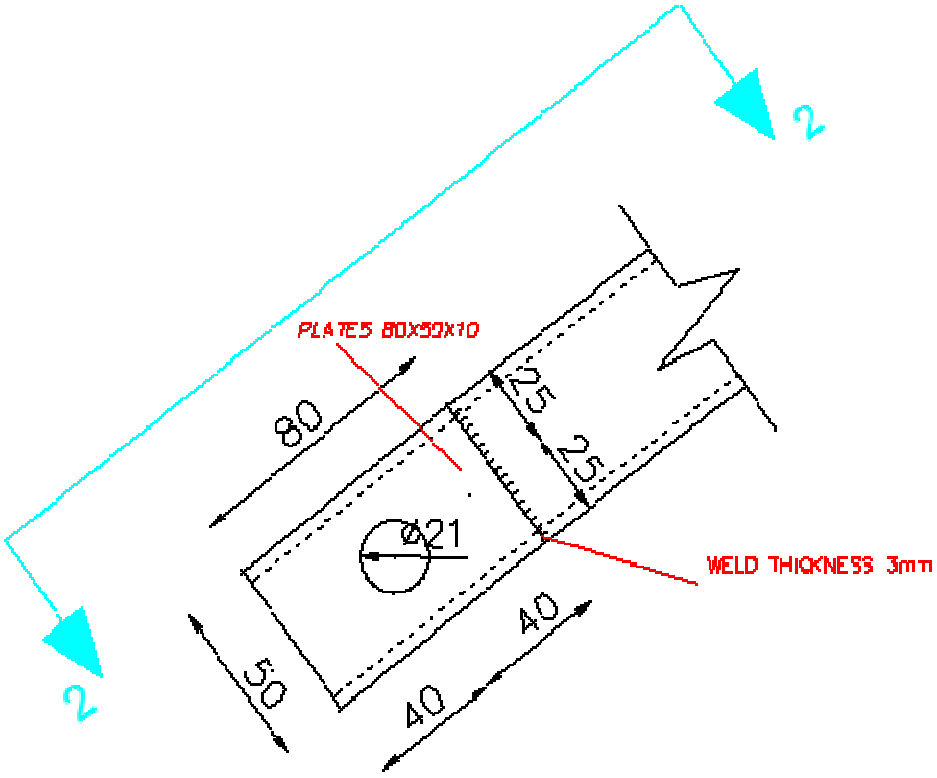

Figure A.3 Lateral detail of the end of each arch

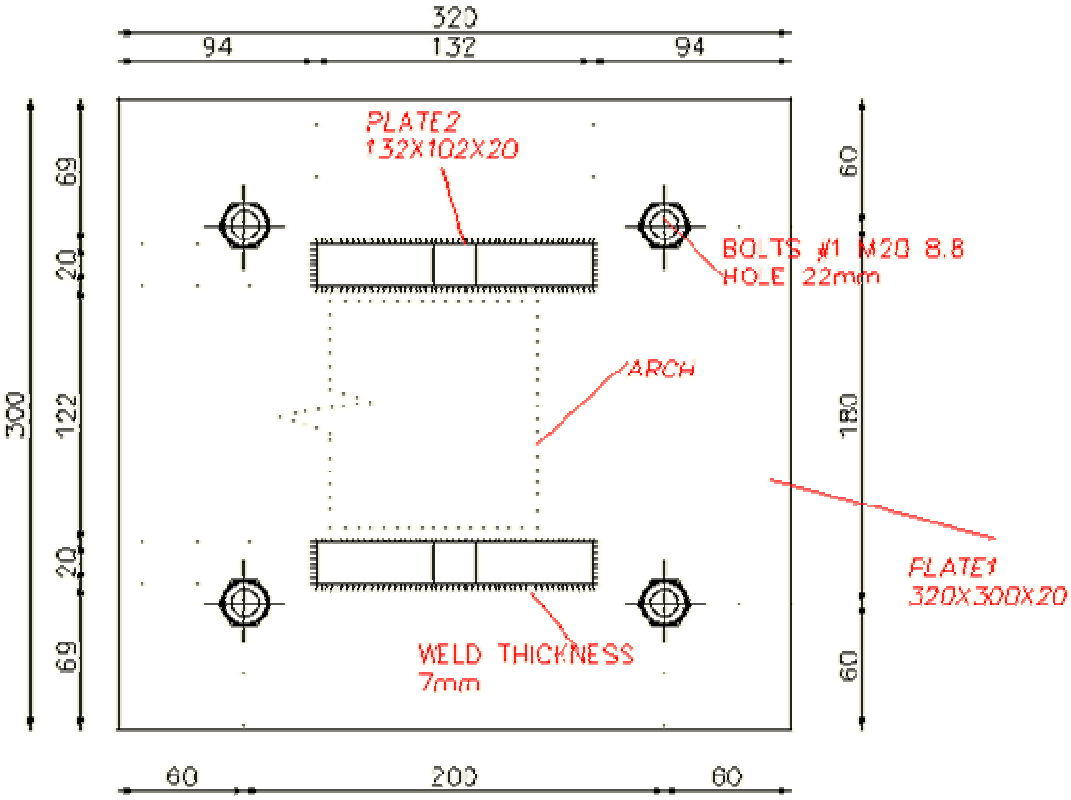

Figure A.4 Ground plan of the main support

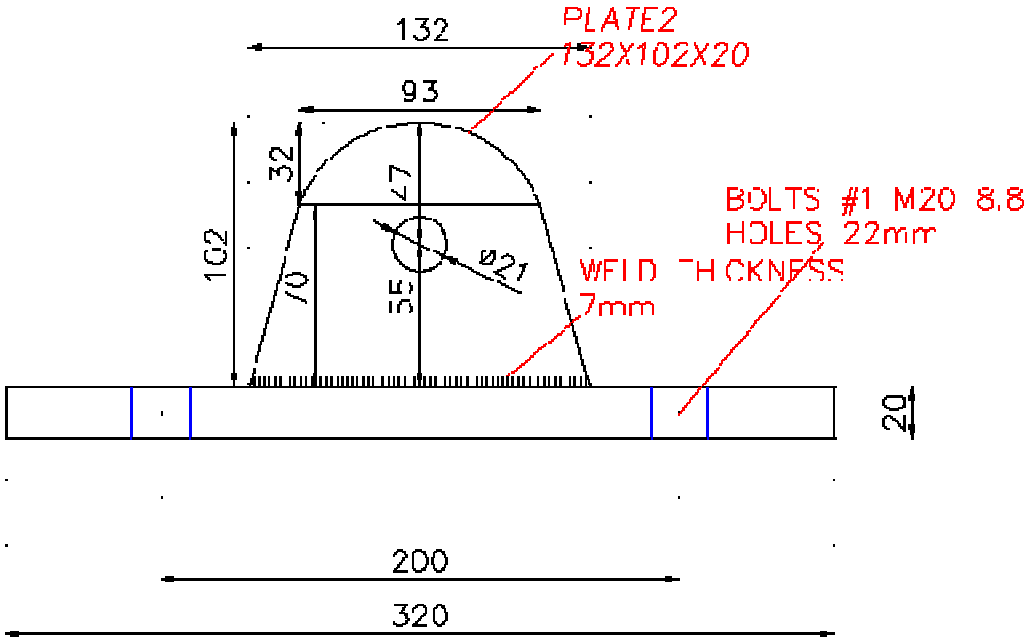

Figure A.5 Lateral view of the main support

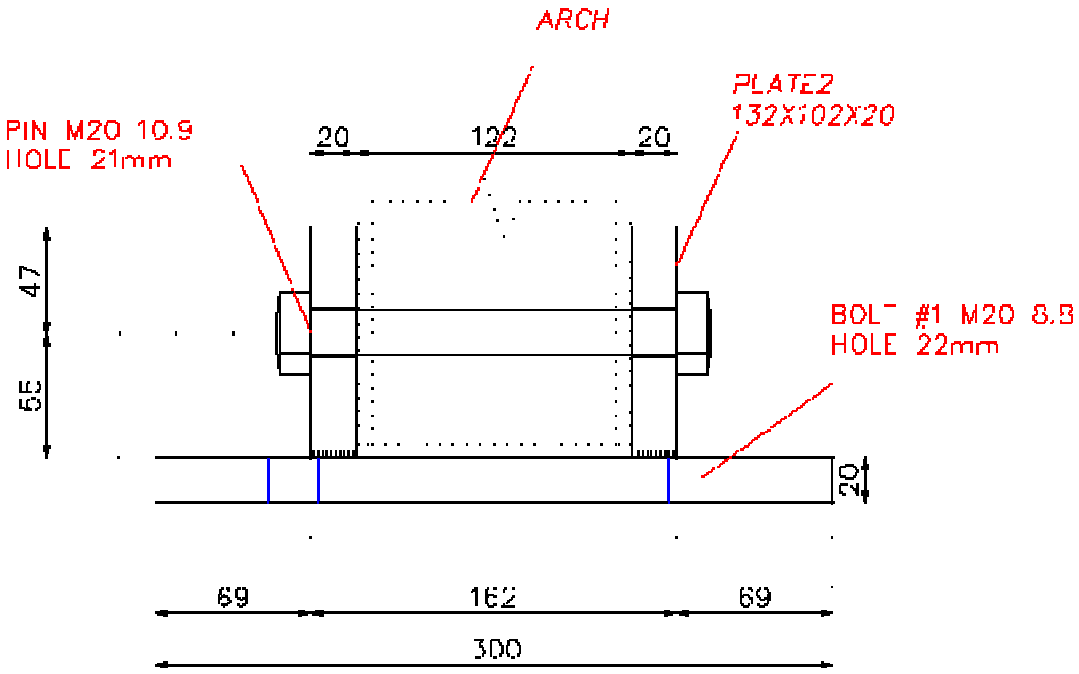

Figure A.6 Front view of the main support

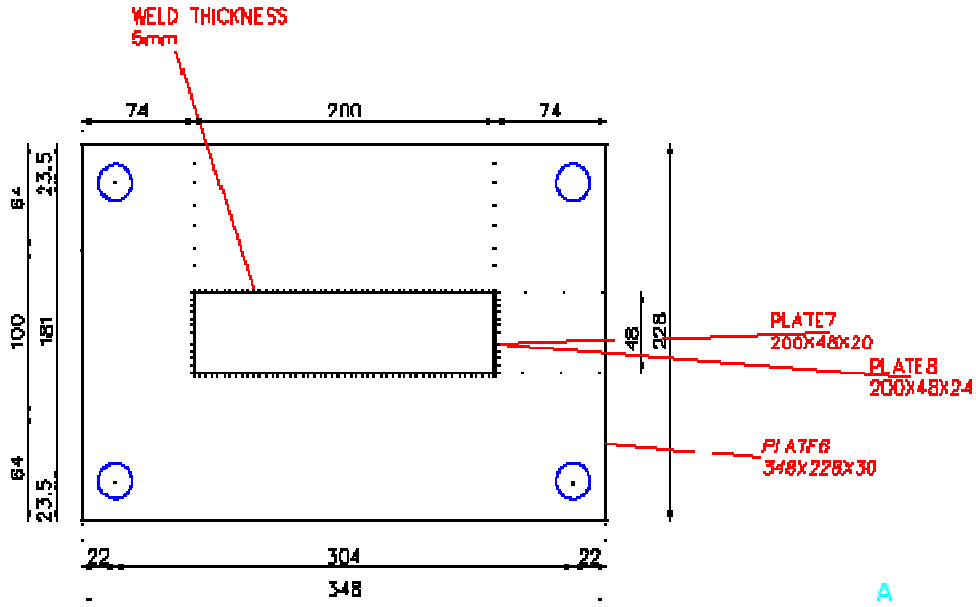

Figure A.7 Plan of the load- plate

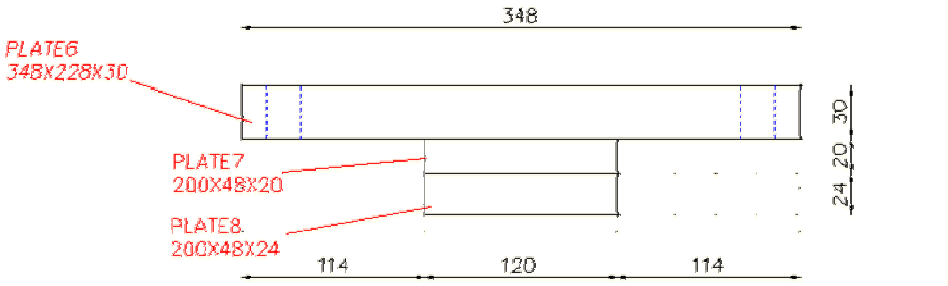

Figure A.8 Front view of the load- plate

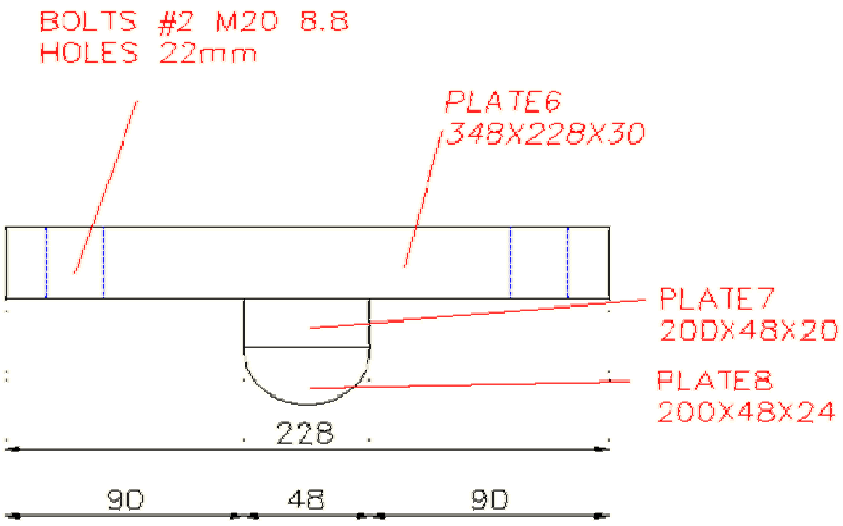

Figure A.9 Lateral view of the load plate

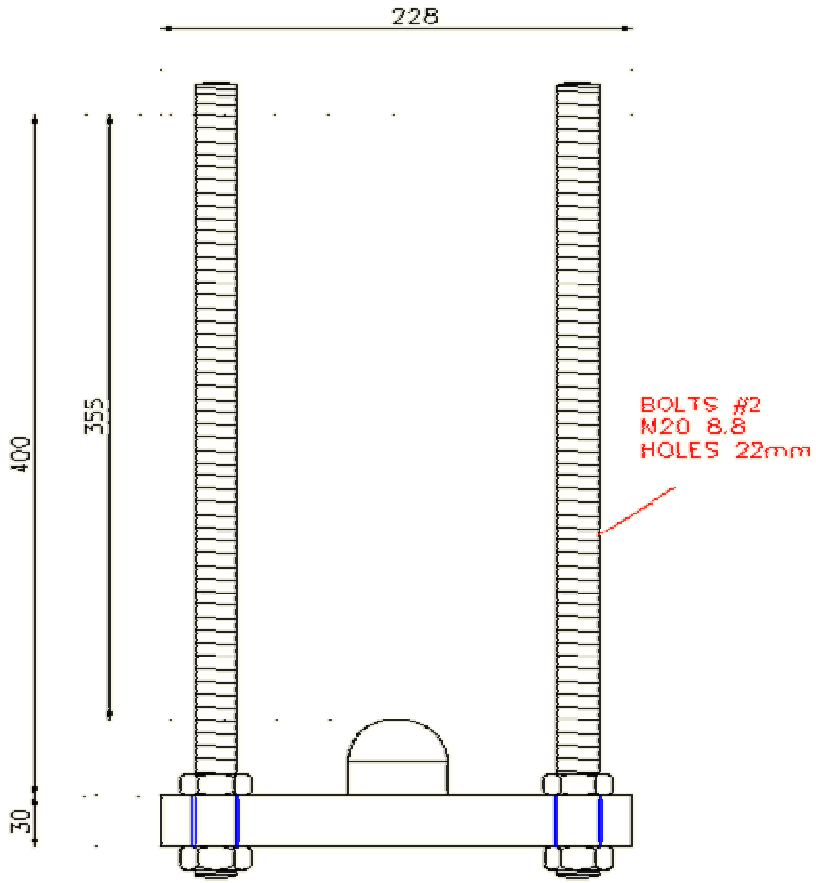

Figure A.10 Lateral view of the load plate for the tension test

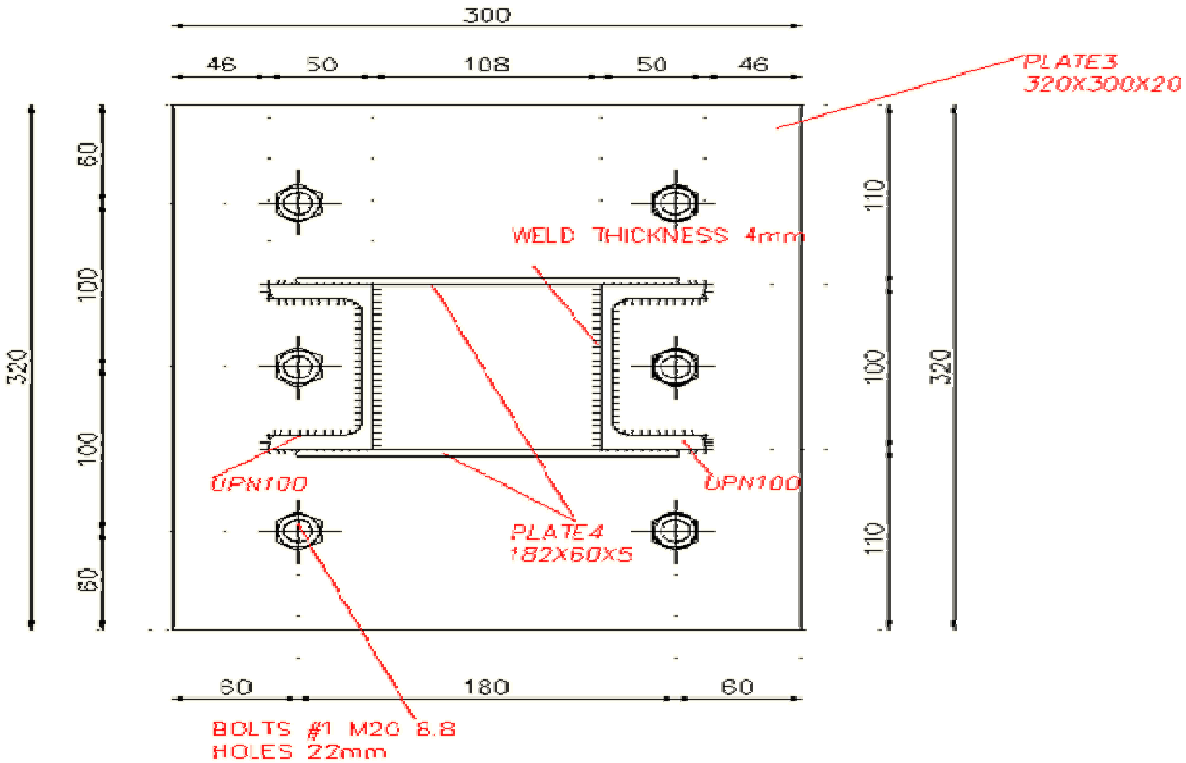

Figure A.11 Plan of the lateral support

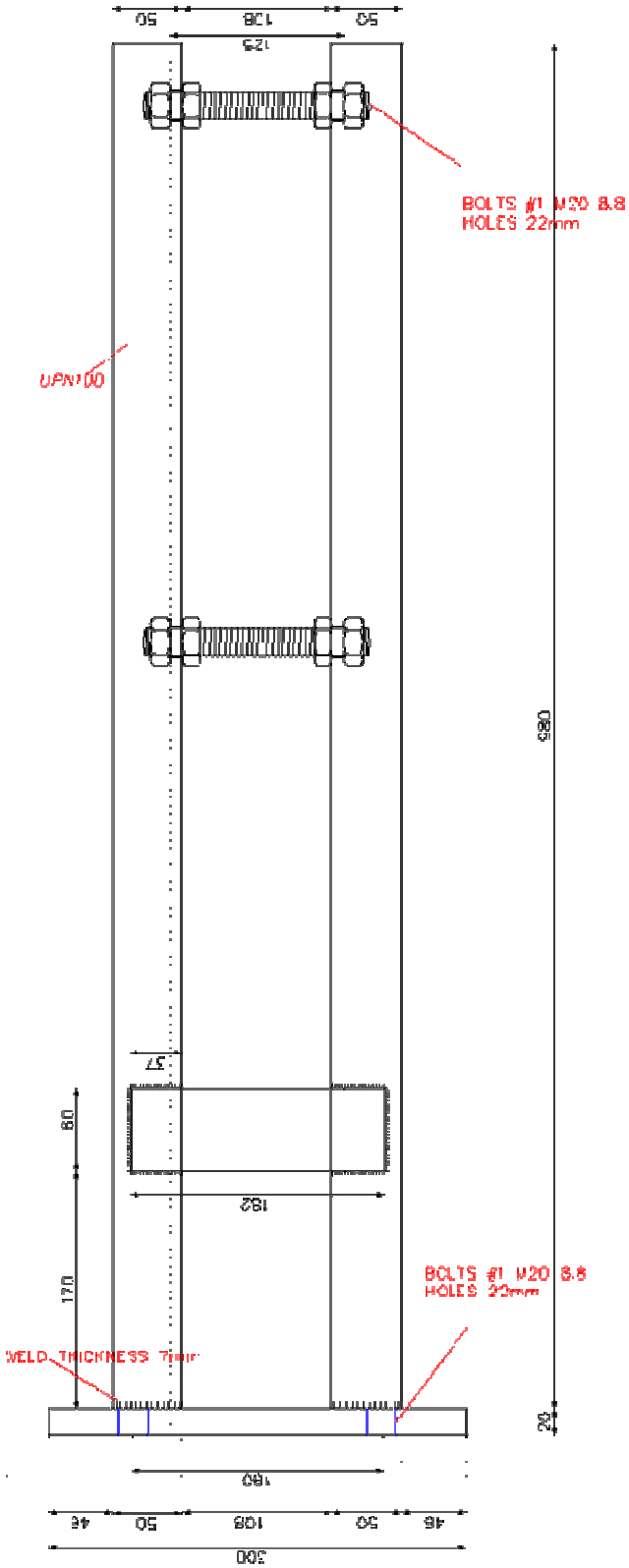

Figure A.12 View of the lateral support

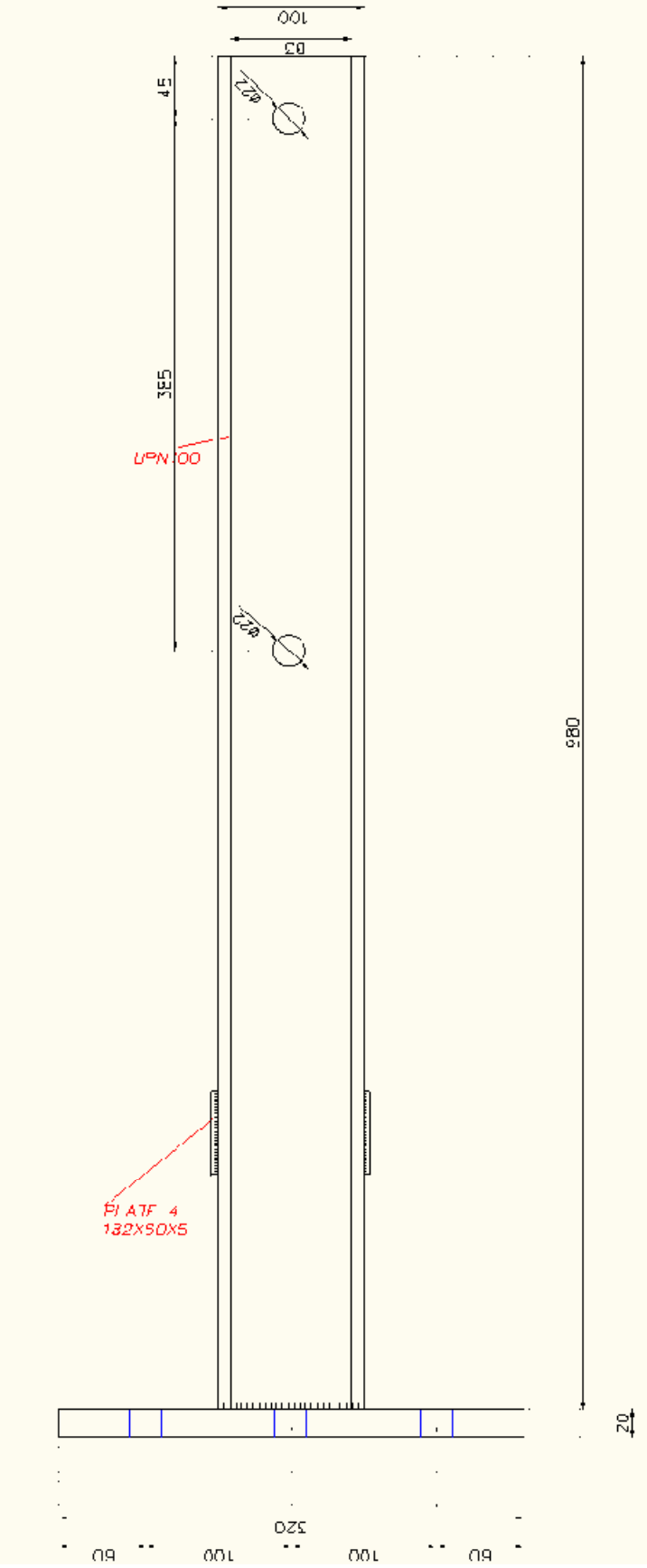

Figure A.13 View of the lateral support

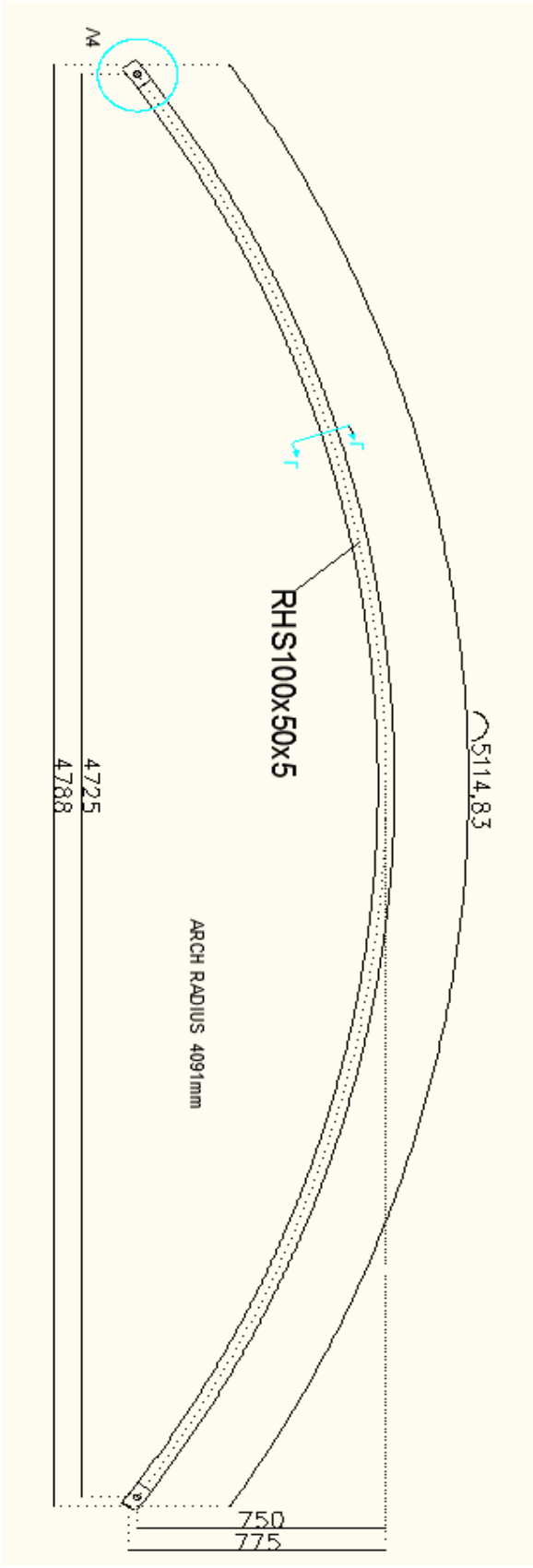

Figure A.14 Shallow arch

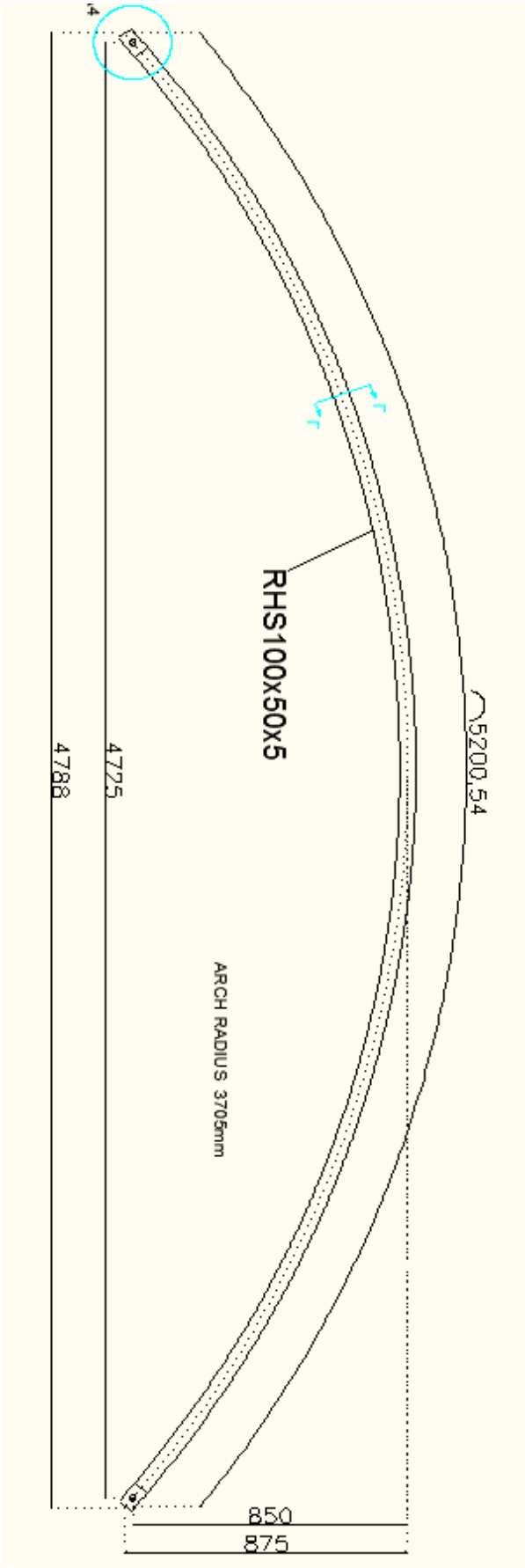

Figure A.15 High arch

Appendix B

The present appendix shows some characteristic pictures from the laboratory, where the experiments took place. In these pictures all the set-up of the experiment is shown and each member as well.

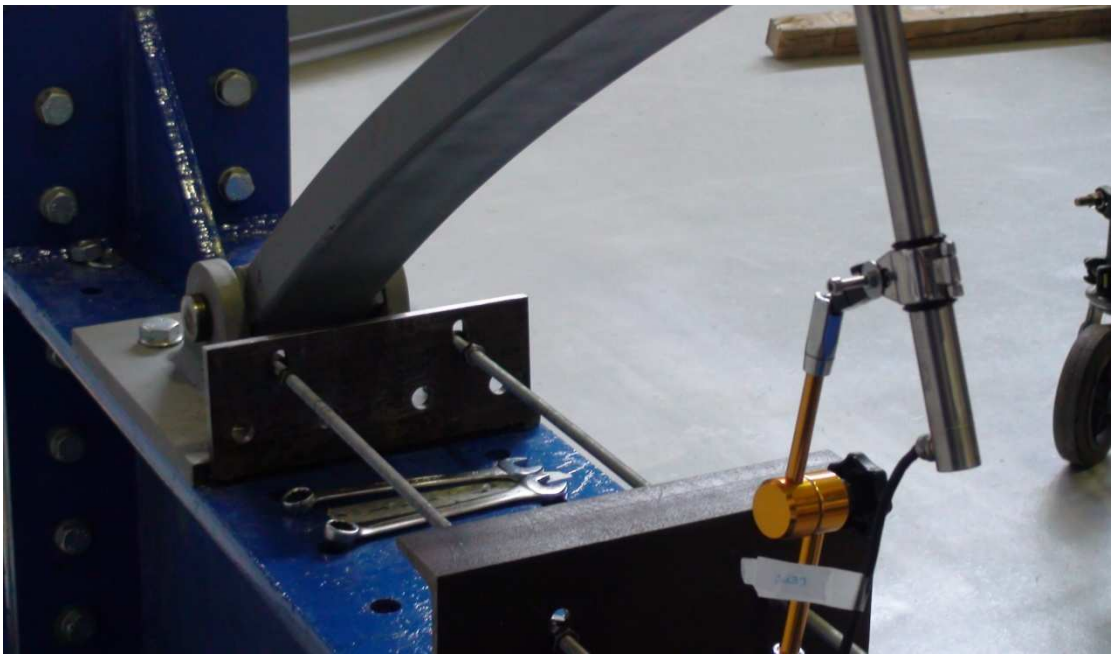

Figure B.1 The helpful set-up to release the arch safely, erasing partially the internal residual forces.

Figure B.2 The lateral support, embracing the arch

Figure B.3 The lateral support

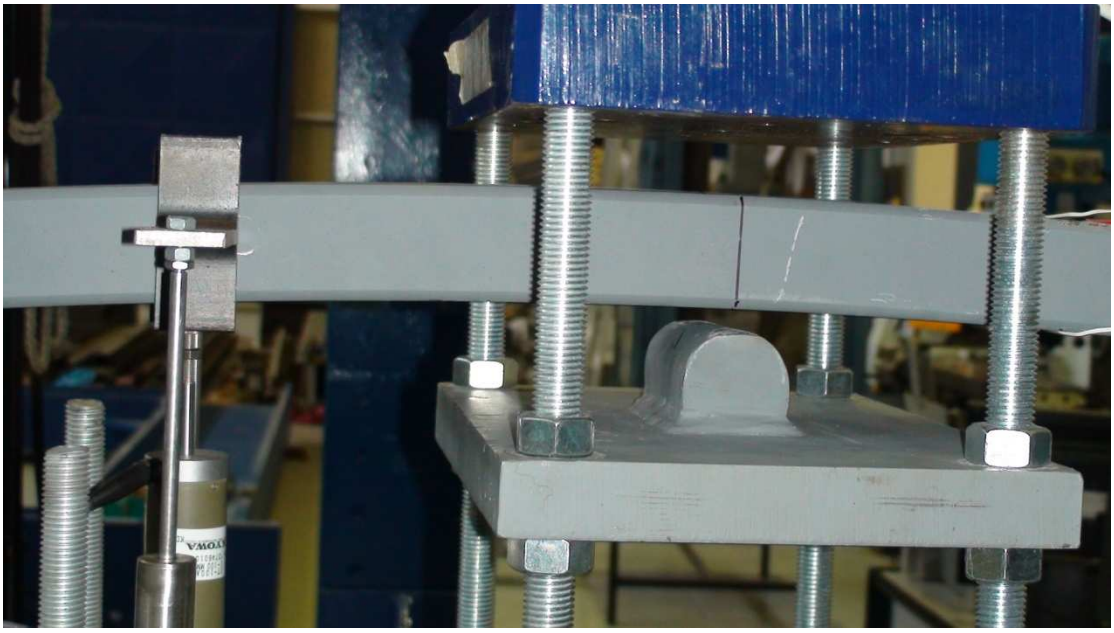

Figure B.4 The load plate in a tension arrangement

Figure B.5 The load cell in a compression arrangement

Figure B.6 the deformed arch, after a compression test

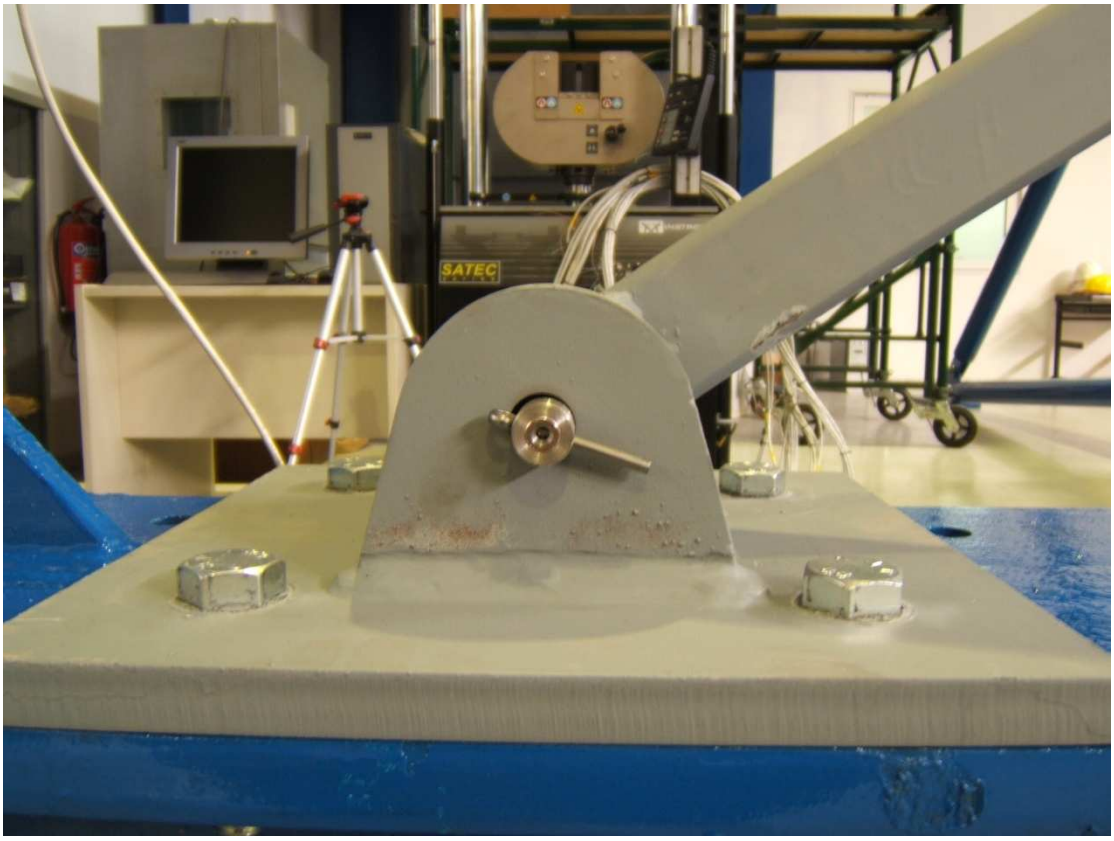

Figure B.7 the support and the gap between hole and pin, responsible for the sliding process